

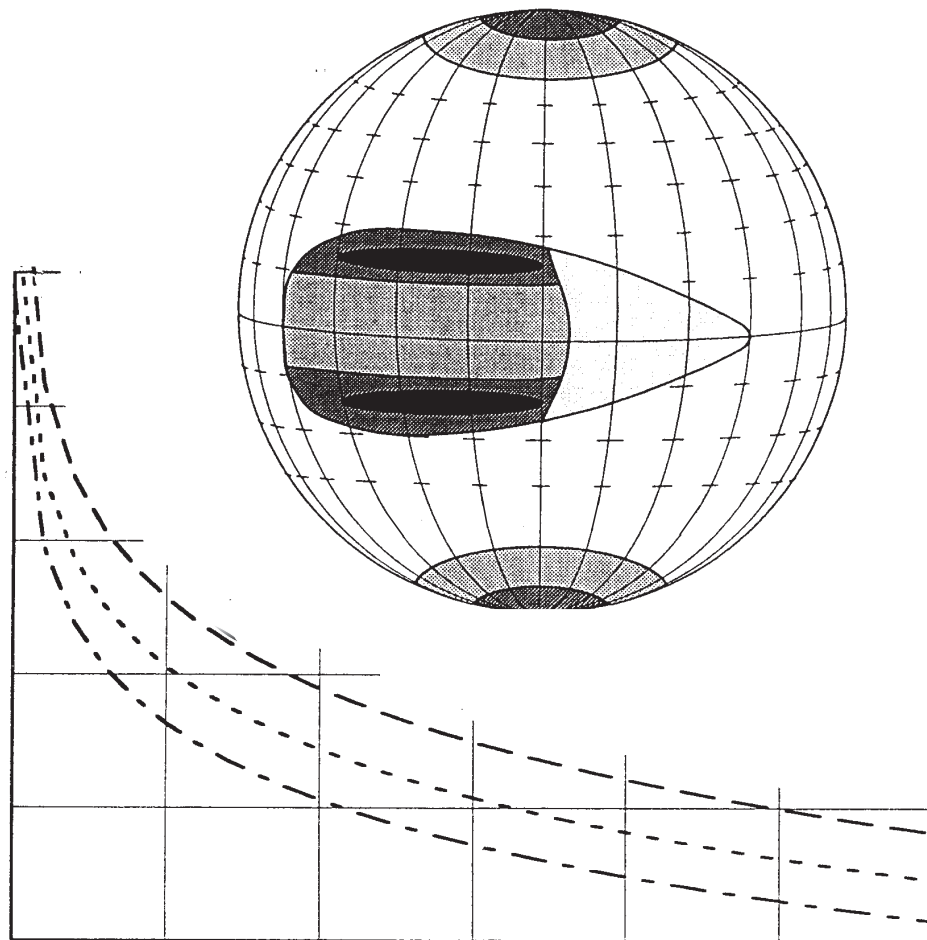


INTERNATIONAL TELECOMMUNICATION UNION

# HANDBOOK

## RADIOWAVE PROPAGATION INFORMATION FOR PREDICTIONS FOR EARTH-TO-SPACE PATH COMMUNICATIONS

HANDBOOK ON EARTH-SPACE PROPAGATION



Radiocommunication Bureau  
Geneva, 1996



# **HANDBOOK**

## **RADIOWAVE PROPAGATION INFORMATION FOR PREDICTIONS FOR EARTH-TO-SPACE PATH COMMUNICATIONS**



## **PREFACE**

This Handbook has been developed by experts of Working Party 3M (Point-to-point and Earth-space propagation) of ITU-R Study Group 3 (Radiowave propagation), under the chairmanship of Mr. M.P.M. Hall (U.K.).

Major contributors to the Handbook were:

Dr. Jeremy Allnut  
Dr. J.P.V. Poiaras Baptista  
Dr. Asoka Dissanayake  
Mr. Glenn Feldhake  
Ms. Fatim Haidara  
Dr. Yoshio Karasawa  
Prof. Marlene Pontes  
Dr. David Rogers  
Mr. Erkki Salonen  
Dr. Haim Soicher  
Mrs. Carol Wilson

The Handbook was edited by Mrs Carol Wilson and Dr. David Rogers.

## TABLE OF CONTENTS

	<b>Page</b>
<b>CHAPTER 1 - INTRODUCTION</b> .....	1
1.1 Relationship of this Handbook to Recommendations of ITU-R Study Group 3.....	1
1.2 Application of the Earth-space Handbook.....	2
<b>CHAPTER 2 - PROPAGATION EFFECTS OF THE TROPOSPHERE AND THE IONOSPHERE</b> .....	4
<b>CHAPTER 3 - PROPAGATION LOSS</b> .....	5
3.1 Attenuation due to atmospheric gases .....	5
3.1.1 Procedure for calculating gaseous attenuation .....	5
3.2 Attenuation by precipitation and clouds .....	5
3.2.1 Prediction of attenuation statistics for an average year (from point rainfall rate).....	5
3.2.1.1 Basis of prediction method for rain attenuation.....	5
3.2.1.2 Equivalent rain cell length .....	6
3.2.1.3 Effective rain height.....	7
3.2.1.4 Specific attenuation.....	7
3.2.2 Long-term frequency and polarization scaling of rain attenuation statistics..	8
3.2.3 Seasonal variations - worst month.....	8
3.2.4 Discussion of model evaluation (testing) .....	8
3.2.5 Example calculation .....	9
3.2.6 Cloud attenuation .....	10
3.3 Diversity and spatial features of rain.....	11
3.3.1 Site diversity.....	11
3.3.1.1 Reference distribution .....	13
3.3.1.2 Diversity improvement factor .....	14
3.3.1.3 Diversity gain .....	15
3.3.1.4 Instantaneous diversity gain.....	15
3.3.1.5 Comparison of diversity improvement factor and diversity gain as measurement parameters.....	15
3.3.1.6 Example calculations using the recommended site diversity prediction procedures .....	16
3.3.1.7 Factors affecting site diversity performance .....	19
3.3.2 Statistical distribution of signal level for large areas .....	24
3.3.3 Other diversity schemes .....	25
3.3.3.1 Orbital diversity .....	26
3.3.3.2 Frequency diversity .....	26
3.3.3.3 Time diversity .....	26

3.4	Characteristics of precipitation events.....	27
3.4.1	Duration of individual fades.....	28
3.4.2	Interfade and inter-event intervals.....	31
3.4.3	Rates of change of attenuation .....	33
3.4.4	Correlation of instantaneous values of attenuation at different frequencies ..	34
3.5	Sand and dust effects .....	34
3.5.1	General .....	34
3.5.2	Categories of dust storms .....	35
3.5.3	Propagation impairment prediction models for dust effects .....	37
3.5.4	Typical propagation impairment prediction results .....	38
	References for Chapter 3 .....	40
	<b>CHAPTER 4 - SKY NOISE TEMPERATURE CONTRIBUTIONS.....</b>	<b>46</b>
4.1	Atmospheric noise temperature effects on Earth-space paths .....	46
4.2	Galactic and other extraterrestrial noise sources .....	46
4.3	Noise from the surface of the Earth and man-made sources .....	47
4.4	Example problem.....	47
	References for Chapter 4 .....	48
	<b>CHAPTER 5 - PATH DEPOLARIZATION.....</b>	<b>49</b>
5.1	Introduction .....	49
5.1.1	Physical causes of depolarization.....	49
5.1.2	Systems importance of depolarization .....	49
5.1.3	Cross-polarization isolation and discrimination.....	50
5.1.4	Polarization states.....	50
5.1.5	Polarization orthogonality and mismatch.....	51
5.2	Relation between depolarization and attenuation.....	53
5.2.1	Computation of long-term XPD statistics .....	53
5.2.1.1	Ice depolarization .....	53
5.2.1.2	Frequency dependence .....	54
5.2.1.3	Dependence on time percentage.....	55
5.2.2	Dependence on path configuration.....	56
5.2.3	Evaluations of model performance.....	57
5.2.4	Joint statistics of XPD and attenuation .....	57
5.2.5	Long-term frequency and polarization scaling.....	58
5.3	Dependence of XPD and XPI on physical processes .....	58
5.3.1	Faraday rotation in the ionosphere .....	58
5.3.2	Precipitation effects .....	58
5.3.2.1	Differential attenuation .....	58
5.3.2.2	Differential phase .....	59

5.4	Data relevant to cross-polarization compensation.....	59
5.5	Incorporation of path XPD into system XPI.....	60
5.6	Example calculation of path XPD .....	61
5.6.1	Step-by-step application of the method.....	61
5.6.2	Example of a system application.....	63
	References for Chapter 5 .....	66
	<b>CHAPTER 6 - CLEAR AIR EFFECTS .....</b>	<b>69</b>
6.1	Loss due to defocusing and wave-front incoherence.....	69
6.2	Scintillation and multipath effects .....	69
6.2.1	General .....	69
6.2.2	Background of the scintillation model .....	70
6.2.2.1	Seasonal and diurnal variations.....	70
6.2.2.2	Frequency dependence .....	72
6.2.2.3	Elevation angle dependence.....	72
6.2.2.4	Antenna aperture diameter dependence .....	72
6.2.2.5	Probability density function (PDF) of signal-level variations .....	72
6.2.2.6	Polarization dependence.....	73
6.2.3	Accuracy and applicable range of the prediction method.....	73
6.2.3.1	Accuracy and applicability of r.m.s. fluctuation prediction.....	73
6.2.3.2	Accuracy and applicability of PDF prediction.....	74
6.2.4	Signal variations at elevation angles lower than about 5°.....	74
6.2.4.1	Empirical model .....	75
6.2.4.2	Characteristics of low-angle fading .....	78
6.3	Propagation delays.....	78
6.4	Angle of arrival.....	80
	References for Chapter 6 .....	81
	<b>CHAPTER 7 - TRANSIONOSPHERIC PROPAGATION.....</b>	<b>82</b>
7.1	Introduction .....	83
7.2	Total Electron Content (TEC) .....	83
7.3	Effects due to background ionization .....	83
7.3.1	Faraday rotation.....	83
7.3.2	Group delay .....	84
7.3.3	Dispersion.....	86
7.3.4	Doppler frequency shift.....	86
7.3.5	Direction of arrival of the ray.....	86
7.3.6	Absorption .....	87
7.3.6.1	Auroral absorption .....	87
7.3.6.2	Polar cap absorption.....	87

7.4	Effects due to ionization irregularities.....	88
7.4.1	Scintillation effects.....	88
7.4.2	Geographic, seasonal and solar dependence .....	89
7.4.3	Scintillation models.....	90
7.5	Conclusion .....	92
	References for Chapter 7 .....	93
<b>CHAPTER 8 - SURFACE REFLECTIONS AND LOCAL ENVIRONMENTAL EFFECTS (OF PARTICULAR INTEREST TO MOBILE-SATELLITE SYSTEMS).....</b>		<b>95</b>
8.1	Introduction .....	95
8.2	Effects of the Earth's surface .....	95
8.2.1	Reflection from the Earth.....	96
8.2.1.1	Specular reflection from a plane Earth.....	96
8.2.1.2	Specular reflection from a smooth spherical Earth.....	97
8.2.1.3	Divergence factor .....	98
8.2.1.4	Reflection from rough surfaces.....	99
8.2.1.5	Reflection multipath.....	101
8.2.2	Fading due to sea reflection.....	102
8.2.2.1	General .....	102
8.2.2.2	Sea surface characteristics.....	102
8.2.2.3	Fading calculation model .....	104
8.2.3	Shadowing and blockage.....	111
8.2.3.1	Tree shadowing .....	111
8.2.3.2	Building shadowing .....	115
8.2.4	Fading in AMSS due to land reflection.....	117
8.2.5	Interference from adjacent satellite systems .....	118
8.2.5.1	General .....	118
8.2.5.2	Basic assumptions of the model .....	118
8.2.5.3	Prediction accuracy .....	120
8.2.6	Example problem .....	120
8.2.7	Results of experimental measurements .....	123
8.2.7.1	LMSS measurements.....	123
8.2.7.2	Measurements of sea-reflection multipath effects .....	126
8.3	Local environmental effects .....	127
8.3.1	Noise contribution of local environment.....	127
8.3.2	Ship superstructure/blockage .....	128
8.3.3	Motion of mobile antenna .....	129

References for Chapter 8 .....	131
<b>CHAPTER 9 - COMBINED EFFECTS MODELLING</b> .....	134
9.1 Equiprobable summation .....	134
9.2 Convolution .....	135
9.3 Temporal segmentation .....	135
9.4 Root-Square summing .....	136
9.5 Example .....	136
References for Chapter 9 .....	137

## CHAPTER 1

### INTRODUCTION

#### 1.1 Relationship of this Handbook to Recommendations of ITU-R Study Group 3

The Handbook on “Radiowave Propagation Information for Predictions for Earth-Space Path Communications” supplies background and supplementary information on radiowave propagation effects. It serves as a companion volume and guide to the Recommendations that are maintained by Study Group 3 (SG 3) of the ITU Radiocommunication Sector (ITU-R) to assist in the design of Earth-space communication systems.

This handbook is intended to be used in conjunction with the published SG 3 Recommendations to assist the user in the application of those Recommendations. It applies to SG 3 Recommendations containing impairment prediction methods and engineering advice on radiowave propagation for the fixed-satellite service (FSS); broadcasting-satellite service (BSS); maritime mobile-satellite service (MMSS); land mobile-satellite service (LMSS); and aeronautical mobile-satellite service (AMSS). Specific versions of the corresponding Recommendations that are used throughout this handbook are:

- ITU-R P.618-4: Propagation data and prediction methods required for the design of Earth-space telecommunications systems, Geneva, 1996.
- ITU-R P.679-1: Propagation data required for the design of broadcasting-satellite systems, Geneva, 1994.
- ITU-R P.680-1: Propagation data required for the design of Earth-space maritime mobile telecommunication systems, Geneva, 1994.
- ITU-R P.681-2: Propagation data required for the design of Earth-space land mobile telecommunication systems, Geneva, 1996.
- ITU-R P.682-1: Propagation data required for the design of Earth-space aeronautical mobile telecommunication systems, Geneva, 1994.
- ITU-R P.531-3: Ionospheric effects influencing radio systems involving spacecraft, Geneva, 1994.

This handbook is keyed to the above Recommendations and uses the same terminology and notation. Reference is made to equation numbers in the Recommendations, for application as a companion volume. Duplication of propagation data from the Recommendations is intentionally minimal, and the prediction methods are found in the Recommendations. It is preferable, of course, to use the latest version of the Recommendations for system calculations.

Proper application of the Recommendations for the Earth-space services requires radiometeorological and other data from additional ITU-R Recommendations. In addition, significant background material can be found in the ITU-R Handbook on Radiometeorology. The versions of the other Recommendations referred to in this handbook are the following:

- ITU-R P.311-7: Acquisition, presentation and analysis of data in studies of tropospheric propagation, Geneva, 1994.
- ITU-R P.372-6: Radio Noise, Geneva, 1994.
- ITU-R P.453-5: The radio refractive index: its formula and refractivity data, Geneva, 1996.
- ITU-R P.526-4: Propagation by diffraction, Geneva, 1996.

- ITU-R P.527-3: Electrical characteristics of the surface of the Earth, Geneva, 1994.
- ITU-R P.530-6: Propagation data and prediction methods required for the design of terrestrial line-of-sight systems, Geneva, 1996.
- ITU-R P.581-2: The concept of “worst month”, Geneva, 1994.
- ITU-R P.676-2: Attenuation by atmospheric gases, Geneva, 1996.
- ITU-R P.834-1: Effects of tropospheric refraction on radiowave propagation, Geneva, 1994.
- ITU-R P.836: Surface water vapour density, Geneva, 1994.
- ITU-R P.837-1: Characteristics of precipitation for propagation modelling, Geneva, 1994.
- ITU-R P.838: Specific attenuation model for rain for use in prediction methods, Geneva, 1994.
- ITU-R P.839: Rain height model for prediction methods, Geneva, 1994.
- ITU-R P.840-1: Attenuation due to clouds and fog, Geneva, 1994.
- ITU-R P.841: Conversion of annual statistics to worst-month statistics, Geneva, 1994.
- ITU-R P.1057: Probability distributions relevant to radiowave propagation modelling, Geneva, 1994.

## **1.2 Application of the Earth-space Handbook**

Accurate propagation information is required to support the design, implementation and operation of most modern satellite communication systems. The propagation behaviour of radiowaves, in the ionosphere and the troposphere, near the Earth's surface, or upon reflection from the surface, is of concern to telecommunication system designers intending to use an atmospheric propagation medium for the transmission of electromagnetic energy between antennas in the system. Signal degradations that occur with sufficient frequency and intensity to affect the performance and availability objectives must be estimated and accounted for in the link budget as part of the system design. Methods are thus required to predict the magnitude and occurrence of relevant propagation impairments with sufficient accuracy for engineering applications.

This handbook provides background on the physical causes for path impairments, the bases for the prediction methods that are found in the Recommendations, and additional information considered useful for engineering applications, including data and models that are yet inadequate for Recommendation status. As far as possible, the prediction methods are evaluated by testing with measured data from the data banks of SG 3, and the results are used to indicate the accuracy of the prediction methods and the variability of the measured data.

This Handbook addresses propagation impairments for systems operating above 100 MHz; this includes all current frequency allocations for satellite systems.

The importance of a particular propagation impairment to an Earth-space telecommunication system depends on wave frequency and polarization, path geometry (e.g., elevation angle of the path), system performance objectives, achievable performance margins, details of the system configuration (e.g., whether dual-polarized operation is intended), and local ionospheric and meteorological features. For example, rain attenuation is often the dominant path impairment at frequencies above about 10 GHz, but is of negligible consequence for a mobile-satellite system operating at 1.5 GHz. Conversely, surface reflections, shadowing and blockage are of paramount importance for a mobile system, but seldom critical for a terminal operating in the FSS, for which terminal placement can be planned to minimize such effects.

Table 1.1 identifies the relevant propagation effects along with those systems for which the effect is of significant importance.

This Handbook for Earth-space propagation deals only with the propagation effects on the wanted signal. The exception is path depolarization which, although of concern only from the standpoint of interference (e.g., between orthogonally-polarized signal transmissions), is addressed because it can be related statistically to the propagation impairments of the co-polarized direct signal.

To conform with the format of the corresponding Recommendations, the information is arranged according to the link parameters considered in actual system planning, rather than according to the physical phenomena causing the different effects.

TABLE 1.1

**Propagation impairments affecting satellite communication systems**

<b>Impairment</b>	<b>Physical causes</b>	<b>Affected systems</b>	<b>Frequency</b>	<b>Handbook section</b>
Signal attenuation, sky noise increases	Atmospheric gases, clouds, precipitation, sand and dust	All types of satellite systems	$f >$ about 10 GHz	3, 4
	Low ionospheric layers		$f <$ 70 MHz	7.3.6
Signal depolarization	Raindrops, ice crystals,	Dual-polar systems	at 6/4, 14/11 and 30/20 GHz	5
	Faraday rotation		below about 1 GHz	7.3.1
Signal scintillations (phase and amplitude)	Refractivity variations, especially at low elevation angles (below about 10°)	Low-margin systems, antenna tracking, uplink power control	$f >$ about 10 GHz	6.2
	Ionospheric refractivity variations		10 MHz - 12 GHz	7.4
Refraction, atmospheric multipath	Atmospheric gases	Systems operating at low elevation angles; antenna tracking	1 - 45 GHz	6
	Ionospheric electron distribution			7.3.5
Reflection multipath, shadowing, blockage	Objects, vegetation on Earth's surface	Mobile-satellite services		8
Propagation delays & delay variations	Free-space, variations in troposphere	TDMA & position-location systems; closed-loop adaptive control systems		6.3
	Total electron content			7.3.2
Inter-system interference	Ducting, precipitation scatter, diffraction	All types of satellite systems	6/4 GHz systems	8.2.5 (MSS); see also ITU-R Handbook on Radiowave propagation information for predictions for signal levels likely to cause interference and for evaluation of coordination distances (to be published in 1998)
	Ionospheric scattering and reflection		$f <$ 300 MHz	
Dispersion	Total electron content	Wide bandwidth systems		7.3.3

## CHAPTER 2

### PROPAGATION EFFECTS OF THE TROPOSPHERE AND THE IONOSPHERE

ITU-R Study Group 3 deals with propagation effects in all regions of the atmosphere and free space, including the Earth's ionosphere. Most of the Earth's "weather" (precipitation) occurs in the troposphere, which is the non-ionized region from the surface up to a height of about 15 km (at the equator) above the surface. The thickness of the troposphere decreases towards the poles. Propagation effects in the troposphere tend to increase in importance as the frequency increases above 1 GHz. For mobile-satellite systems, the effects of reflection from the Earth's surface are critically important at even lower frequencies.

At frequencies below about 1 GHz, the most important region of the Earth's atmosphere is the ionosphere, the ionized region of the atmosphere above the stratosphere, within which low-frequency propagation effects are quite strong. Propagation effects within the ionosphere are covered in detail in the ITU-R Handbook on the Ionosphere and its effects on terrestrial and Earth-space radiowave propagation from VLF to SHF. Those effects of significance for Earth-space paths are also covered in Chapter 7 of this Handbook.

## CHAPTER 3

### PROPAGATION LOSS

#### 3.1 Attenuation due to atmospheric gases

The gases present in the atmosphere may attenuate the electromagnetic waves. This attenuation is caused by the molecular absorption of the atmospheric constituents and is strongly frequency dependent. The main contributors to this attenuation below 70 GHz are water vapour and oxygen.

##### 3.1.1 Procedure for calculating gaseous attenuation

The procedure currently adopted in Recommendation ITU-R P.618 to derive the attenuation due to atmospheric gases is the one presented, for the simplest configuration, in Recommendation ITU-R P.676.

Equations (1) to (3) of Recommendation ITU-R P.618 are based on the assumption that the densities of water vapour and of oxygen decay exponentially, although at different rates. This first order approximation can be used for sites with an altitude of less than 1 km.

The procedure requires, as radiometeorological input, the surface water vapour density. In the absence of local measurements of this parameter, Recommendation ITU-R P.836 may be used.

For sites with altitudes greater than 1 km, or with a negative slant-path elevation, the more complete procedures adopted in Recommendation ITU-R P.676 should be used. Annex 1 of the Recommendation should be used if a highly accurate estimate of the attenuation due to gases is necessary. In this case, measurements of atmospheric profiles of pressure, temperature and humidity (e.g., radiosonde profiles) are needed.

#### 3.2 Attenuation by precipitation and clouds

##### 3.2.1 Prediction of attenuation statistics for an average year (from point rainfall rate)

Rainfall rate distribution is inhomogeneous in space and time. Rain gauge records show short intervals of higher rain rate occurring in longer periods of lighter rain. Weather radar observations show small areas of higher rain rate occurring in larger regions of lighter rain. Various precipitation models that have been developed to deal with these complexities are described in the ITU-R Handbook on Radiometeorology. Several methods have been proposed for predicting rain attenuation statistics from rainfall rate measurements near the path. The main difference in the methods is in the models used to describe the time-space structure of rainfall rate [Fedi, 1981a].

##### 3.2.1.1 Basis of prediction method for rain attenuation

The slant-path rain attenuation prediction procedure currently adopted in Recommendation ITU-R P.618 is based on the estimation of the attenuation exceeded at 0.01% of the time ( $A_{0.01}$ ) from the rainfall rate exceeded at the same time percentage ( $R_{0.01}$ ). The concept of equiprobability is not consistent with meteorological information and is not entirely satisfactory from a theoretical point of view. However, the accuracy obtained with the prediction method is consistent with the quality and variability of available rain intensity data.

For a given value of rain rate  $R_{0.01}$  the specific attenuation ( $\gamma_R$ ) is calculated and multiplied by an effective path length ( $L_{eff}$ ) to produce the corresponding value of  $A_{0.01}$ . The effective path length is the product of a path reduction factor ( $r_{0.01}$ ) and the slant path length  $L_s$ :

$$A_{0.01} = \gamma_R \cdot L_{eff} = \gamma_R \cdot L_s \cdot r_{0.01} \quad (3.1)$$

An empirical expression is used for scaling to other time percentages, in order to provide the complete rain attenuation distribution.

The set of expressions for the estimation of  $A_{0.01}$  is based on two assumptions:

- a) the spatial structure of rain can be modelled by an equivalent rain cell with a rectangular cross-section, of equivalent length  $L_0$  and effective height  $h_R - h_S$  in the plane of the path (see Figure 3.1); and
- b) the equivalent rain cell can assume any position with respect to the path with equal probability.

The expression for the path reduction factor  $r_{0.01}$  given by Equation (8) in Recommendation ITU-R P.618 is a consequence of these two assumptions. The effective path length, represented by the product  $L_s r_{0.01}$  in Equation (10), corresponds to the average length of the slant-path ( $L_s$ ) inside the equivalent rain cell assuming a constant rain rate throughout the cell.

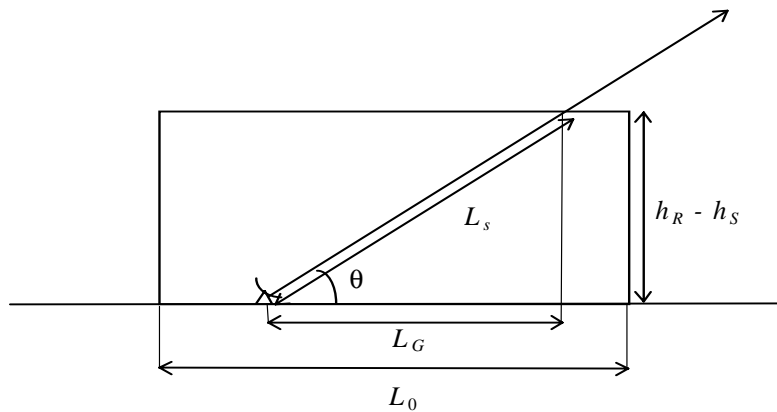


FIGURE 3.1

**Equivalent rain cell of uniform rainfall rate**

**3.2.1.2 Equivalent rain cell length**

The concept of an effective path length, to take into account the non-uniform profile of rain intensity along a horizontal path for the prediction of rain attenuation cumulative distribution on terrestrial links, is presently used in Recommendation ITU-R P.530. The effective path length in terrestrial links is the length of a hypothetical path obtained from radio data by dividing the total attenuation by the specific attenuation exceeded for the same time percentage.

The expression for the reduction coefficient relating the effective path length and the actual path length was initially supposed to depend only on the path length but has been subsequently improved, supposing a dependence also on rainfall intensity [Yamada *et al.*, 1987] in the equivalent rain cell length  $L_0$ .

The method adopted in Recommendation ITU-R P.618 was developed [Fedi, 1981b] by applying the reduction coefficient developed for terrestrial links to the portion of the Earth-space path subject to rain. This portion was calculated as the intersection of the path with the 0°C isotherm height, a preliminary expression of which was proposed as a function of latitude. In the present version, the method has been revised applying the same reduction coefficient as adopted for terrestrial links [Yamada *et al.*, 1987] only to the horizontal projection of the portion of the Earth-space path subject to rain. This portion is calculated as the intersection of the path with the effective rain height.

### 3.2.1.3 Effective rain height

In order to take the vertical structure into account various techniques have been proposed [Brussaard, 1981]. A number of these techniques are extensions of those developed for terrestrial paths [Kalinin, 1976; Morita and Higuti, 1978; Misme and Waldteufel, 1980; Fedi, 1980; Lin, 1980; Rue, 1985; García-Lopez *et al.*, 1989]. Others have been derived on the basis of extensive studies on the rain structure [Crane, 1980; Fedi and Paraboni, 1986; Leitao and Watson 1986; Rue, 1988; Li *et al.*, 1987].

In the current version of the prediction method in Recommendation ITU-R P.618, the vertical structure of rain is taken into account by the use of an effective rain height  $h_R$ , derived from experimental data, in the expression of  $L_S$ . For vertical paths the effective path length coincides with the effective rain height which, at any latitude, may differ from the 0°C isotherm height  $h_{FR}$ , as specified in Recommendation ITU-R P.839. No information is available on the behaviour of the ratio  $h_R/h_{FR}$  for the various latitudes. However, recent work by Study Group 3 suggests that it may be appropriate to use  $h_{FR}$  as the effective rain height in the model.

### 3.2.1.4 Specific attenuation

For practical applications the relationship between specific attenuation  $\gamma_R$  (dB/km) and rain rate  $R$  (mm/h) can be approximated by a power-law [Olsen *et al.*, 1978] given by Equation (9) in Recommendation ITU-R P.618. Based on an assumption of spherical drops, values of  $k$  and  $\alpha$  have been calculated at a number of frequencies between 1 and 1000 GHz for several drop temperatures and drop size distributions [Olsen *et al.*, 1978].

Values of  $k$  and  $\alpha$  for the Laws and Parsons drop-size distribution and a drop temperature of 20°C have also been calculated by assuming oblate spheroidal drops aligned with a vertical rotation axis and with dimensions related to equal volume spherical drops [Fedi, 1979; Maggiori, 1981]. Values for horizontal and vertical polarizations are presented in Table 1 of Recommendation ITU-R P.838.

Values of  $k$  and  $\alpha$  at frequencies other than those in the table can be obtained by logarithmic interpolation for  $f$  and  $k$ , and a linear interpolation for  $\alpha$ . For linear and circular polarization, Recommendation ITU-R P.838 provides approximate expressions to calculate  $k$  and  $\alpha$  from values for horizontal and vertical polarizations.

Other measurements [Manabe *et al.*, 1987; Zakharyan *et al.*, 1989] suggest that, above about 40 GHz, the values of  $k$  in Table 1 of Recommendation ITU-R P.838 may be underestimated and the values of  $\alpha$  are overestimated. This result may indicate that the Laws and Parsons drop-size distribution is not appropriate at frequencies above about 40 GHz.

A more detailed discussion of the relation between specific attenuation and rain rate is given in the ITU-R Handbook on Radiometeorology.

### 3.2.2 Long-term frequency and polarization scaling of rain attenuation statistics

The method of § 2.2.1 of Recommendation ITU-R P.618 may be used to investigate the dependence of attenuation statistics on elevation angle, polarization and frequency, and is therefore a useful general tool for scaling of attenuation according to these parameters.

If only attenuation data measured at one frequency are available, the empirical formula (14) in Recommendation ITU-R P.618, giving an attenuation ratio directly as a function of frequency and attenuation, may be applied for frequency scaling on the same path in the frequency range 7 to 50 GHz. The formula was found to be the best analytical fit to the available scaling data [Boithias, 1989]. As the accuracy of this procedure is within 10%, frequency scaling should be preferable, where applicable, to predictions using rain rate data.

Frequency scaling is examined in greater detail in the ITU-R Handbook on Radiometeorology, which gives an alternative method that makes use of the  $k$  and  $\alpha$  values and is therefore more appropriate where polarization scaling is required. Some other methods use attenuation statistics measured at two frequencies or information on the elevation angle to predict the attenuation at another frequency.

### 3.2.3 Seasonal variations - worst month

System planning often requires the attenuation exceeded for a time percentage  $P_w$  of the “worst month” (see Recommendation ITU-R P.581). The conversion from annual statistics to “worst month” statistics is discussed in detail in the ITU-R Handbook on Radiometeorology. The relationship between  $P_w$  and the annual time percentage,  $P$ , can be expressed as:

$$P = Q_1^{\frac{-1}{1-\beta}} P_w^{\frac{1}{1-\beta}} \quad (3.2)$$

The above expression is applicable for the time percentage range ( $0.001\% < P < 3\%$ ). Values of  $Q_1$  and  $\beta$  measured in various locations and for several propagation effects are given in the ITU-R Handbook on Radiometeorology. For global planning purposes, a single “average” relationship may be preferable, using  $Q_1 = 2.85$  and  $\beta = 0.13$ , which yields

$$P = 0.3 P_w^{1.15} \quad (3.3)$$

for  $1.9 \times 10^{-4} < P_w \% < 7.8$ .

Measurements obtained in a variety of climates indicate that the ratio of average yearly worst-month time percentage to average yearly time percentage depends somewhat on the climate. The above equation corresponds to climates with relatively small seasonal variations in rainfall intensity. Values of  $\beta$  and  $Q_1$  for several regions of the world are given in Table 1 of Recommendation ITU-R P.841.

### 3.2.4 Discussion of model evaluation (testing)

Testing criteria for comparing prediction methods, including the definition of a test variable for comparing rain attenuation predictions, are provided in Recommendation ITU-R P.311. Extensive tests performed on the basis of available methods and data suggest that the method of § 2.2.1 of Recommendation ITU-R P.618, provides an attainable r.m.s. accuracy of about 35% - 40% on a global basis. Additional long-term statistical data, especially from tropical regions, are needed to improve the prediction method.

### 3.2.5 Example calculation

For a satellite link from a given location, the following parameters are required:

Location: (Rio de Janeiro)

latitude:  $22^{\circ} 54' 10''$  S

longitude:  $43^{\circ} 12' 28''$  W

$h_s = 30$  m (height above mean sea level of the earth station)

Satellite: (hypothetical)

longitude:  $53^{\circ}$  W

frequency: 12 GHz

polarization: vertical

Path elevation  $\theta = 60.905^{\circ}$

Rain data:  $R_{0.01} = 70.4$  mm/hr (point rainfall rate for 0.01 % of time of an average year)

This value is the rainfall rate exceeded during 0.01% of one-year, obtained from measurements at the site, as the average of the values for each measurement year. For sites where this value is not available, it can be obtained from Table 1 of Recommendation ITU-R P. 837. The rain climatic zone to be chosen in the table is obtained from Figures 1 to 3 of Recommendation ITU-R P. 837.

Once the required parameters are available, application of the step-by-step attenuation prediction method of 2.2.1.1. in Recommendation ITU-R P.618 is quite straightforward, as illustrated here:

*Step 1:* The effective rain height,  $h_R$ , for the latitude  $\varphi$  of the station is

$$h_R \text{ (km)} = 3.0 + 0.028\varphi = 3.64 \text{ km}$$

*Step 2:* The slant-path length,  $L_s$  is

$$L_s = \frac{(h_R - h_s)}{\sin \theta} = 4.13 \text{ km}$$

*Step 3:* The horizontal projection,  $L_G$ , is

$$L_G = L_s \cos \theta = 2.0 \text{ km}$$

*Step 4:* The rain intensity,  $R_{0.01}$ , exceeded for 0.01% of an average year is 70.4 mm/hr

*Step 5:*  $L_0$  is

$$35 \exp(-0.015R_{0.01}) = 12.17$$

The reduction factor  $r_{0.01}$ , for 0.01% of the time is given by

$$r_{0.01} = \frac{1}{1 + L_G/L_0} = 0.858$$

Step 6: The specific attenuation,  $\gamma_R$ , using the frequency-dependent coefficients, given in Recommendation ITU-R P.838, and the rainfall rate,  $R_{0.01}$ :

$$\gamma_R = k(R_{0.01})^\alpha = 2.769$$

Step 7: The predicted attenuation exceeded for 0.01% of an average year is

$$A_{0.01} = \gamma_R L_s r_{0.01} = 9.8 \text{ dB}$$

Step 8: The estimated attenuation to be exceeded for other percentages of an average year, in the range 0.001% to 1% is

$$A_p = A_{0.01} \cdot 0.12 \cdot p^{-(0.546+0.043\log(p))}$$

The cumulative distribution is shown in Figure 3.2.

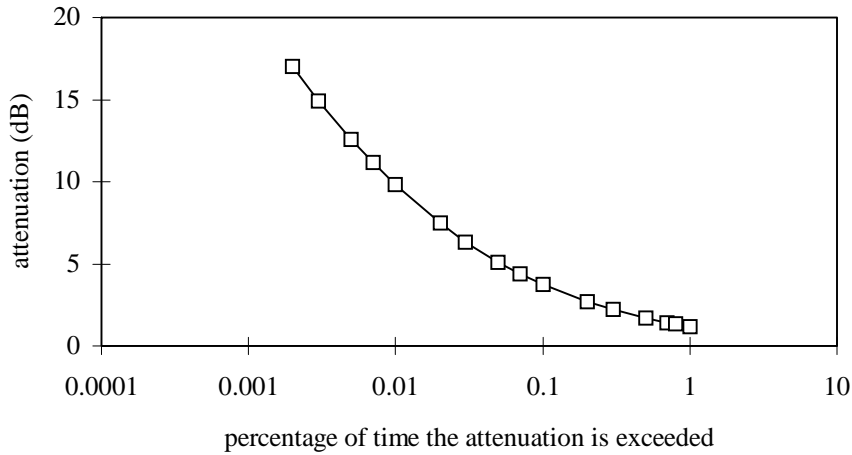


FIGURE 3.2

**Example of rain attenuation statistics**

**3.2.6 Cloud attenuation**

The formation of clouds can be due to a variety of atmospheric processes, which result in cloud layers at many altitudes. The World Meteorological Office (WMO) specifies nine different cloud types for each of three cloud heights: low, middle, and high. Based on observations using these WMO classifications, maps of cloud cover have been prepared [Warren *et al.*, 1986] that show that clouds of one type or another exist on average for 53% of the time over land. Any satellite-to-ground link needing to maintain communications for a large fraction of the time will, therefore, have to be designed to operate through clouds.

Attenuation due to clouds on Earth-space microwave links is not usually a significant factor for high availability services (99.96% link up-time in an average year; 0.2% down-time in an average worst-month for a one-way connection). The additional margin required for clouds over that necessary to counteract rain attenuation is relatively small. On the other hand, if a low-fade margin system is employed, attenuation due to clouds could be significant at frequencies above about 10 GHz.

Large cumulus clouds, for instance, can cause more than 2 dB of attenuation on paths with elevation angles below 5° at frequencies around 11 GHz. Cloud maps indicate [Warren *et al.*, 1986] that cumulus clouds exist on average for 5% of the time over land, a significant fraction of time for any service requirement. As the clouds become more laden with water, the likelihood of precipitation increases, as does the risk of encountering significant path attenuation on the link. Most likely, at very low elevation angles tropospheric scintillation will be of greater significance than cloud losses.

Recommendation ITU-R P.840 gives a prediction method for the attenuation due to clouds and for fog, which may be of concern above about 100 GHz. This model relies on the underlying physical mechanism of Rayleigh scattering by droplets and requires a knowledge of the liquid water content of the cloud.

### **3.3 Diversity and spatial features of rain**

Local weather patterns are affected significantly by the terrain over which they flow. The small-scale fluctuations in these patterns can lead to substantial differences in rainfall from place to place. The small-scale differences in rainfall patterns can be reflected in corresponding differences in path attenuation with respect to location (i.e., from site to site) or direction of observation (i.e., from azimuth to azimuth at the same site).

It is not unusual for there to exist areas of rain shadow or enhanced rain production that are geographically close to each other (< 30 km). One such example was obtained during the ATS-6 experimental campaign in Europe while the satellite was stationed at 35°E longitude [Allnutt and Shutie, 1977]. Consistent differences in cumulative rainfall rate statistics from site to site over a small area can be used with advantage to select a preferred earth station location. The site with the lowest rainfall rate statistics is usually preferred.

If the link to the satellite must pass through a region of enhanced rainfall production, however, some of the advantage of selecting an optimum site can be lost. Such a situation was noted in an experiment during the SIRIO and OTS campaigns [Rucker, 1980]. A ridge of hills about 200 m in height roughly parallel to the azimuth angle to the SIRIO satellite caused appreciably more rainfall to occur along that path than on the path to the OTS satellite which was essentially over the floor of a valley.

Of more significance for high-availability services, however, are temporal differences in rain rate over small distances. This aspect can be used with advantage to reduce the net attenuation experienced along a slant path if more than one site is used simultaneously. The technique is referred to as site diversity or path diversity [Hogg, 1967].

#### **3.3.1 Site diversity**

Path diversity in telecommunications systems involves the provision of alternate propagation paths for signal transmission, with the capability to select the least-impaired path when conditions warrant. For satellite communications systems, implementation of path diversity requires the deployment of two or more interconnected earth terminals at spatially separated sites, hence the use of the term “site diversity”. A pictorial representation is shown in Figure 3.3.

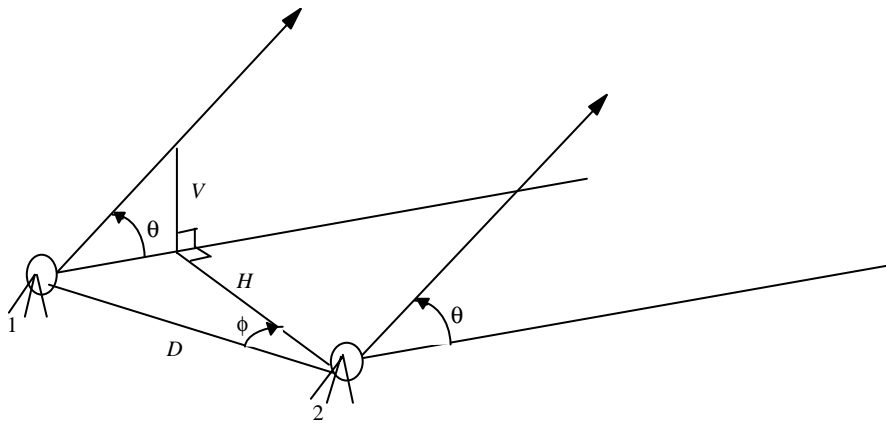


FIGURE 3.3

**Dual-site diversity configuration**

**$H$  and  $V$  are horizontal and vertical path separations, respectively**

Measurements [Wilson and Mammel, 1973; Witternigg *et al.*, 1993] and analysis [Hodge, 1974] indicate that the additional availability obtained by simultaneously operating with more than two terminals is small. Implementation of additional diversity terminals to operate with a main station would also be complex and expensive. Recently, however, there has been interest in achieving relatively high availability ( $> 99.9\%$ ) for Very Small Aperture Terminals (VSATs) in the 14/11 GHz or 30/20 GHz bands by operating a number of VSATs interconnected via a Metropolitan Area Network (MAN) using a Wide Area Diversity (WAD) network controller [Allnutt, 1993]. Each VSAT would act as a transparent resource for any user connected to the MAN and would be activated via the WAD controller as the weather and/or traffic situation demanded. Experiments to determine the feasibility of VSAT WAD techniques over MANs are planned at both 14/11 GHz and 30/20 GHz.

From a meteorological perspective, however, there is little additional information to be gained from conducting multi-site (three, or more, terminal) diversity experiments if orographic features do not suggest such a configuration. The emphasis of investigations has therefore concentrated on dual-site diversity configurations for satellite communications.

There are several factors that may affect the performance of a particular dual-site diversity installation. These include:

- a) Terminal separation,  $d$ ;
- b) Path geometry (elevation angle  $\theta$  and azimuth angle  $\phi$ );
- c) Local meteorological characteristics (rainfall rate statistics, degree of convectivity, rain cell dimensions and shapes, relative cell separation, etc.);
- d) Frequency,  $f$ ;
- e) Orientation of the baseline joining the sites; and
- f) Local topographical features.

Interrelationships exist between these parameters, shown pictorially in Figure 3.4, so that isolating the dependence of diversity behaviour on any one of them is difficult. These aspects are considered in § 3.3.1.7.

The statistical presentation of joint path attenuation statistics and the calculation of the diversity performance depend somewhat on the reference distribution selected.

### 3.3.1.1 Reference distribution

Ideally, if the least-impaired path of a diversity configuration could always be successfully identified and selected for communications, the cumulative distribution defined at each time percentage by the lesser of  $A$  and  $B$  in Figure 3.5 would constitute a more reasonable reference distribution than does the mean single site distribution. Diversity performance would then be less than computed from the mean single-path attenuation, which presents an apparent paradox: Why does not perfect switching between diversity paths maximize the available diversity performance?

In fact, such switching does maximize the diversity performance but the results are reflected in the diversity (joint) distribution of Figure 3.5. The assumption of perfect switching is implicit in available data, which are processed by selecting the smallest path attenuation for each sampling interval to compile the joint attenuation distribution. Diversity combining would also achieve the goal of “perfect switching” since the stronger of the two signals would always be used as the reference. For analogue signals, very accurate phase control is required to achieve diversity combining and so tends to be limited to fairly narrow-band applications.

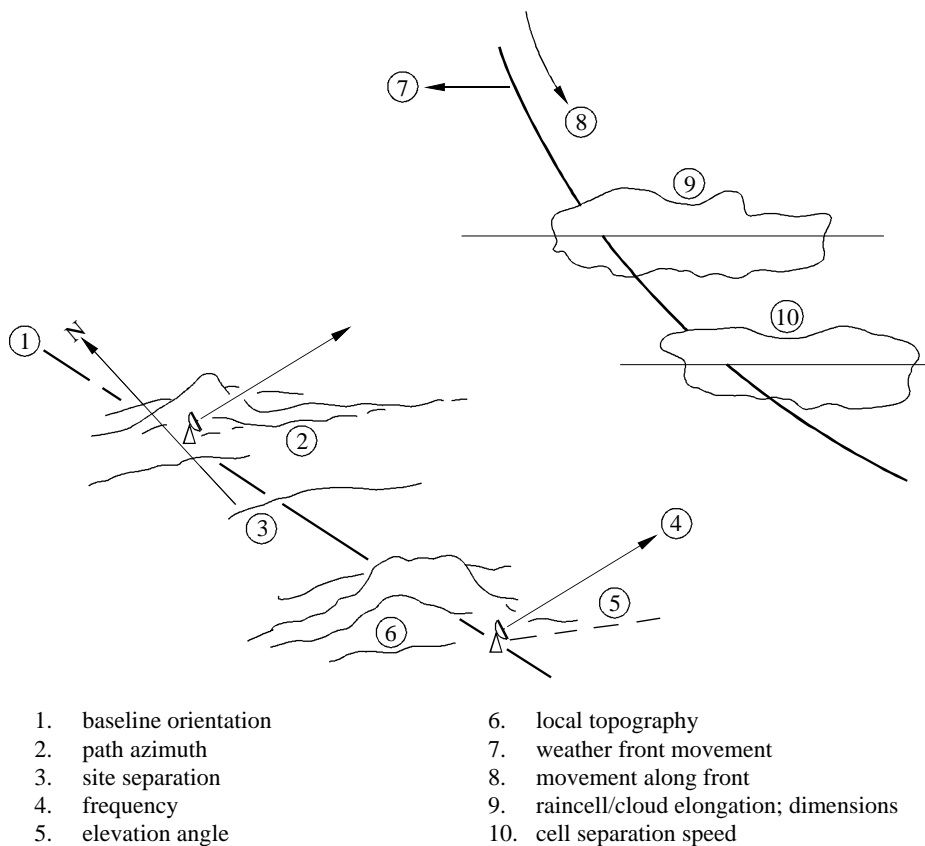


FIGURE 3.4

### Factors affecting site diversity performance

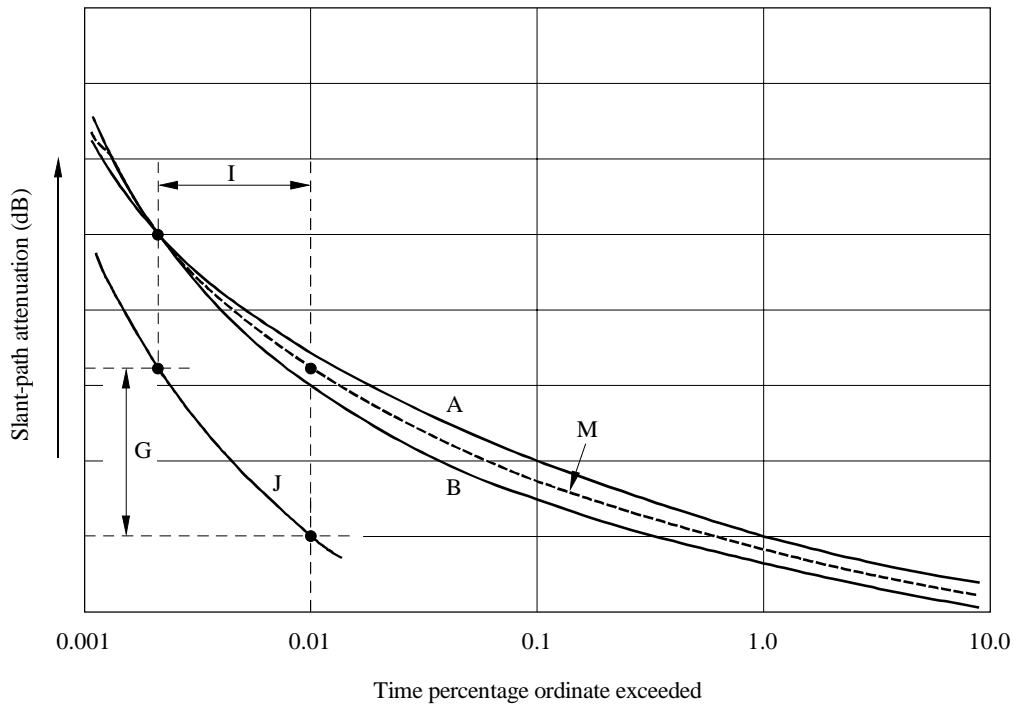


FIGURE 3.5

### Illustration of diversity parameters

In operating systems, switching will be performed in accordance with an algorithm designed to minimize the number of switches and consequent probability of a temporary link interruption while maintaining acceptable service [Wallace and Carr, 1982]. Thus switching will usually be avoided, even if the primary link is impaired, provided the path is available with some reasonable reserve margin. In any case, measurement inaccuracies in the monitoring equipment will inevitably introduce errors in establishing the least-impaired path and therefore in switching efficiency. The joint attenuation distribution achievable with perfect switching will not be attained in such circumstances. The degree to which it will be achieved is a function of the switching strategy and the measurement accuracy of the equipment.

The above considerations render the details of the reference distribution somewhat moot for many applications. In practice, the mean single-site attenuation is a convenient reference that presumably averages out some of the experimental inaccuracies and inter-annual variabilities of the measured statistics for the individual paths.

Two standard statistical approaches exist for relating the mean single-site and diversity attenuation distributions, as illustrated in Figure 3.5: Diversity improvement factor and diversity gain.

#### 3.3.1.2 Diversity improvement factor

A hypothetical, but representative, example of cumulative distributions of 11 GHz rain attenuation for two single paths (*A* and *B*), and for the diversity (joint) distribution (*J*) constructed from the concurrent fading records for paths *A* and *B* by selecting the lesser attenuation for each data sample, is shown in Figure 3.5.

The mean (average) of the two values of rain attenuation at each time percentage defines the mean single-site attenuation distribution (dashed line in Figure 3.5), which is commonly used as a reference distribution for classifying diversity performance.

The diversity improvement factor [Wilson and Mammel, 1973] (or diversity advantage [Hodge, 1974]),  $I$ , is defined as the ratio of the single-path  $p_m$  and diversity  $p_{div}$  time percentages for a specified rain attenuation,  $A$ :

$$I(A) = \frac{p_m(A)}{p_{div}(A)} \quad (3.4)$$

A model for the diversity improvement factor,  $I$ , is described in § 2.2.4.1 of Recommendation ITU-R P.618.

### 3.3.1.3 Diversity gain

Diversity gain,  $G$ , is defined [Altman and Sichak, 1956; Hodge, 1973] in an orthogonal sense to diversity advantage, and is the difference (in dB) between the single-path and diversity rain attenuations for a given time percentage,  $p$  (see Figure 3.5):

$$G(p) = A_m(p) - A_{div}(p) \quad (3.5)$$

Diversity gain may be estimated for a given dual-site diversity configuration by applying the model given in § 2.2.4.2 of Recommendation ITU-R P.618.

### 3.3.1.4 Instantaneous diversity gain

An additional quantity called “instantaneous diversity gain” has been proposed [Towner *et al.*, 1984] to characterize diversity performance. For an  $N$ -site diversity configuration, the instantaneous diversity gain at time  $t$  is defined as:

$$G_i(t) = A_{max}(t) - A_{min}(t) \quad (3.6)$$

where  $A_{max}(t)$  and  $A_{min}(t)$  are the maximum and minimum values of the  $N$  single-path attenuations at time  $t$ . For a dual-site diversity configuration,  $G_i(t)$  is simply the positive difference between the two path attenuations at any instant.

Diversity gain supplies no instantaneous information, but it does supply the basic statistical information required to design a diversity system. Processing the data on the basis of instantaneous diversity gain loses the basic data required for system design, which is the additional (statistical) availability or fade margin provided by diversity, not the instantaneous difference between attenuations.

### 3.3.1.5 Comparison of diversity improvement factor and diversity gain as measurement parameters

One merit of the diversity improvement factor is that it can be determined for the small time percentages of the diversity distribution. Conversely, it cannot be evaluated for large single-site attenuations. For diversity gain, the regions of applicability are just reversed.

Diversity gain and improvement are both defined by the same cumulative distributions and are, in a sense, equivalent. However, as has been noted [Hodge, 1974], the single-path and diversity attenuations used to calculate diversity improvement correspond to different time percentages, and thus to different statistical reliabilities. In particular, attenuations for the small time percentages of the diversity distribution may be subject to large statistical uncertainties, which will be reflected in the improvement factor. Experimentally determined diversity improvement factors [Allnutt, 1978; Lin *et al.*, 1980] do, in fact, reveal somewhat irregular, scattered behaviour, whereas diversity gain typically exhibits more-or-less predictable characteristics [Allnutt, 1978; Hodge, 1976]. Diversity gain thus appears to be the parameter of choice for specifying diversity performance.

### 3.3.1.6 Example calculations using the recommended site diversity prediction procedures

#### 3.3.1.6.1 Diversity improvement factor

In Recommendation ITU-R P.618, the diversity improvement factor,  $I$ , is given by Equation (16), where  $p_1$  and  $p_2$  are the respective single-site and diversity time percentages, and  $\beta$  is a parameter depending on link characteristics. The approximation

$$I \approx \left[ 1 + \frac{100\beta^2}{p_1} \right] \quad (3.7)$$

from Equation (16) of Recommendation ITU-R P.618 is acceptable in nearly every case since  $\beta$  is generally small.

From a large number of measurements carried out in the 10-20 GHz band, and mainly between 11 and 13.6 GHz, it has been found that the value of  $\beta^2$  depends basically on the distance between the earth stations,  $d$  (km), and only slightly on the angle of elevation and the frequency. It is found that  $\beta^2$  can be expressed by the empirical relationship found in Equation (17) of Recommendation ITU-R P.618.

There is some evidence to suggest that this equation can be modified to account for the influence of varying elevation angles by using the following expression:

$$\beta^2 = 10^{-4} (\sin \theta)^{0.5} d^{1.5} \quad (3.8)$$

but this relationship has yet to be verified fully.

Figure 3.6 shows  $p_2$  versus  $p_1$  on the basis of Equations (16) and (17) of Recommendation ITU-R P.618.

Figure 3.7 presents the data obtained using sites 3 and 4 in an experiment in Graz, Austria, at a frequency of 12 GHz [Witternigg *et al.*, 1987]. The inset in Figure 3.7 is the layout of the network of four radiometer sites. The separation of these two sites was 15.4 km with an elevation angle of 26.4° and the angle between the azimuth and baseline orientation was almost 90°.

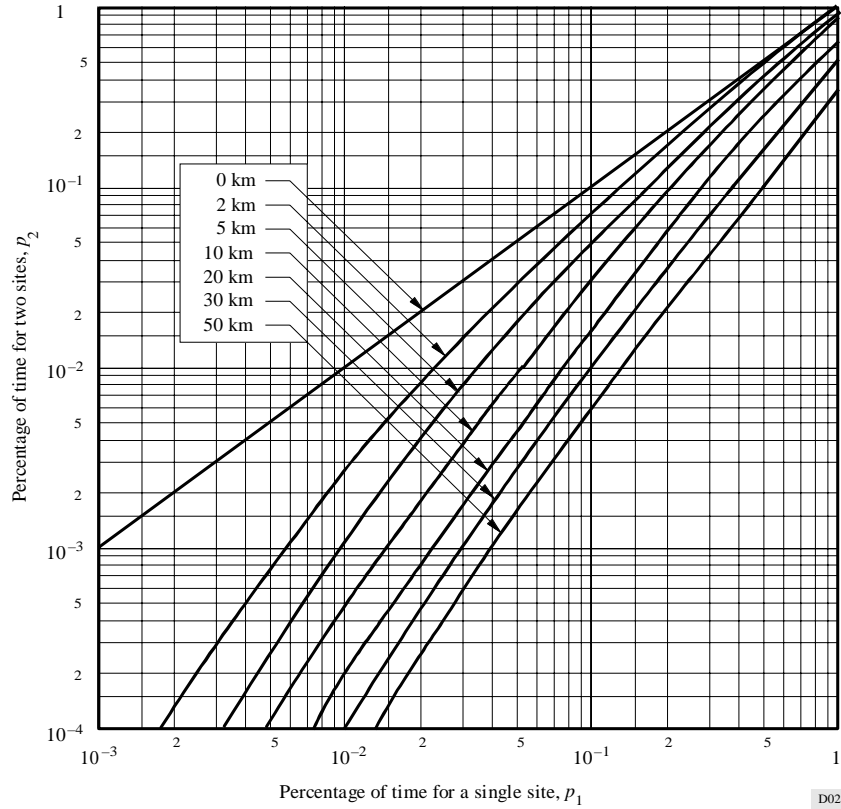


FIGURE 3.6

**Relationship between time percentages with and without site diversity for the same attenuation**

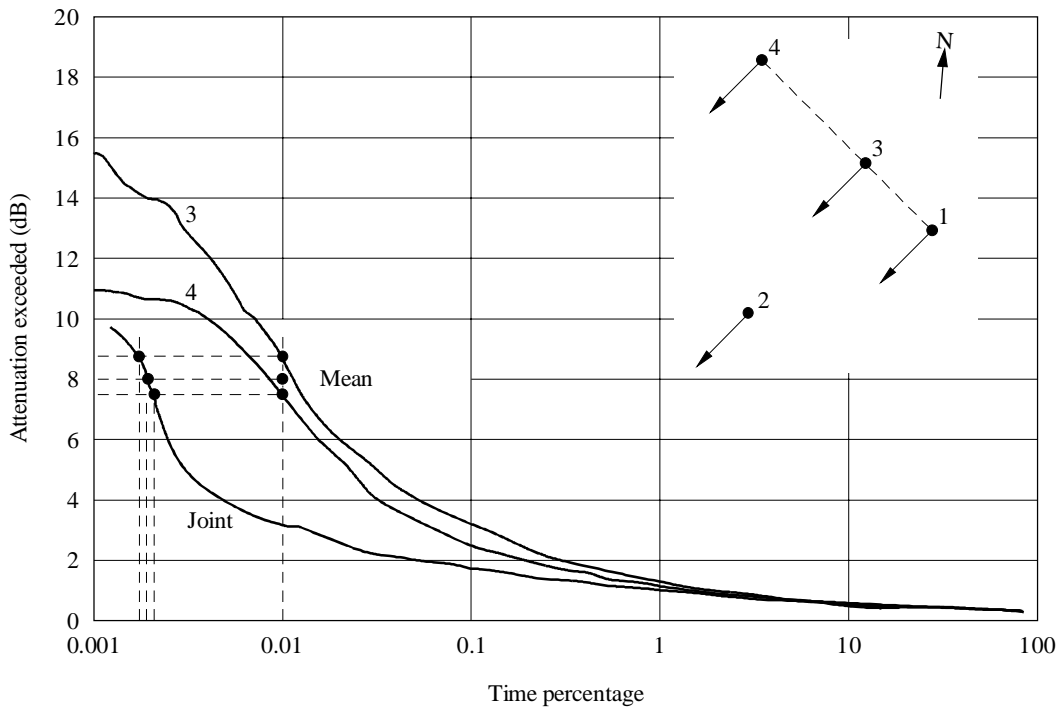


FIGURE 3.7

**Some results from two sites in a 12 GHz quadruple site diversity experiment at Graz, Austria [Witternigg *et al.*, 1987]**

With a site separation of 15.4 km,  $\beta^2 = 0.00386$  from Equation (17) of Recommendation ITU-R P.618. Upon inserting this value of  $\beta^2$  into Equation (16) for a mean single-site attenuation of 8 dB, which occurs at a time percentage  $p_1 = 0.01\%$ , there results:

$$I = 1 + (100 \times 0.00386)/0.01 = 39.6 \quad (3.9)$$

From Figure 3.7, the measured diversity advantage for the single-site time percentage of 0.01% is  $0.01/0.002 = 5$ . Note that the mean single-site characteristic has been used rather than either of the single-site distributions (as noted earlier in § 3.3.1.1).

In this example, the calculated diversity advantage is much larger than the measured value, which may be due to the limited data sample (the results in Figure 3.7 are for a single year of the experiment). In Figure 3.7 the joint path attenuation characteristic does not follow the same trend at low time percentages as that of the two single-site characteristics. In many respects, this highlights the variability in using diversity advantage as a method for predicting site diversity performance.

### 3.3.1.6.2 Diversity gain

Recommendation ITU-R P.618 provides a procedure for calculating the diversity gain,  $G$ , between pairs of earth station sites using the following parameters:

- $d$ : separation between the two sites (km)
- $A$ : path attenuation due to rain for a single site (dB)
- $f$ : frequency (GHz)
- $\theta$ : path elevation angle (degrees)
- $\psi$ : angle made by the azimuth of the propagation path with respect to the baseline between sites, chosen such that  $\psi \leq 90^\circ$  (degrees)

In the prediction procedure in Recommendation ITU-R P.618, the gain  $G_d$  contributed by the spatial separation of the earth station sites at a separation  $d$  (km) is computed with Equation (18); the gain  $G_f$  contributed by the frequency-dependent term is given by Equation (19); the gain  $G_\theta$  contributed by the elevation angle element is given by Equation (20); and the gain  $G_\psi$  contributed by the baseline-dependent element is given by Equation (21). The overall diversity gain,  $G$ , is calculated as the product of the four diversity gain elements:

$$G = G_d G_f G_\theta G_\psi \quad \text{dB} \quad (3.10)$$

When the above method was tested against the ITU-R SG 3 site-diversity data bank, the arithmetic mean and standard deviation were found to be 0.14 dB and 0.96 dB, respectively, with an r.m.s. error of 0.97 dB. More recently [Allnutt, 1993] it has been found that the above diversity gain prediction procedure tends slightly to overestimate at low levels of single site attenuation (i.e., predicts a higher gain than is obtained in practice) and slightly to underestimate at high levels of single site attenuation (i.e., predicts a lower gain than is obtained in practice). The method seems to achieve its highest accuracy at single-site fade levels corresponding to 0.01% of an average year, which is a critical time percentage for high availability satellite systems.

As with the sample calculation of diversity advantage given above, diversity gain will be calculated for the same pair of sites and the same set of data (see Figure 3.7). From the diversity gain procedure outlined above, with  $d = 15.4$  km;  $f = 12$  GHz; elevation angle  $\theta = 26.4^\circ$ ; and the angle between the baseline azimuth and the look-angle azimuth  $\psi = 90^\circ$ , Equations (18)-(21) of Recommendation ITU-R P.618, respectively, yield:

$$a = 5.1047 \text{ and } b = 0.3249, \text{ hence}$$

$$G_d = 5.0704, G_f = 0.7483, G_\theta = 1.1584, G_\psi = 1.18$$

From Equation (22) for diversity gain, the estimated gain is computed to be  $G = 5.2$  dB.

From Figure 3.7, the measured diversity gain at a time percentage of 0.01% is  $8 - 3.1 = 4.9$  dB. As noted earlier, diversity gain is a relatively stable parameter from year to year. In this case, the difference between the measured and predicted diversity gain was  $\approx 0.3$  dB, an error of about 6%.

### 3.3.1.7 Factors affecting site diversity performance

A variety of site diversity measurements have been performed and are summarized in several references (e.g., Hodge, 1982; Ippolito *et al.*, 1983; Rogers and Allnutt, 1984). Many of the parameters potentially affecting a site diversity installation are interrelated (e.g., baseline orientation, path geometry, and local terrain) and some of these relationships will be noted.

#### 3.3.1.7.1 Dependence on site separation

The concept of site diversity is based on the assumption that propagation impairments on different paths are more or less uncorrelated for sufficient spatial separations between paths. Conversely, propagation degradations for identical paths (i.e., parallel paths with zero separation) are completely correlated. Between these limits, site (or path) separation must be a strong determinant of diversity gain. Not unexpectedly, measurements show that site separation,  $d$ , is the controlling factor in diversity performance for separations of less than 10 to 20 km [Hogg, 1967; Wilson and Mammel, 1973; Rogers and Allnutt, 1984].

The dependence of diversity gain,  $G$ , on site separation is illustrated in Figure 3.8 [Hodge, 1976], based on data at three frequencies from Ohio and New Jersey (USA). Diversity gain is observed to increase rapidly as  $d$  increases from zero until the separation exceeds 10 to 15 km, after which benefits from further increases in  $d$  become small. The site separation for which 95 percent of the available diversity gain is achieved varies somewhat among different measurements, ranging from about 15 km to about 30 km [Hodge, 1978]. These differences may be due to influences of parameters other than site separation, such as configuration geometry, climatic differences, or terrain effects. Data from an 11.6 GHz radiometric site diversity experiment in the UK [Hall and Allnutt, 1975] show similar trends. A comparison of the two sets of data is shown in Figure 3.9, and some interesting differences are apparent between the results.

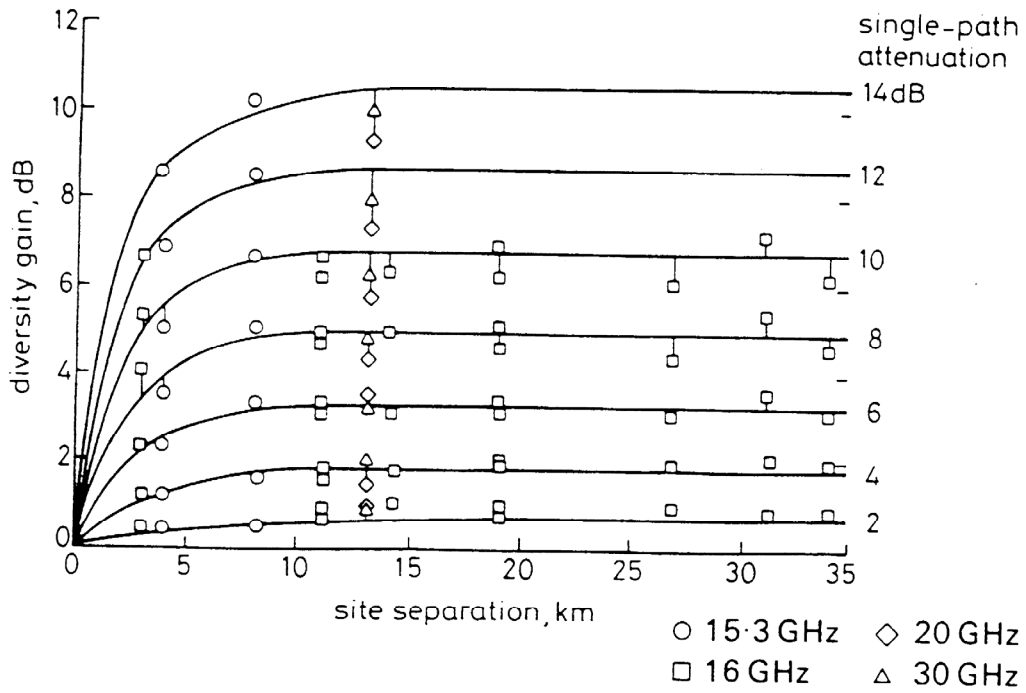


FIGURE 3.8

**Diversity gain vs. site separation**

Copyright 1976 IEEE [Hodge, 1976]

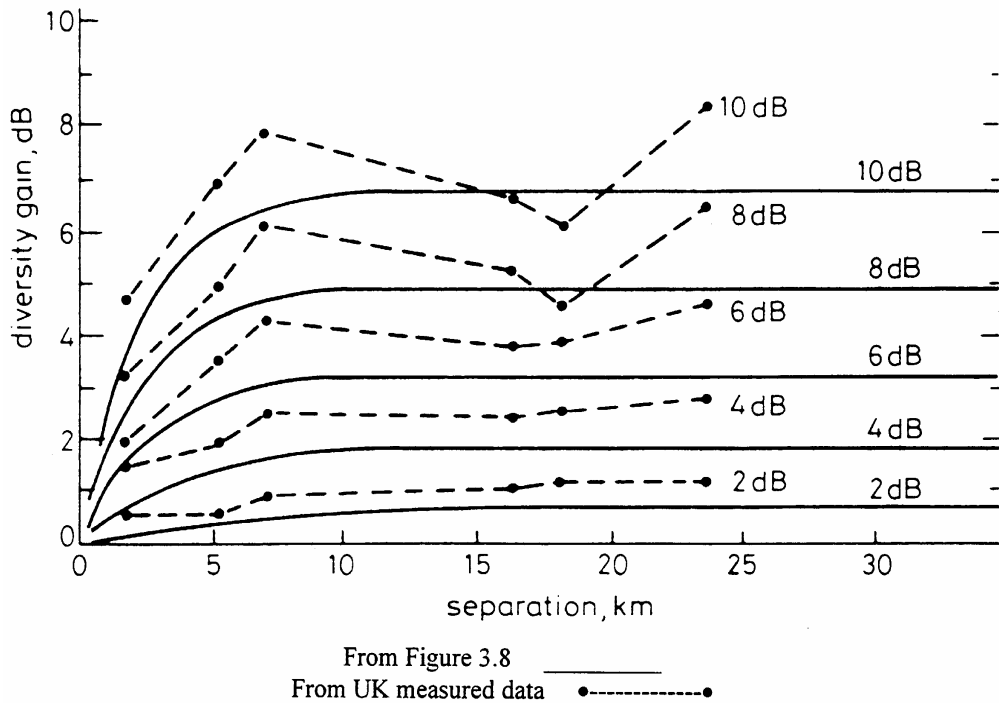


FIGURE 3.9

**Diversity gain vs. site separation: comparison of USA and European data**

(Reproduced with permission from INTELSAT and COMSAT)

In general, diversity gain in the UK experiment seems to exceed that for the USA experiments, supporting the argument that, for a given site separation, diversity gain decreases as frequency increases. The dependence is fairly weak, however, especially at the elevation angles ( $25^\circ$  to  $55^\circ$ ) used in these experiments.

Also, in agreement with other European data [Witternigg *et al.*, 1993, 1987], the increase in diversity gain with increasing site separation seems to be significantly higher in the UK experiment than that observed in the USA data for small site separations. More significantly, there is a distinct drop in diversity gain in the UK experiment for site separations between 7 and 18 km, which occurred because two independent, intense rain cells traversed the site diversity network and caused simultaneous rain fades at the widely-spaced sites.

The observed dependence of diversity gain on site separation is consistent with joint probability characteristics of point rainfall rate. Both quantities show rapid decorrelation with increasing site separation, until "saturation" effects begin to limit the quantity to a value corresponding to somewhat less than complete decorrelation [Rogers, 1976; Barbaliscia and Paraboni, 1982]. Concurrent path attenuation and point rainfall rate statistics for diversity sites often show comparable behaviour, suggesting that joint rainfall rate statistics may be used to predict site diversity performance, analogous to the predictive techniques used to convert point rainfall rate statistics to single-path attenuation statistics [Allnutt, 1978].

Because the rain medium is bounded in the vertical direction, and the precipitation pattern in the horizontal plane is often banded, it is possible that separation (both vertical and horizontal) of the radio paths may be more important than the physical site separation [Rogers and Allnutt, 1984]. The geometry for the perpendicular path separation is illustrated in Figure 3.4, which also demonstrates the interdependence of the path separations on baseline orientation, path azimuth, and path elevation angle.

For a specific configuration, local terrain and climatic factors (e.g., alignment between configuration geometry and the directions of local weather fronts, or any regional anisotropy in rain structures) may also be related to path separation. Such effects are not yet fully understood. However, it has been concluded [Rogers, 1976] from meteorological considerations that horizontal increases in path separation were more useful than equivalent vertical increases for reducing the probability of simultaneous path impairments, at least for latitudes below 60 degrees and elevation angles above 3 degrees. For elevation angles less than about  $3^\circ$ , tropospheric scintillation is so severe that height diversity schemes may be needed to increase the performance and availability margins of the link [Acampora, 1981; Allnutt, 1993].

### **3.3.1.7.2 Baseline orientation effects**

As noted above, meteorological considerations [Rogers, 1976] imply that maximizing the horizontal path separation (for a specified site separation) will maximize diversity gain. From Figure 3.4, the maximum horizontal path separation is achieved by orientating the diversity baseline perpendicular to the path azimuth. Data from a three-site 15.5 GHz radiometric experiment in New Jersey [Gray, 1973] and from a six-site network of 11.6 GHz radiometers near Slough, UK [Hall and Allnutt, 1975] support this view. A later survey [Allnutt, 1978] also concluded that the preferred baseline orientation was normal to the radio path. It has been surmized [Hogg and Chu, 1975], however, that orientating the baseline normal to the radio path, and secondarily to the direction of travel of

convective weather fronts, would be the most beneficial for site diversity applications. This idea is supported by extensive measurements in the USA [Lin *et al.*, 1980].

Radar simulations of diversity configurations for Wallops Island, Virginia, USA, with baselines parallel to the slant path azimuths, revealed that baselines orientated perpendicular to the predominant direction of rain cell elongation were preferred [Goldhirsh, 1976]. Later measurements from the six-site diversity experiment mentioned earlier also revealed that the prevailing direction of movement of weather systems can affect diversity performance [MacKenzie and Allnutt, 1977]. Other radar simulations [Hodge, 1978; Furgusson and Rogers, 1978] and analyses [Mass, 1979], however, showed only a small dependence of diversity performance on baseline orientation.

Therefore, results are not conclusive as regards baseline orientation, which probably indicates that baseline orientation is not the dominant parameter for many diversity configurations, and that the factors potentially affecting diversity performance are sufficiently interrelated to make ascribing observed performance to a single parameter (other than site or path separation) difficult. For example, in an experiment in southern Ontario, Canada, consistently poor diversity performance was attributed to orographic rainfall induced by an escarpment parallel to the baseline [Strickland, 1977]. Possibly this topographic effect could have been negated by re-orientating the baseline perpendicular to the escarpment.

Since the probability of simultaneous path impairments must inevitably be larger for parallel baseline and path azimuths at low elevation angles (because the vertical path separations will be small), especially for small site separations, baseline orientation will be important in these cases. As the possibility of joint impairment by a single cell is high for such a configuration, the preferred baseline orientation will indeed probably be the bisector of the obtuse angle between the path azimuth and the major axis of cell anisotropy (though in general the latter information will be unknown, and may thus be ignored). For large site separations, however, variations in the joint probability are small for differing baseline orientations, as confirmed by the measured data.

### **3.3.1.7.3 Effects of path geometry**

The geometry of a radio path is defined by the path azimuth,  $\psi$ , and path elevation,  $\theta$ . For most cases, the azimuth angle dependence is covered by baseline orientation effects, since it is the relative angle between the path and the baseline that appears to be important in determining diversity gain. Azimuth effects have been shown to be significant in some cases of single-site operation [Rucker, 1980], although the effects noted may not have been as substantial in a two-site diversity experiment.

Strong elevation-angle effects on single-path propagation impairments are often observed. As the elevation angle decreases, the slant path length through the troposphere rapidly increases, thereby increasing the occurrence and severity of the single-path impairments. A concomitant increase in the probability of joint impairments is also anticipated and has been substantiated by diversity measurements. The diversity gain at 11.6 GHz for an elevation angle of  $6^\circ$  was found to be approximately half that achieved at  $30^\circ$  for a 7.1 km site separation near Slough, UK [Allnutt, 1977]. Similar diversity gain behaviour was observed on 11 GHz paths in western Japan at a  $6^\circ$  elevation angle and 17 km path separation [Rogers, 1981] and in Virginia, USA, at  $11^\circ$  and 7.3 km separation [Towner *et al.*, 1982]. These diversity gain curves are shown in Figure 3.10.

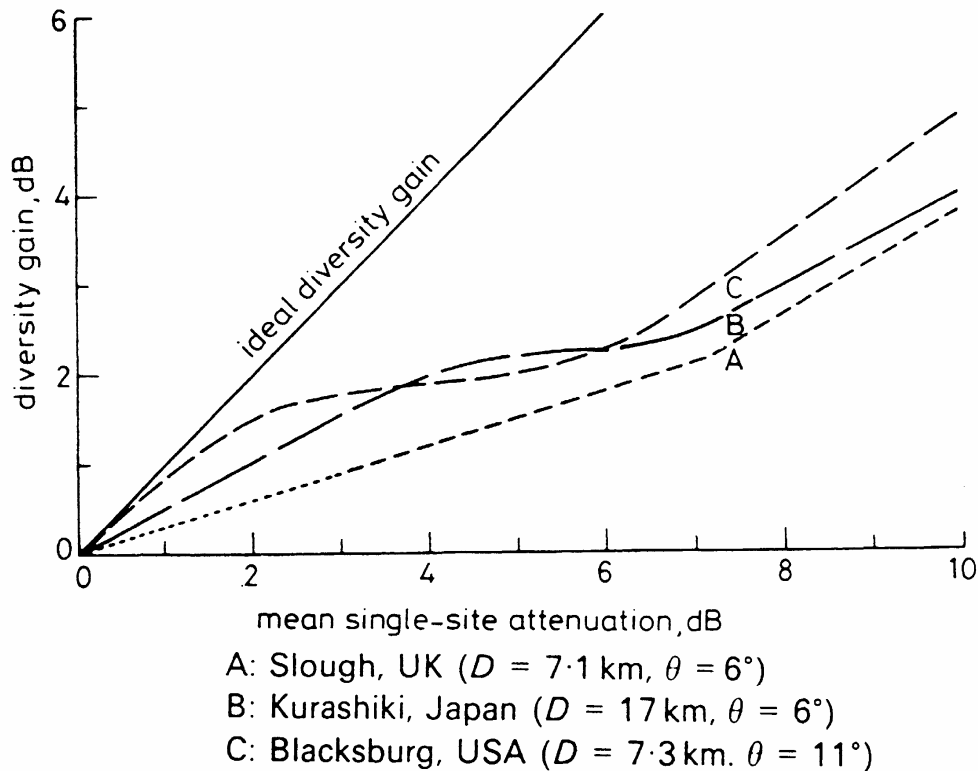


FIGURE 3.10

**Behaviour of diversity gain at low elevation angles**

(Reproduced with permission of INTELSAT and COMSAT)

The diversity gain curves are relatively flat for mean single-site path attenuations in the range of approximately 3 to 6 dB, with minimal increases in performance over this range, and sometimes a decrease that seems to be characteristic for low elevation angle experiments. The occurrence of this "flattening" in the diversity gain characteristic could be due to the simultaneous presence of two separate rain cells over the two earth stations. It is also very probable, however, that if the measurements were continued for a number of years, the flat portion would blend into the overall characteristic giving a monotonic increase in diversity gain with single-site attenuation [Witternigg *et al.*, 1987].

It is therefore considered that the apparent flattening or non-monotonic characteristic seen in low-elevation-angle site diversity experiments is due to sampling errors (insufficient data to provide a stable result). It seems clear, however, that diversity performance becomes degraded as the path elevation angle becomes smaller and, from Figure 3.10, that elevation angle may be a dominant consideration for paths with elevation angles below about 15 degrees. For higher elevation angles, diversity performance has only a weak dependence on path elevation angle.

**3.3.1.7.4 Frequency dependence**

Diversity performance is expected to decrease with increasing frequency because the impact of widespread, low rainfall rate structures on the single-path statistics will increase. These widespread phenomena are more correlated over large distances, and thus the decorrelation between paths should decrease. Early measurements of diversity gain at frequencies between 11 and 30 GHz, however, indicated that the gain appeared to be almost independent of frequency [Goldhirsh and Robison, 1975; Hodge *et al.*, 1976]. A later analysis [Hodge, 1982] of the apparent residual

frequency dependence of diversity gain (after estimated site separation effects had been deleted) also yielded weak dependence. While the frequency dependence of diversity gain has not been tested on low elevation angle paths, it is probable that for these paths, frequency effects will be important, particularly above 30 GHz, where gaseous and cloud effects become significant in terms of path attenuation.

### **3.3.1.7.5 Local meteorological and topographic effects**

Diversity performance can be influenced by local terrain, since topographic features often modify rainfall characteristics [Harrold and Austin, 1974] as noted earlier [Strickland, 1977]. Both apparent rainfall enhancement [Strickland, 1977] and rain "shadow" [MacKenzie and Allnut, 1977] can occur. Such orographic effects can be anticipated in general, although their magnitude will be difficult to predict. Interposing significant geographical features (a hill, river, lake, etc.) between sites should always increase the decorrelation between the sites [Szuppa *et al.*, 1993].

Establishing a pair of diversity terminals with a substantial difference in height above mean sea level [Otsu *et al.*, 1978] might permit greater than normal diversity gain to be achieved due to the substantially shorter path through the troposphere of the higher terminal. This result may not always occur [Misme and Waldteufel, 1982] and the advantage to be gained by siting one terminal up a mountain may be obviated by logistics, adverse weather, and other problems. There is no doubt, however, that some height separation (akin to those in terrestrial line-of-site space diversity operation) is preferred at elevation angles below 3° at high latitudes [Mimis and Smalley, 1982; Gutteburg, 1983; Bryant, 1992].

### **3.3.2 Statistical distribution of signal level for large areas**

Future satellite systems that operate simultaneously to a large number of widely-spread earth stations may make use of on-board processing to allocate additional resources on a dynamic basis to earth stations requiring additional link margins or capacity. Such a scheme is a shared-resource TDMA operation [Acampora, 1981, v Hugo and Wilde, 1994] in which a pool of additional capacity (reserve portions of the TDMA frame) can be assigned to users needing the extra resource. The allocation would be on a dynamic basis and could be under the control of a master control station on the Earth or, in more advanced versions, under the control of a processing payload on the satellite itself.

To estimate the additional capacity required in a shared-resource scheme, the probability of occurrence of joint outages at the earth stations is required. Studies of large-scale diversity [Barbaliscia *et al.*, 1988a, 1988b, 1989] indicate that the dynamic allocation of resources among a large group of earth stations could significantly reduce the outage probability due to rain at individual earth stations. However, the same studies show that an assumption of statistical independence between the various earth stations may lead to an underestimate of the outage probability of the individual earth station, due to the correlation of rainfall that still exists between earth stations at separations up to 800 km [Dintelmann *et al.*, 1993].

For a satellite system operating with  $N$  earth stations with a number  $M$  of extra common resources, two design elements can be identified:

- a) the probability of "over-request" of the on-board system and its resources; and
- b) the probability of an individual earth station "not being helped" and its hierarchy of priority, if any, among the  $N$  stations.

Both probabilities can be expressed by a weighted sum of the probabilities of joint fading events for the various combinations of the  $N$  stations [Barbaliscia *et al.*, 1989].

For a simple case of pairs of stations ( $N = 2$ ,  $M = 1$ ) an empirical approximation can be established for the probability of joint rain events, as a function of the distance  $d$  (km) and of the rain level in the range 0 to 6 mm/h as:

$$P_{ij} = A_1 e^{-\left(\frac{d}{D_1}\right)} + A_2 e^{-\left(\frac{d}{D_2}\right)^2} \quad (3.11)$$

with:

Case 1

$$A_1 = 33 H^{0.92}$$

$$D_1 = 592 - 22 H \quad \text{where } H = \text{daily rainfall (mm/day)}$$

$$A_2 = 0.2 \quad \text{for } H \leq 20 \text{ mm/day}$$

$$D_2 = 1400$$

Case 2

$$A_1 = 0.3 R^{0.6}$$

$$D_1 = 195 - 30 R \quad \text{where } R = \text{rainfall rate (mm/h)}$$

$$A_2 = 0.02 \quad \text{for } R \leq 6 \text{ mm/h}$$

$$D_2 = 500$$

The parameters in Case 1 should be used when the joint probability of the occurrence of a cumulative quantity of rain per day is required. Where the joint probability of a given rainfall intensity is required, the parameters given in Case 2 should be used. It should be noted that the rainfall intensity for Case 2, while shown in mm/h is, in fact, the average rainfall intensity over the joint probability period needed (for this case, one hour).

For the more general case of  $N$  stations and  $M$  resources, a model has been developed based on the assumption of log-normality for the joint rain distributions that shows good agreement with the experimental data. It should be noted that log-normality applies only to the fraction of time during which the rainfall rate exceeds zero simultaneously at all of the  $N$  earth stations.

**3.3.3 Other diversity schemes**

Without an ability to increase the margin (e.g., through the application of power control via additional transmit gain, transmit power, or increased resource allocation in the TDMA frame), there are basically three types of diversity schemes that can be used by satellite systems to overcome impairments at a given earth station: time diversity; frequency diversity; and site diversity. Site diversity has been discussed above but there is another technique that provides for a measure of path diversity and that is orbital diversity. A brief outline of orbital diversity and the other two diversity techniques is provided in the following.

### **3.3.3.1 Orbital diversity**

Orbital diversity [Capsoni and Matricciani, 1984] is different from site diversity in that only one earth station site is used. To achieve a measure of diversity, the earth station uses two antennas that can access different satellites simultaneously. Orbital diversity does not require the diversity interconnect link between sites as is required for site diversity, but to obtain significant decorrelation of concurrent attenuations along the two paths, the angle between the two paths at the earth station must be large.

However, if this angle is large, at least one, and possibly both, of the links will be at a relatively low elevation angle and therefore encounter a greater degree of impairments than encountered at higher elevations. In any case, the achievable diversity gain is fairly small, generally being at most about 2-3 dB in the 14/11 GHz bands.

### **3.3.3.2 Frequency diversity**

Path losses caused by particulates on the path increase as the frequency increases, particularly for rain. At 6/4 GHz, attenuation due to rain is negligible; at 14/11 GHz it can be significant in high rainfall rate regions of the world; at 30/20 GHz it is the dominant link impairment nearly everywhere. If it is possible to switch communications from a band to a lower-frequency band, significant increases in availability might be achieved [Mangulis, 1985].

This capability requires that both frequency bands (the higher, impaired one and the lower one to which the communications channels are to be switched) be simultaneously available at the earth station in question. Furthermore there must be spare capacity available in the lower frequency band whenever needed, implying that significant spare capacity must be provided if the link is a high-capacity channel, and that the complete network be under dynamic control. Both elements require significant investment. Should such dynamic network control features be in place and the additional capacity in the lower frequency band be available on-call, frequency diversity can undoubtedly provide large increases in availability.

### **3.3.3.3 Time diversity**

Severe rain events do not usually last long at a given location. This characteristic can be used in any communications link that does not require interaction between the caller and the receiver. A facsimile transmission fits this category: provided a FAX is successfully sent without any errors within, say, a two-hour period, the service can be said to be acceptable. The delay in sending the FAX can be considered a form of time diversity.

This feature could also be used with advantage to determine the capacity requirements of a given link for optimal economic performance. If a link is sized for the maximum anticipated capacity it will have excess capacity for most of the time. If some transmissions can be delayed and sent, for example, at off-peak times, the capacity requirements can be reduced. The time delay could therefore be used either at times of peak capacity (i.e., the equivalent of call-blocking) or when the earth station is undergoing a severe rain event.

Another form of time diversity is the application of data rate reduction to permit the available margin to be increased. The receipt of the information, in this case, is delayed due to a reduction in the transmission rate.

### 3.4 Characteristics of precipitation events

Characteristics of precipitation events are of importance in the design and implementation of fade mitigation techniques such as power control, diversity, coding, and resource sharing. In addition, they need to be considered in specifying the performance of digital networks employing satellite links. Fade duration or the time interval during which the signal attenuation exceeds a given threshold, intervals between fade episodes, intervals between fade events, and the rate of change of attenuation are the most important dynamic features relevant to satellite system modelling. Within a precipitation event the fade level varies considerably, crossing a given fade threshold several times over a relatively short time interval; precipitation events themselves are separated by a longer time span as illustrated in Figure 3.11 [Kumar, 1985; Vogel *et al.*, 1993]. A precipitation event starts when the fade level exceeds a given threshold and ends when the fade level falls below the threshold and is followed by a long gap during which the fade level is closer to the clear-air value. Within the event there may be several short duration peaks separated by several short gaps. The peaks are called fade episodes and the gaps are known as inter-episode gaps or interfade intervals. The relatively longer time interval between fade events is the inter-event interval.

Tropospheric scintillations often accompany precipitation events, and the above features need to be characterized both in the presence and absence of scintillations. Characteristics of scintillations are discussed in Chapter 6. Scintillations are relatively fast variations in the signal amplitude and these can be separated from slower variations produced by precipitation particles using a low-pass filter. Filter time constants of the order of 120 seconds appear to be adequate for the purpose [Karasawa and Matsudo, 1991]. Figure 3.12 shows an example of separating rain fading and scintillations using a 1 minute moving average filter; the data have been collected using a 11 GHz beacon signal at an elevation angle of 6.5°.

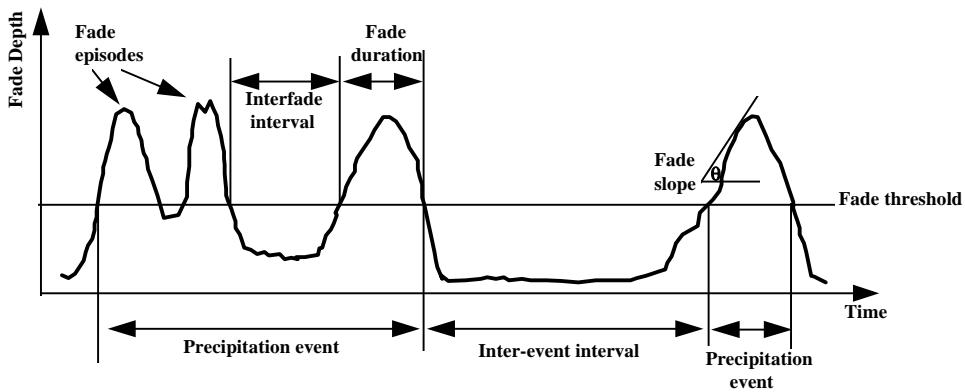
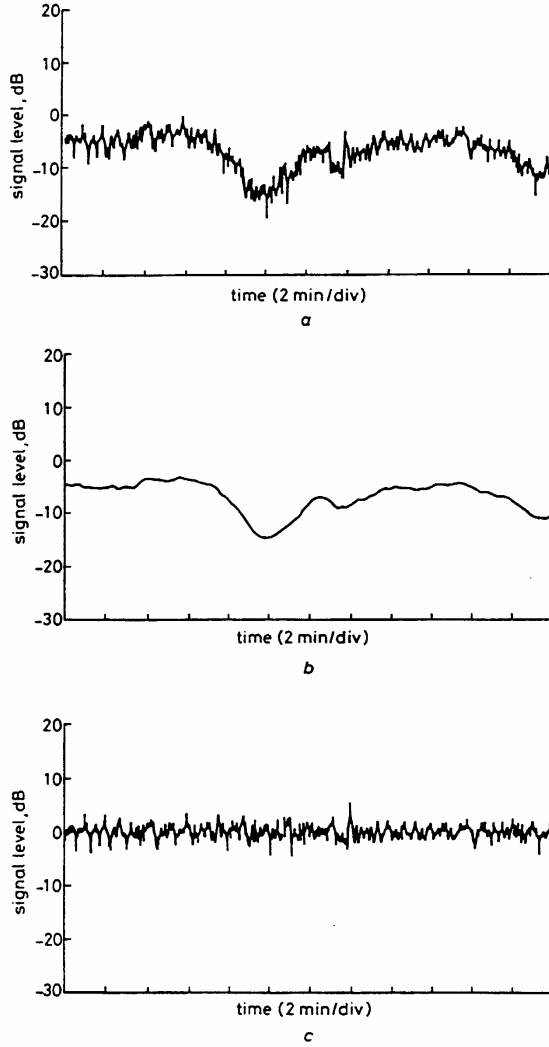


FIGURE 3.11

Features Commonly Used in Characterizing Precipitation Events



- (a) Original 11 GHz data at 6.5°
- (b) Data smoothed by moving average procedure at 1 minute intervals (11 GHz attenuation)
- (c) Difference between original and smoothed data (11 GHz scintillation)

FIGURE 3.12

**Separation of Scintillation and Rain Fading  
from [Allnutt, 1989] based on original work by Karasawa**

**3.4.1 Duration of individual fades**

In general, fade duration is a function of frequency, elevation angle, and the rain type. At a given fade threshold, the fade duration will increase with the increase of frequency and the decrease of the elevation angle. Experimental evidence shows that these dependencies approximately follow the rain attenuation dependence on frequency and elevation angle [Kumar, 1985; Allnutt, 1989]. Thus, the frequency dependence of fade duration at a fixed elevation angle is approximately given by:

$$\frac{\text{total no. of fades with } A > x \text{ dB at } f_1}{\text{total no. of fades with } A > x \text{ dB at } f_2} \approx \left(\frac{f_1}{f_2}\right)^2 \tag{3.12}$$

where  $A$  is the fade depth (dB) and  $x$  is the threshold (dB) at which the fades are counted and  $f$  is frequency. A more rigorous frequency scaling law may be found in Recommendation ITU-R P.618. The elevation angle dependence at a fixed frequency may be approximated by:

$$\frac{\text{total no. of fades } > A \text{ at } \theta_1}{\text{total no. of fades } > A \text{ at } \theta_2} \approx \frac{\sin \theta_2}{\sin \theta_1} \quad (3.13)$$

where  $\theta$  is the elevation angle.

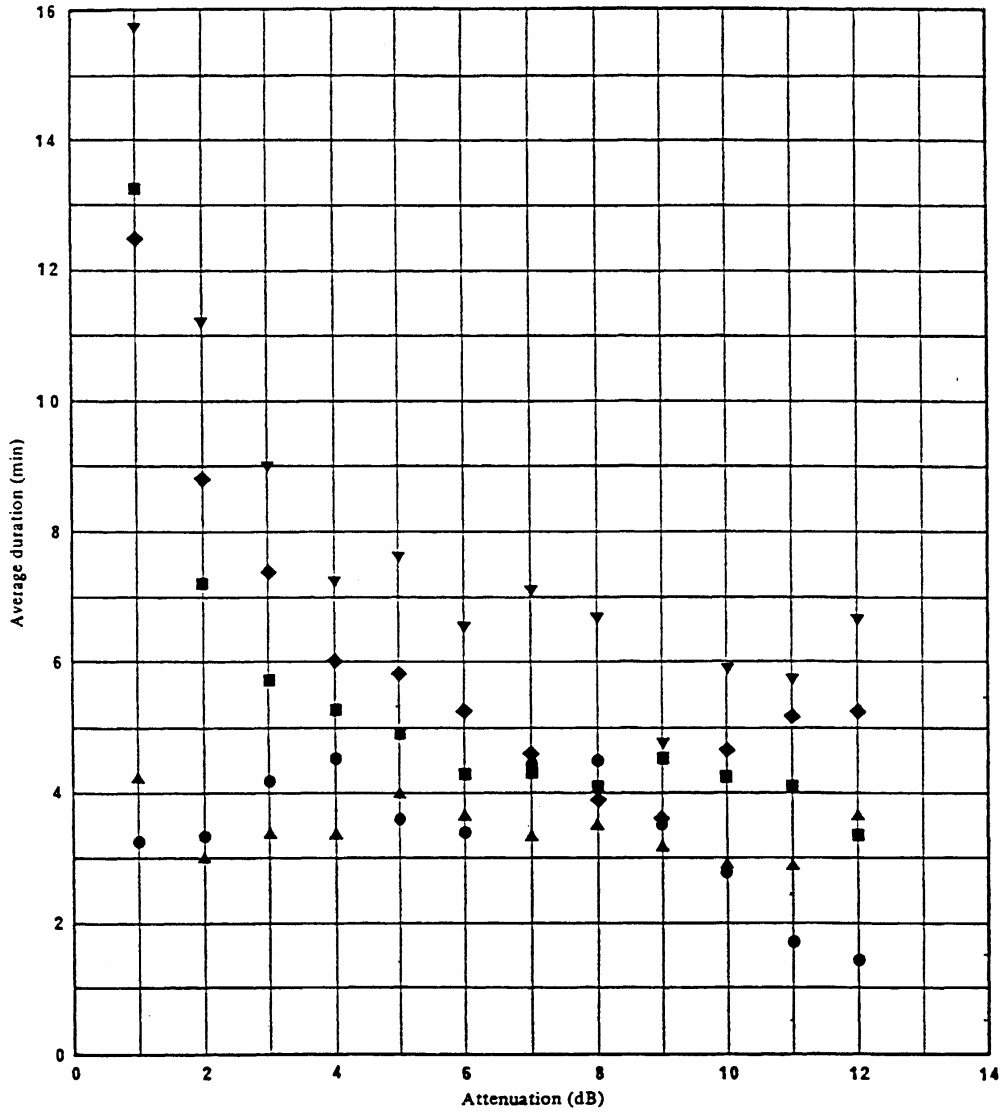
The elevation angle dependence shown in Equation (3.13) is expected to hold only for moderate to high elevations where fading is produced by individual rain cells. At low elevation angles more than one rain cell often contribute to the fading process, thus leading to a more complex elevation angle dependence.

The role of the rain type in influencing fade duration stems directly from the average dwell time of rain structures. Widespread rains tend to have longer dwell times compared to thunderstorm rains.

The average duration of fades exceeding a given threshold appears to be independent of the threshold level. This is due to the fact that the number of fades increase with the decrease of the fade threshold without any discernible relationship between the two parameters. The larger time percentage for which a lower fade threshold is exceeded is distributed among a larger number of fades, and the lower time percentage at a higher fade threshold is distributed among a smaller number of fades. An example of average fade duration is given in Figure 3.13 based on data from [Flavin, 1982].

An average fade duration of approximately 5 minutes for most fade thresholds is evidenced in Figure 3.13. This seems to be typical for most paths and climates with the exception of those regions that are subject to extremely severe and widespread events such as typhoons. The spread of fade duration around the average value increases with the decrease of the fade threshold. As an example, it is common to observe fades lasting more than an hour at a threshold of 3 dB at frequencies above about 14 GHz; on the other hand, a fade of 20 dB is less likely to last more than three or four times the average value. This is illustrated in the fade duration statistics shown in Figure 3.14 [Cox and Arnold, 1982]. The curves show the average number of fades per year with duration equal to or greater than the value on the abscissa and are drawn with and without a 1 dB hysteresis. Use of hysteresis essentially removes rapid signal fluctuations due to equipment effects, and to some degree tropospheric scintillations. The suppression of short-duration at 5 and 10 dB thresholds by hysteresis is evident. Presence of a large number of long-duration fades at the lower thresholds is also evident. Both these effects appear to disappear for fade depths of 20 dB or more.

The measured data indicate that the duration of fades exceeding a given threshold has a log-normal distribution of longer duration fades composed mainly of rain induced fades [Lin *et al.*, 1980; Dissanayake *et al.*, 1990]. Shorter duration fades, produced largely by tropospheric scintillations, can be represented by a power-law distribution [Paraboni and Riva, 1994]. Examples of fade duration distributions similar to those presented in Figure 3.14 can be found in the ITU-R SG 3 data bank (see Recommendation ITU-R P.311). In the absence of appropriate measured data, the empirical model described in Paraboni and Riva [1994] may be used to predict fade duration distributions.



- ▼ Darwin, Australia 14 GHz  $\theta = 60^\circ$  (Nov. 1977-May 1979)
- ◆ Darwin, Australia 11 GHz  $\theta = 60^\circ$  (Nov. 1977-May 1979)
- Innisfail, Australia 11 GHz  $\theta = 45^\circ$  (Oct. 1978-Apr. 1979)
- ▲ Melbourne, Australia 14 GHz  $\theta = 45^\circ$  (June 1980-June 1983)
- Melbourne, Australia 11 GHz  $\theta = 45^\circ$  (June 1980-June 1983)

FIGURE 3.13

Average Fade Duration as a Function of Fade Level [Flavin, 1982]

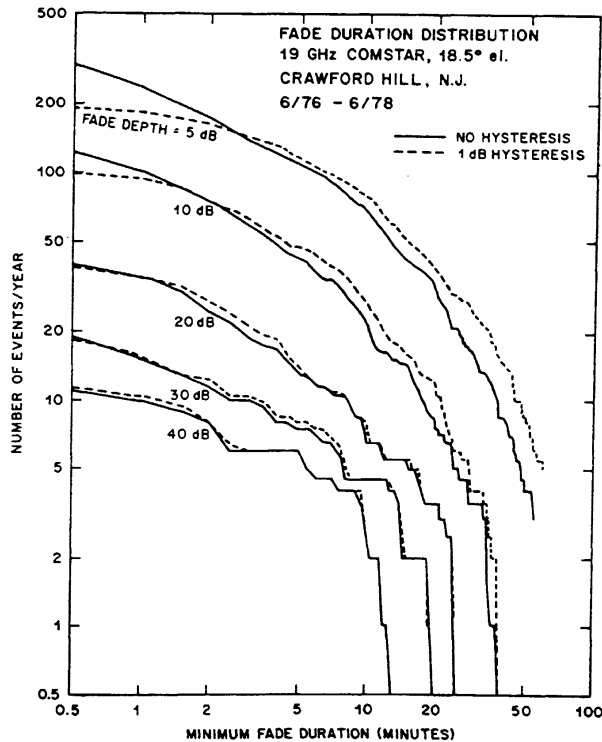


FIGURE 3.14

**Cumulative Distribution of Fade Duration [Cox and Arnold, 1982]**

**3.4.2 Interfade and inter-event intervals**

Information on interfade intervals is important in applications such as diversity switching in which excessive switch occurrences can have a detrimental effect on system performance. Inter-event intervals, which pertain to the return period of precipitation events, are of importance in network management and reallocation of resources on a larger scale.

In general, rain induced interfade intervals and inter-event intervals are log-normally distributed [Kumar, 1985; Vogel *et al.*, 1993]. Short duration interfade intervals resulting from tropospheric scintillations, however, are expected to follow a power-law form as found with the short-term fade duration.

Figure 3.15 gives an example where distributions for the interfade and inter-event intervals are shown separately [Vogel *et al.*, 1993]. The data were derived from a 11.2 GHz beacon experiment operating at an elevation angle of 5.8°. Data have been analyzed using a minimum clear-sky gap of 4.2 hours to separate inter-event gaps and inter-episode gaps or interfade intervals. The median inter-event gap between 20 dB fades was found to be 9.27 days. At a 20 dB threshold the central 90% of the interfade intervals were found between 80 seconds and 1.7 hours. Also shown in the figure are the average number of events per year and the number of fade episodes per event. It is seen that the number of fade episodes per event increases with the decrease of the fade threshold.

Figure 3.16 shows an example of a combined distribution of interfade and inter-event intervals from a 19 GHz satellite beacon experiment [Cox and Arnold, 1982]. The curves show the number of intervals per year with duration equal to or greater than the value on the abscissa and are drawn with and without a 1 dB hysteresis. As discussed earlier, hysteresis essentially removes rapid signal fluctuations due to equipment effects, and to some degree tropospheric scintillations. It can be seen that the slope of the distribution changes with the fade depth. Higher fade thresholds are

characterized by longer intervals mainly composed of inter-event intervals longer than 6 hours. Lower fade thresholds show a much larger variability with almost half of the intervals at the 5 dB threshold having a duration less than 1 hour.

Frequency and elevation angle scaling of inter-fade intervals may be attempted using the relationships discussed in the previous subsection under fade duration.

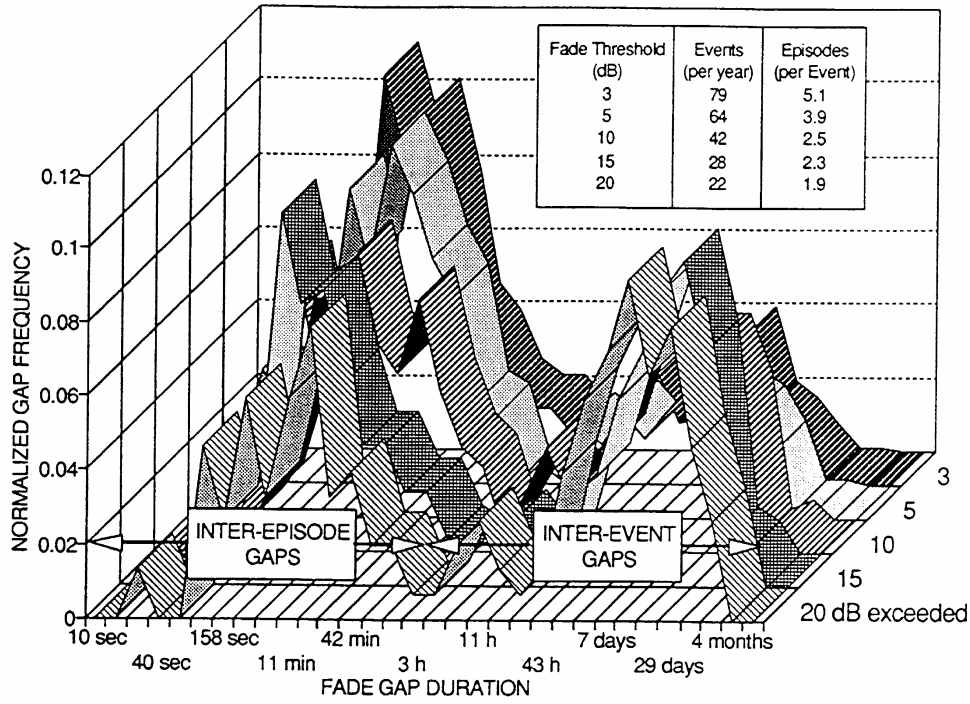


FIGURE 3.15

**Gap Duration Histograms for Rain Fades [Vogel *et al.*, 1993]**

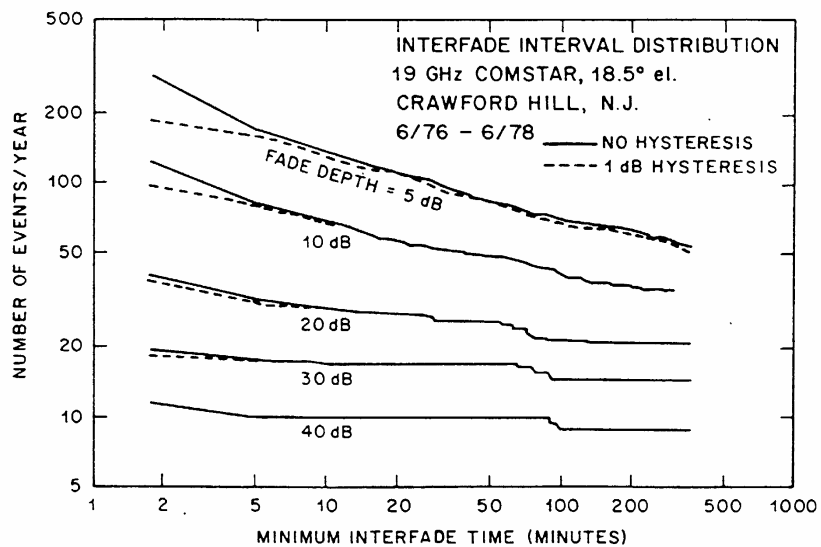


FIGURE 3.16

**Cumulative Distribution of Interfade Intervals [Cox and Arnold, 1982]**

### 3.4.3 Rates of change of attenuation

Rate of change of attenuation is normally estimated only for rain fades after removing most of the signal fluctuations arising from tropospheric scintillations. As found with the rain fade duration statistics, the distribution of the rate of change of attenuation appears to be log-normal with a median of about 0.1 dB/s. The rate of change of attenuation increases with the operating frequency. Distributions of the positive-going (fading) and negative-going (recovering) slopes are found to have similar distributions. However, there appears to be clear evidence that, as the fade rate increases, the difference between the fade slope and the recovery slope tends to increase with the fade slope always being greater. The physical explanation could be that the higher fading rates are associated with thunderstorms and that the leading edges of thunderstorms contain higher rainfall rates than the trailing edges.

Cumulative distributions of rate of change of attenuation or fade slopes derived from a beacon measurement experiment at a frequency of 30 GHz and an elevation angle of 26.8° are shown in Figure 3.17 as reported in [Baptista and Davies, 1994]. Distributions pertain to the absolute value of the slope without regard to the positive- or negative-going fades. Distributions for three fade ranges are shown in the figure. It can be seen that the probability of encountering higher rates of change of attenuation increases with increasing attenuation. Similar trends have been identified by other experimenters as well [Pratt *et al.*, 1993; also other experiments reported in Baptista and Davies, 1994]. Fade slopes at other frequencies may be estimated using the frequency scaling relationships found in Recommendation ITU-R P.618.

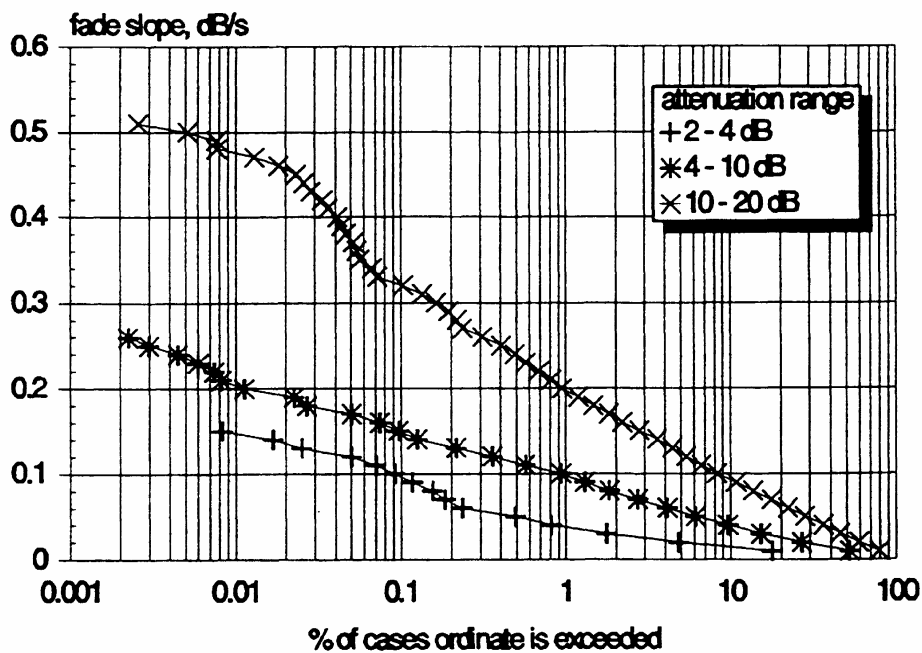


FIGURE 3.17

Cumulative Distribution of Fade Slopes at 30 GHz [Baptista and Davies, 1994]

### 3.4.4 Correlation of instantaneous values of attenuation at different frequencies

When comparing instantaneous attenuations measured simultaneously at different frequencies, it must be borne in mind that in most cases the combined effect of different attenuating mechanisms is observed. Hence, in order to be meaningful, the comparison should be restricted to one attenuating effect only. In the case of rain attenuation this would require a correction for the gaseous and cloud absorption components. However, if rain is the dominant attenuation component, the other effects become less important with increasing rain attenuation.

With its beacons at 12.5, 20 and 30 GHz, OLYMPUS allowed for a comparison of simultaneously-measured instantaneous attenuations. When plotting the attenuation  $A(f_1)$ , measured at beacon frequency  $f_1$ , versus the simultaneously-measured attenuation  $A(f_2)$ , at frequency  $f_2$ , a high degree of correlation is observed, although often a hysteresis-like pattern is found [Ortgies *et al.*, 1991]. This behaviour has an immediate bearing on frequency scaling of attenuation in uplink power control applications where it would be desirable to use the instantaneously-measured attenuation scaling ratio. The most prominent causes for the hysteresis effect are variations in the drop size distributions as well as in the path length through rain [Ortgies *et al.*, 1992]. This is plausible, since a particular attenuation level can result from the product of a low specific attenuation and a long propagation path, or a high specific attenuation and a short path length. In the first case, low intensity rain with small droplets is the cause for attenuation, while in the second, larger rain drops are involved. Large raindrops lead to a lower attenuation-scaling factor than small drops. Therefore, the observed change of instantaneous scaling factors reflects the development of a rain storm. Statistics of the instantaneous frequency scaling factor for 20/30 GHz were obtained for a period of 30 months and for one year at Darmstadt (Germany) and Virginia Tech (USA) respectively [Pratt *et al.*, 1993]. The steep increase of the scaling factor observed for low values of 20 GHz attenuation can be explained in terms of water vapour and cloud attenuation.

The variability in time of the attenuating processes also has an immediate bearing on the scaling of attenuation. Applications requiring a higher accuracy than can be achieved with a constant scaling factor would have to rely on monitoring an additional beacon signal whose frequency is close to that to which attenuation is to be scaled.

## 3.5 Sand and dust effects

### 3.5.1 General

The atmosphere contains a variety of solid particles in suspension. These particles range in size from aerosols (up to 50  $\mu\text{m}$ ) to coarse dust, sometimes known as sand (about 1 mm [Miller and Anthes, 1981]). The larger the size of the particles, the quicker they fall out of suspension. While aerosols can remain aloft for days, and sometimes years, coarse dust will rapidly descend to the ground once the impelling force, such as a violent wind storm, has subsided. In a like manner, aerosols can be carried high up into the stratosphere in even a slight updraft while the larger particles, such as coarse dust, generally remain within a few metres of the surface of the Earth.

Aerosols and small solid particles do not significantly affect the transmission of electromagnetic waves until the optical frequencies are approached and their extinction cross-section becomes appreciable. The effect of fine dust and coarse dust on radiowave transmissions can be noticeable at much lower frequencies, however, although the impact is often difficult to separate from the meteorological phenomena that often accompany the dust storms. In many cases, the strong winds that generate a dust storm may cause antenna depointing that will lead to a loss of signal strength which is difficult to distinguish from the attenuating effect of dust particles. In other cases, enhanced

humidity or even rain that might accompany a severe convective activity in an arid region might cause the dust particles to attenuate more strongly than would be the case in a dry atmosphere due to water up-take into the crystal structure of the particles themselves.

### 3.5.2 Categories of dust storms

An intensive investigation of the effects of sand and dust particles on 6/4 and 14/11 GHz signals on satellite-to-ground paths [McEwan *et al.*, 1985] made a clear distinction between dust and sand, which is summarized in Table 3.1 below. Note that sand particles are usually restricted to within 10 m of the surface of the Earth, and so their impact on satellite-to-ground links due to propagation effects is usually insignificant at elevation angles above 5°. The same investigation identified eight distinct dust storm types: Planetary Winds, Cyclogenetic, Frontal, Katabatic Winds, Haboob, Constriction, Dust Devils, and Diurnal Winds. The eight dust storm types were classified into a range of average wind speeds, maximum gusts, average storm widths, average storm lengths, and effective storm heights. Table 3.2 summarizes these data and Figure 3.18 shows the major desert regions of the world with the locations and directions of motion of the dust storms. In Figure 3.18, the areas shown in heavy black are the main source areas for dust; the shaded areas are the deserts of the Earth; regions shown within broken lines are regions at sea where haze may occur due to dust for >10 days in any season; the arrows indicate the general directions of the dust storms; “C” indicates areas affected by haboobs; and “D” indicates areas that are not classified as deserts but where dust storms can occur.

A haboob is a direct result of a thunderstorm, being generated by the strong, cold down-draught. For this reason, a haboob is sometimes known as a cold dust storm. The severe turbulence and gusting in a haboob lead to very high suspended dust densities. The high dust particle densities give rise to a significant reduction in (optical) visibility. For this reason, optical visibility has been used as a classification mechanism for dust storms.

The principal criterion applied to defining the occurrence of a dust storm is when the visibility drops below 1 km. Using this as the determining criterion, between 0.1 and 174 days per year of dust storm activity occur for the various regions of the world where such effects are observed. Table 3.2 also gives the typical visibilities and expected duration for the same eight dust storms classified earlier. Because optical extinction is a parameter that is relatively easy to measure, there have been attempts to model microwave attenuation in dust storms from visibility data.

TABLE 3.1

#### Salient distinctions between sand and dust particles

	Sand	Dust
Diameter limits	> 10 $\mu\text{m}$ , generally < 100 $\mu\text{m}$	< 10 $\mu\text{m}$
Usual maximum height above the ground	< 10 m	> 1,000 m
Silica content	> 80%	< 55%
Iron oxide content	~ 7%	20 - 30%
Water absorbed in air of 91% relative humidity	< 1%	6 - 9%

TABLE 3.2

**Eight Dust Storm Classifications, with Typical Wind Speeds, Structures, Visibility and Duration [McEwan *et al.*, 1985]**

Type of Storm	Average Wind Speed (m/s)	Max. Gust Speed (m/s)	Width (km)	Length (km)	Height (km)	Visibility Expected	Duration of Event
1) Planetary Winds	6 - 17	23	0.3 - 250	40 - 8 000	0.4 - 3	10 m - < 11 km	< 24 h - 2 weeks
2) Cyclogenetic	7 - 18	27 - 50+				0 - <1 000 m (0 - 50 m in severe storms)	6 - 24 h
a) Low Level Jet			500 - 1 000	500 - 2 000+	3 - 5		
b) Upper Level Jet			500 - 1 000	500 - 2 000+	3 - 5		
c) Surface Storm Circulation			50 - 150	50 - 150	0.4 - 0.8		
3) Frontal	9 - 17	38	500 - 1 000	50 - 2 000+	1 - 5	0 - <1 000 m (0 - 50 m in severe storms)	1 - 8 h
4) Katabatic Winds	12 - 21	36 - 50+	15 - 150	100 - 450	1 - 5	3 - <1 000 m	0.5 - 18 h
5) Haboob	11 - 21.5	41	3 - 75	3 - 300	0.5 - 12	200 - 400 m (0 - 50 m in severe storms)	0.5 - 6 h
6 Constriction	14	18	0.5 - 10	Length of the valley	Height of the valley	800 - 1 000 m (3 m in severe storms)	0.5 h
7) Dust Devils	5 - 10	15	0.01 - 0.5	Localized	0.5 - 3	< 1 000 m	0.1 - 0.5 h
8) Diurnal Wind Cycle	8 - 13	15	0.1 - 50	1 - 40	< 1	< 1 000 m (Near zero in severe storms)	< 1 h



FIGURE 3.18  
Sources and directions of major dust storms [McEwan *et al.*, 1985]

### 3.5.3 Propagation impairment prediction models for dust effects

An expression commonly used to relate the suspended dust mass  $\rho$  to the visibility  $V$  (in km) is due to Chepil and Woodruff [Chepil and Woodruff, 1957]:

$$\rho = \frac{56 \times 10^{-9}}{V^{1.25}} \quad \text{grams/cm}^3 \quad (3.14)$$

The visibility is that which exists 2 m above the ground.  $N$ , the number of dust particles per  $\text{m}^3$ , of radius  $a$  (in metres), can be related to the visibility  $V$  (in km) as follows [Flock, 1987]:

$$N = \frac{5.51 \times 10^{-4}}{Va^2} \quad (3.15)$$

The density of the particles decays with height and, in order to calculate the integrated effects along the slant path to a satellite, an effective path length needs to be determined in much the same way as for rain attenuation. One model that derives an effective path length [McEwan *et al.*, 1986] postulates a storm contained within a cylinder 10 km in diameter with the dust horizontally uniform, but decaying exponentially with height, inside the cylinder, and negligible outside. If  $k_r$  and  $k_i$  are the real and imaginary parts of the complex relative dielectric constant of the dust particles, respectively, the specific attenuation  $\alpha_p$  can be given by [Flock, 1987]:

$$\alpha_p = \frac{189a}{V\lambda} \left( \frac{3k_i}{(k_r + 2)^2 + k_i^2} \right) \text{ dB/km} \quad (3.16)$$

where  $\lambda$  is the wavelength in metres. The equations for  $N$  and  $\alpha_p$  assume that the dust particles have a uniform radius. Not only is this unlikely to be the case, but also the particles will have different orientations. This non-symmetry can significantly affect the depolarization effects of an ensemble of dust particles. Eccentricity measurements of dust particles [McEwan *et al.*, 1983; Ghobrial and Sharief, 1987] have given an average value of 0.71 to the ratio of the horizontal minor axis to the horizontal major axis, and the value of 0.57 [McEwan *et al.*, 1983] and 0.53 [Ghobrial and Sharief, 1987] to the ratio of the vertical minor axis to the vertical major axis. This eccentricity, plus the likely net positive alignment of the crystals by aerodynamic [McEwan *et al.*, 1983] and electrical forces [Ghobrial and Sharief, 1987], will lead to some cases where the depolarization effects are significant, particularly on low elevation angle paths.

### 3.5.4 Typical propagation impairment prediction results

Table 3.3 (from Figure 16 of [Abdulla *et al.*, 1986]) and Table 3.4 (from Figure 1 of [McEwan *et al.*, 1986]) give some typical results of attenuation and depolarization predictions. In Table 3.3, circular dust particles are assumed with a uniform distribution. Table 3.4 assumes the eccentricities noted earlier for the dust particles, and postulates that the particles are fully aligned with equiprobable azimuths. The humidity is 0% and the antenna height is 20 m.

TABLE 3.3

**Specific attenuation in dB/km for a visibility of 10 m at the given frequency**

Frequency:	1 GHz		3 GHz		10 GHz		30 GHz	
g H <sub>2</sub> O/g soil:	0.3%	10%	0.3%	10%	0.3%	10%	0.3%	10%
Spec. Atten:	0.001	0.004	0.003	0.02	0.01	0.07	0.03	0.6

TABLE 3.4

**Cross Polarization Discrimination at a frequency of 14 GHz**

Elevation Angle:	5°	10°	20°	30°
Visibility 10m:	22	25	31	36
Visibility 5m:	16	17	26	30
Visibility 2m:	10	14	20	24

From Table 3.3, if an effective path length of 3 km is assumed, it is not until Ka-Band frequencies are employed (30/20 GHz) that the attenuation becomes in any way significant. Even then, it is only in relatively humid air, with 10% water up-take, that the path attenuation approaches 2 dB. For depolarization, the values of cross-polarization discrimination (XPD) are relatively benign until the visibility becomes very small (2 m) and the elevation angle is low. However, if the air becomes humid and the dust particles absorb the moisture, the XPD values are worsened by about 5 dB. On

some paths (elevation angle below  $10^\circ$ ) and for some frequencies ( $>10$  GHz), a severe dust storm that contains a large proportion of moist particles could cause the XPD to fall below 12 dB, a value commonly used as the value below which the interference potential may cause difficulties. In general, however, for satellite-to-ground paths the radiowave impairments caused by sand and dust storms are significantly less of a problem than the mechanical difficulties they may cause, such as severe wind gusts and dust in the antenna feeds and ancillary equipment.

REFERENCES FOR CHAPTER 3

- ABDULLA, S.A.A., AL-RIZZO, H.M., and CYRIL, M.M. [1986] Particle-size distribution of Iraqi sand and dust storms and their influence on microwave communications systems, *IEEE Trans.*, AP-36, 114-126.
- ACAMPORA, A.S. [1981] Rain margin improvement using resource sharing in 12 GHz satellite downlink, *Bell System Tech. Journal*, Vol. 60, 167-192.
- ALLNUTT, J.E. [1977] Variation of attenuation and space diversity with elevation angle on 12 GHz satellite-to-ground paths, *Electron. Lett.*, Vol. 13, 346-347.
- ALLNUTT, J.E. [1978] Nature of space diversity in microwave communications via geostationary satellites: a review, *Proc. IEE*, Vol. 125, 369-376.
- ALLNUTT, J.E. [1989] *Satellite-to-Ground Radiowave Propagation*, Peter Peregrinus, IEE, London.
- ALLNUTT, J.E. [1993] INTELSAT propagation experiments: the focus and results of recent campaigns, *Proceedings of the IEEE*, Vol. 81, No. 6, 856-864.
- ALLNUTT, J.E. and SHUTIE, P.F. [1977] Slant-path attenuation and space-diversity results at 30 GHz using radiometer and satellite receivers, *Proceedings of ATS-6 Meeting*, ESTEC, Noordwijk, 6-7 Sept. 1977 (ESA SP-131).
- ALTMAN, F.J. and SICHAKE, W. [1956] Simplified diversity communications system for beyond-the-horizon links, *IRE Trans.*, Vol. CS-4, 50-55.
- BAPTISTA, J.P.V. and DAVIES, P.G., editors [1994] *Reference Book on Attenuation Measurement and Prediction: OPEX Second Workshop of the Olympus Propagation Experiments*, European Space Agency, ESA WPP-083.
- BARBALISCIA, F., BRUSSAARD, G., PARABONI, A. and RAVAIOLI, G. [1988a] Spatial statistical dependence of rainy events, *URSI-IEEE Symposium*, Syracuse, USA.
- BARBALISCIA, F. and PARABONI, A. [1982] Joint statistics of rain intensity in eight Italian locations for satellite communications networks, *Electron. Lett.*, Vol. 18, 118-119.
- BARBALISCIA, F., PARABONI, A. and RAVAIOLI, G. [1988b] Fading correlation study: Final Report - *ESA Contract No. 6825/86/NL/DG*, Fondazione Ugo Bordoni 1A1188, Italy.
- BARBALISCIA, F., PARABONI, A. and RAVAIOLI, G. [1989] Analysis and modelling of rain correlation over wide areas, *URSI Commission F Open Symposium*, La Londe Les Maures, France.
- BOITHIAS, L. [1989] Frequency scaling for rain attenuation. *Ann. des Télécomm.*, Vol. 44, 5-6, 186-198.
- BRUSSAARD, G. [1981] Prediction of attenuation due to rainfall on Earth-space links. *Radio Science*, Vol. 16, 5, 745-760.
- BRYANT, D.L. [1992] Low elevation angle 11 GHz beacon measurements at Goonhilly earth station, *BT Technology*, Vol. 10, No. 4, 68-75.

- CAPSONI, C. and MATRICCIANI, E. [1984] Performance of orbital diversity systems and comparisons with site diversity in Earth-space radio links affected by rain attenuation, *AIAA 10th. Communications Satellite Conference*, Orlando, Florida, USA, paper AIAA 84-0723, 565-570.
- CHEPIL, W.S., and WOODRUFF, N.P. [1957] Sedimentary characteristics of dust storms: 2. Visibility and dust concentration, *Am. J Science*, 255, 104-114.
- COX, D.C. and ARNOLD, H.W. [1982] Results from the 19- and 28-GHz COMSTAR Satellite Propagation Experiments at Crawford Hill, *Proc. IEEE*, Vol. 70, 458-488.
- CRANE, R.K. [1980] Prediction of attenuation by rain. *IEEE Trans. Comm.*, Vol. COM-28, 9, 1717-1733.
- DINTELMANN, F., ORTGIES, G., SZUPPA, S., and TROMMER, H. [1993] Fade duration and site diversity statistics to assess low-margin system performance at 30 GHz, XXIVth General Assembly of URSI, Kyoto.
- DISSANAYAKE, A.W., MCCARTHY, D.K., ALLNUTT, J.E., SHEPHERD, R. and ARBESSER-RASTBURG, B. [1990] 11.6 GHz Rain Attenuation Measurements in Peru, *Intl. Jnl. Satellite Comm.*, Vol. 8, 229-238.
- FEDI, F. [1979] Attenuation due to rain on a terrestrial path. *Alta Frequenza*, Vol. 66, 167-184.
- FEDI, F. [1980] Rain attenuation on Earth-satellite links: a prediction method based on point rainfall intensity. *Proc. URSI (Commission F) International Symposium on Effects of the lower atmosphere on radio propagation at frequencies above 1 GHz*, Lennoxville, Canada.
- FEDI, F. [1981a] Predicting of attenuation due to rainfall on terrestrial links. *Radio Science*, Vol. 16, 5, 731-743.
- FEDI, F. [1981b] A simple method for predicting rain attenuation statistics on terrestrial and Earth-space paths. *Fondazione Ugo Bordononi*, Report 1B1 081.
- FEDI, F. and PARABONI, A. [1986] A new prediction method for attenuation beyond 10 GHz based on a model of raincells characterized by exponential shape. statistics on terrestrial and Earth-space paths. *Proc. URSI -F*, Durham, USA
- FLAVIN, R.K. [1982] Rain attenuation considerations for satellite paths in Australia. *Australian Telecom. Research*, Vol. 16, 2, 11-24.
- FLOCK, W.L. [1987] *Propagation effects on satellite systems at frequencies below 10 GHz: A handbook for satellite system design*. NASA Reference Publication 1108(2), 2nd. Edn.
- FURGUSSON, A. and ROGERS, R.R. [1978] Joint statistics of rain attenuation on terrestrial and Earth-space propagation paths, *Radio Science*, Vol. 13, 471-479.
- GARCIA-LOPEZ, J.A., HERNANDO, J.M. and SELGA, J.M. [1989] Simple rain attenuation prediction method for satellite radio links. *IEEE Trans. on Antennas and Propagation*, Vol. 36, 3, 444-448.
- GHOBRIAL, S.I., and SHARIEF, S.M. [1987] 'Microwave attenuation and cross-polarization in dust storms', *IEEE Trans.*, Vol. AP-35, 418-425.

- GOLDHIRSH, J. [1976] Earth-space path attenuation statistics influenced by orientation of rain cells, *Proc. 17th. Conf. on Radar Meteorology*, Seattle, Washington, USA (American Meteorological Society), 85-90.
- GOLDHIRSH, J. and ROBISON, F.L. [1975] Attenuation and space diversity statistics calculated from radar reflectivity data of rain, *IEEE Trans.*, Vol. AP-23, 221-227.
- GRAY, D.A. [1973] Earth-space path diversity: dependence on baseline orientation, *IEEE G-AP Int. Symp.*, University of Colorado, Boulder, Colorado, USA, 366-369.
- GUTTEBURG, O. [1983] Measurements of atmospheric effects on satellite links at very low elevation angles, *AGARD EPP Symposium on Characteristics of the lower atmosphere influencing radiowave propagation*, Spatind, Norway, 5-1 to 5-19.
- HALL, J.E. and ALLNUTT, J.E. [1975] Results of site diversity tests applicable to 12 GHz satellite communications, *IEE Conf. Publ. 126*, 156-162.
- HARROLD, T.W. and AUSTIN, P.M. [1974] The structure of precipitation systems - a review, *J. Recherches Atmos.*, Vol. 8, 41-57.
- HODGE, D.B. [1973] The characteristics of millimeter wavelength satellite-to-ground space-diversity links, *IEE Conf. Publ. 98*, 28-32.
- HODGE, D.B. [1974] Path diversity for reception of satellite signals, *J. Recherches Atmos.*, Vol. 8, 443-449.
- HODGE, D.B. [1976] An empirical relationship for path diversity gain, *IEEE Trans.*, Vol. AP-24, 250-251.
- HODGE, D.B. [1978] Path diversity for Earth-space communications links, *Radio Science*, Vol. 13, 481-487.
- HODGE, D.B. [1982] An improved model of diversity gain on Earth-space paths, *Radio Science*, Vol. 17, 1393-1399.
- HODGE, D.B., THEOBALD, D.M. and TAYLOR, D.M. [1976] ATS-6 millimeter wavelength propagation experiment, *Report 3863-6*, ElectroScience Laboratory, Ohio State University, Columbus, Ohio, USA.
- HOGG, D.C. [1967] Path diversity in propagation of millimeter waves through rain, *IEEE Trans.*, Vol. AP-15, 410-415.
- HOGG, D.C. and CHU, T.S. [1975] The role of rain in satellite communications, *Proc. IEEE*, 1308-1331.
- IPPOLITO, L.J., KAUL, R.D. and WALLACE, R.G. [1983] Propagation effects handbook for satellite systems design, *NASA Ref. Publ. 1082(03)*, NASA, Washington, DC, USA.
- KALININ, A.I. [1976] Vliyanie dozhdya na oslableniye radiovoln na trassakh zemlya - ISZ. (Earth-to-space path attenuation due to rainfall). *Elektrosviaz*, 5.
- KARASAWA, Y. and MATSUDO, T. [1991] Characteristics of fading on low-elevation angle Earth-space paths with concurrent rain attenuation and scintillation, *IEEE Trans. on Antennas and Propagation*, Vol. AP-39, 5, 657-661.
- KUMAR, P.N. [1985] Fade Duration Statistics from COMSTAR 20/30 GHz Beacon Measurement Program, *COMSAT Tech. Review*, Vol. 15, 71-87.

- LEITÃO, M.J. and WATSON, P.A. [1986] Method for prediction of attenuation on Earth-space links based on radar measurements of the physical structure of rainfall. *IEE Proc.*, Vol. 133, 4, 429-440.
- LI, H.J., ZHANG, C.Q., LIAO, L. and ZHANG, G.F. [1987] An improved model for the prediction of rain attenuation statistics. *Proceedings of ICAP 1987*, 226-229.
- LIN, S.H. [1980] Rain attenuation on Earth satellite paths. Summary of 10-year experiments and studies. *BSTJ*, Vol. 59, 2, 183-228.
- LIN, S.H., BERGMANN, H.J. and PARSLEY, M.V. [1980] Rain attenuation on Earth-satellite paths - Summary of 10-year experiments and studies, *BSTJ*, Vol. 59, 183-228.
- MACKENZIE, E.C. and ALLNUTT, J.E. [1977] Effect of squall-line direction on space-diversity improvement obtainable with millimetre-wave satellite radio communications systems, *Electron. Lett.*, Vol. 13, 571-573.
- MAGGIORI, D. [1981] Computed transmission through rain in the 1-400 GHz frequency range for spherical and elliptical drops and any polarization, *Alta Frequenza*, Vol. L, 5, 262-273.
- MANABE, T., IHARA, T., AWAKA, J. and FURUHAMA, Y. [1987] The relationship of raindrop-size distribution to attenuation experienced at 50, 80, 140 and 240 GHz. *IEEE Trans. on Antennas and Propagation*, Vol. AP-35, 11, 1326-1330.
- MANGULIS, V. [1985] Protection of Ka-band satellite channels against rain fading by spare channels at a lower frequency, *Space Communications & Broadcasting*, Vol. 3, 151-158.
- MASS, J. [1979] Diversity and baseline orientations, *IEEE Trans.*, Vol. AP-27, 27-30.
- MCEWAN, N.J., and BASHIR, S.O. [1983] Microwave propagation in sand and dust storms: the theoretical basis for particle alignment. *International Conference on Antennas and Propagation*, ICAP 83, IEE Conf. Publ. 219, 40-44.
- MCEWAN, N.J, BASHIR, S.O., CONNOLLY, C., and EXCELL, D. [1985] *The effects of sand and dust particles on 6/4 and 14/11 GHz signals on satellite to Earth paths*. Final report to INTELSAT under contract INTEL-349, School of Electrical and Electronic Engineering, University of Bradford, Bradford, West Yorkshire, BD7 1DP, England.
- MCEWAN, N.J., CONNOLLY, C., EXCELL, D., and BASHIR, S.O. [1986] Attenuation, cross-polarization, and refraction in dust storms. Paper VIII-3, URSI Commission F Open Symposium, University of New Hampshire, Durham NH, USA.
- MILLER, A. and ANTHES, R.A. [1981] *Meteorology*, Charles E. Merrill Publishing Co., 4th. Edn.
- MIMIS, V. and SMALLEY, A. [1982] Low elevation angle site diversity satellite communications for the Canadian Arctic, *IEEE Int. Conf. on Communications*, 4A.4.1-4A.4.5.
- MISME, P. and WALDTEUFEL, P. [1980] Calcul des affaiblissements par les précipitations sur un trajet Terre-satellite. *Proc. URSI (Commission F) International Symposium on Effects of the lower atmosphere on radio propagation at frequencies above 1 GHz*, Lennoxville, Canada.
- MISME, P. and WALDTEUFEL, P. [1982] Affaiblissement calcules pour des liaison Terre-satellite en France, *Ann. Telecommun.*, Vol. 37, 325-333.

- MORITA, K. and HIGUTI, I. [1978] Statistical studies on rain attenuation and site diversity effect on Earth to satellite links in microwave and millimeter wavebands. *Trans. Inst. Electron. Comm. Engrs. Japan*, E61, 425-432.
- OLSEN, R.L., ROGERS, D.V. and HODGE, D.B. [1978] The  $aR^b$  relation in the calculation of rain attenuation. *IEEE Trans. on Antennas and Propagation*, 26, 2, 318-329.
- ORTGIES *et al.* [1992] *Proceedings of the NAPEX VI and ACTS miniworkshop*, 142-154.
- ORTGIES, G., DINTELMANN, F., and RÜCKER, F., [1991] Aspects of attenuation frequency scaling, *North American Radio Science Meeting and International IEEE/AP Symposium*, London, Canada.
- OTSU, Y., KOBAYASHI, T., SHINOZUKO, T., IHARA, T. and AOYAMA, S. [1978] Measurement of rain attenuation at 35 GHz along the slant paths over two sites with a height difference of 3 km, *J. Radio Research Labs. (Japan)*, Vol. 25, 1-21.
- PARABONI, A. and RIVA, C. [1994] A New Method for the Prediction of Fade Duration Statistics in Satellite Links Above 10 GHz, *Intl. Jnl. Satellite Comm.*, Vol. 12, 387-394.
- PRATT, T, STUTZMAN, W.L., SAFAAI-JAZI, A., REMAKLUS, P.W., LASTER, J., NELSON, B. and AJAZ, H. [1993] Fade duration statistics from the Virginia Tech propagation experiment using the Olympus satellite 12, 20 and 30 GHz beacons. *Proceedings of OPEX XX*, 224-256, Darmstadt, Germany.
- ROGERS, D.V. [1981] Diversity and single-site radiometric measurements of 12 GHz rain attenuation in different climates, *IEE Conf. Publ. 195*, 118-123.
- ROGERS, D.V. and ALLNUTT, J.E. [1984] Evaluation of a site diversity model for satellite communications systems, *IEEE Proc. F*, Vol. 131, 501-506.
- ROGERS, R.R. [1976] Statistical rainstorm models: their theoretical and physical foundations, *IEEE Trans.*, Vol. AP-24, 547-566.
- RUCKER, F. [1980] Simultaneous propagation measurements in the 12 GHz band on the SIRIO and OTS satellite links, *URSI Commission F Open Symposium*, Lennoxville, PQ, Canada, 4.1.1-4.2.5.
- RUE, O. [1985] Influence of the atmosphere on Earth-to-satellite links at frequencies above 10 GHz, *TELE*, Vol. 2, (English Edition, Sweden).
- RUE, O. [1988] The statistical dependence of rain height on rain rate, and its use in rain attenuation prediction. *Swedish Telecom Radio Report R1 01/88*.
- STRICKLAND, J.I. [1977] Radiometric measurement of site diversity improvement at two Canadian locations, *URSI Commission F Open Symposium*, La Baule, France (late paper).
- SZUPPA, S., HEYER, G., and TROMMER, H. [1993] Vergleich einjähriger 30-GHz-Radiometermessungen mit gleichzeitigen Regenintensitätsmessungen für den Großraum Berlin, *Kleinheubacher Berichte* 36, 701-705.
- TOWNER, G.C., BOSTIAN, C.W., STUTZMAN, W.L. and PRATT, T. [1984] Instantaneous diversity gain in 10-30 GHz satellite systems, *IEEE Trans.*, Vol. AP-32, 206-208.

- TOWNER, G.C., MARSHALL, R.E., STUTZMAN, W.L., BOSTIAN, C.W., PRATT, T., MANUS, E.A. and WILEY, P.H. [1982] Initial results from the VPI&SU SIRIO diversity experiment, *Radio Science*, Vol. 17, 1489-1494.
- V HUGO, D., and WILDE, A. [1994] An adaptive resource sharing strategy for TDMA, *International Journal of Satellite Communications*, Vol. 12, 249-256.
- VOGEL, W.J., TORRENCE, G.W. and ALLNUTT, J.E. [1993] Rain Fades on Low Elevation Angle Earth-Satellite Paths: Comparative Assessment of the Austin, Texas, 11.2 GHz Experiment, *Proc. IEEE*, Vol. 81, 885-896.
- WALLACE, R.G. and CARR, J.R. [1982] Site diversity system operation study - Final Report, *Tech. Report 2130*, ORI Inc., Silver Spring, Maryland, USA.
- WARREN, S.G. *et al.* [1986] Global distribution of total cloud cover and cloud type amounts over land, National Center for Atmospheric Research (NCAR) Technical Notes, *NCAR/TN-273*, October.
- WILSON, R.W. and MAMMEL, W.L. [1973] Results from a three-radiometer path-diversity experiment, *IEE Conf. Publ.* 98, 23-27.
- WITTERNIGG, N., RANDEU, W.L., RIEDLER, W. and KUBISTA, E. [1987] 3-years analysis report (1980-1983), Final Report of INTELSAT contract IS-900: 12 GHz quadruple-site radiometer diversity experiment, Institut für Angewandte Systemtechnik in der Forschungsgesellschaft, Inffeldgasse 12, A-8010 Graz, Austria.
- WITTERNIGG, N., RANDEU, W.L., RIEDLER, W., KUBISTA, E., ARBESSER-RASTBURG, B. and ALLNUTT, J.E. [1993] Quadruple site diversity in Austria using 12 GHz radiometers, *IEE Proceedings-H*.
- YAMADA, M., KARASAWA, Y., YASUNAGA, M. and ARBESSER-RASTBURG, B. [1987] An improved prediction method for rain attenuation in satellite communications operating at 10-20 GHz. *Radio Science*, Vol. 22, 1053-1062.
- ZAKHARYAN, M.V., KORNILOV, L.N. and POZHIDAEV, V.N. [1989] Izmereniya raspredelenii dozhdevykh kapel po razmeram i otsenka koefitsientov oslableniya radiovoln. (Measurement of raindrop size distributions and evaluation of attenuation coefficients). *Radiotekhnika i elektronika*, 8.

## CHAPTER 4

### SKY NOISE TEMPERATURE CONTRIBUTIONS

The radio noise emitted by all matter, while used as a source of information in radioastronomy and remote sensing, may be a limiting factor in communication services. Sources of radio noise of interest on Earth-space paths are the atmosphere, clouds, rain, extraterrestrial sources, and noise from the surface of the Earth. Prediction methods are given in Recommendation ITU-R P.372. Fundamental information about radio noise and galactic sources is given in [Kraus, 1966].

#### 4.1 Atmospheric noise temperature effects on Earth-space paths

The noise temperature of a satellite-based antenna is dominated by the high temperature emitted by the Earth, which fills, or mostly fills, the main beam of the antenna. Additional noise from precipitation or other variables is insignificant in this case [Allnutt, 1989]. For a global beam, the noise temperature is dependent both on frequency and on the position of the satellite with relation to the major land masses of the Earth. Figure 9 of Recommendation ITU-R P.372 shows this dependence.

The ground-based antenna, however, observes the relatively cool sky, and therefore the presence of clouds and rain can significantly raise the noise temperature of the antenna. In general, the temperature seen by an antenna is given by:

$$T_s = T_m(1 - 10^{-A/10}) + T_g \times 10^{-A/10} \quad \text{K} \quad (4.1)$$

where  $T_s$  is the sky-noise temperature as seen by the antenna,  $T_m$  is the effective temperature of the attenuating medium (atmosphere, clouds, rain),  $A$  is the total attenuation due to the medium, and  $T_g$  is the temperature of any extraterrestrial radio sources, plus background galactic noise (about 3K above 3 GHz). (The derivation of this equation is found in §§ 3-15 and 3-16 of [Kraus, 1966]). In most cases for practical satellite systems, the extraterrestrial noise term can be ignored (unless the Sun or moon is in the antenna beam) and the equation reduces to that given by Equation (52) in Recommendation ITU-R P.618.

The effect of rain on a satellite downlink is not just the attenuation, but the decrease in  $C/N$  due to the higher noise temperature seen in raining conditions compared to clear sky conditions. In some cases, the noise temperature increase can have more effect on the link than the attenuation itself [Pratt and Bostian, 1986].

#### 4.2 Galactic and other extraterrestrial noise sources

Noise from extraterrestrial sources, particularly the Sun, the Moon, and the galactic background, is well understood and the effect on the total noise temperature of a system can be calculated from the method in § 6 of Recommendation ITU-R P.372. The brightness temperature of the Sun decreases with increasing frequency, from about  $10^6$  at 30 MHz to  $10^4$  at 10 GHz under quiet conditions. At 20 GHz, an antenna of 2 m diameter (beamwidth about  $0.5^\circ$ ) would have an increase in noise temperature of about 8 100 K with a quiet Sun [Ippolito, 1989]. The Sun and moon each subtend an angle of about  $0.5^\circ$ , so that if the antenna beam is significantly larger than that, the effect of the Sun or moon is averaged with a larger portion of relative cool sky.

### 4.3 Noise from the surface of the Earth and man-made sources

Fixed earth station antennas for satellites in a geostationary orbit are typically designed and sited so that the main lobe does not intersect the local terrain or obstructions such as mountains or large buildings. Sidelobes are also minimized to reduce the effect of the Earth's temperature on the system performance. However, in land mobile-satellite systems, the antenna beam may pass through vegetation, or be obstructed by buildings or terrain. Measurements [Estabrook *et al.*, 1990] suggest that the impact of the additional noise is greatest when the antenna has a low internal noise temperature, that is, for a less directive antenna. Although these obstructions will raise the noise temperature seen by the antenna, they will also cause shadowing or multipath effects which are likely to be more significant in the total link performance; see Chapter 8.

Man-made noise is the dominant effect at VHF and UHF frequencies for all but the quietest rural areas. Unlike other noise effects, there is a polarization dependence in that the vertical component is higher than the horizontal [Hall, 1979]. In general, the median level of noise decreases linearly with  $\log(f)$ . There are significant variations with location and time, and little data are available to develop models to predict levels.

### 4.4 Example problem

On a 20 GHz downlink, the attenuation exceeded for 0.01% of the time is 7 dB. If the temperature of the rain is 260 K, and the galactic noise is ignored, the sky-noise temperature as seen by the antenna is, from Equation (4.1):

$$T_s = 260(1 - 10^{-7/10}) = 208 \text{ K}$$

If the receiver system noise temperature  $T_r$  in clear air is 250K, the increase in noise temperature is

$$10\log\left(\frac{T_s + T_r}{T_r}\right) = 10\log\left(\frac{208 + 250}{250}\right) = 2.6 \text{ dB}$$

so the system margin must allow for both the attenuation and the increase in noise: 9.6 dB.

REFERENCES FOR CHAPTER 4

- ALLNUTT, J.E. [1989] *Satellite-to-ground radiowave propagation*, Peter Peregrinus Press, IEE, London.
- ESTABROOK, P., OLIVER, G., JAMNEJAD, V., HUANG, J. and THOMAS, B. [1990] The impact of external noise sources on antenna noise temperature and the characterization of the antennas used in the joint MSAT-X/AUSSAT experiment, *MSAT-X Quarterly*, No. 22, JPL 410-13-22.
- HALL, M.P.M. [1979] *Effects of the Troposphere on Radio Communication*, Peter Peregrinus Press, IEE, London.
- IPPOLITO, L.J [1989] Propagation effects handbook for satellite systems design, *NASA Ref. Publ. 1082(04)*, NASA, Washington, DC, USA.
- KRAUS, J.D. [1966] *Radio Astronomy*, McGraw-Hill Book Co., New York, NY, USA.
- PRATT, T. and BOSTIAN, C.W. [1986] *Satellite Communications*, John Wiley and Sons, New York, USA.

## CHAPTER 5

### PATH DEPOLARIZATION

#### 5.1 Introduction

Dual orthogonally-polarized signals are used in some satellite communication systems to increase channel capacity without increasing the bandwidth requirements. This technique is known as “frequency re-use”. However, interference between the channels due to wave depolarization on the propagation path can limit the ideally achievable system performance.

Depolarization alters the polarization properties of the incident wave. Linear and circular polarizations are transformed into elliptical polarization, and the polarization axes themselves may be rotated [Chu, 1971; DiFonzo *et al.*, 1976].

The radiometeorological aspects of depolarization are discussed in Chapter 3 of the ITU-R Handbook on Radiometeorology. Excellent treatments of the system aspects of depolarization are also available (e.g., [Allnutt, 1989]).

##### 5.1.1 Physical causes of depolarization

Depolarization (cross-polarization) may occur when waves propagate through media that are anisotropic (asymmetrical) with respect to the incident polarization. Depolarization in the form of Faraday rotation of the plane of linear polarization occurs in the ionosphere because the ionosphere is birefringent in the presence of the Earth's magnetic field. The resulting impairments are typically circumvented by using circular polarization at those frequencies (less than about 10 GHz) for which the effect can be significant. Ionospheric propagation effects are discussed in detail in Chapter 7.

Depolarization in precipitation is caused by differential attenuation and phase shifts that are induced between orthogonal components of an incident wave by anisotropic hydrometeors. Orthogonally-polarized waves propagating in a medium that causes only differential phase shift are depolarized, but maintain orthogonality; however, if the medium also induces differential attenuation, the waves are deorthogonalized as well [DiFonzo *et al.*, 1976].

##### 5.1.2 Systems importance of depolarization

The importance of depolarization for a telecommunication system depends on several factors:

- signal frequency,  $f$ ;
- path geometry (e.g., elevation angle  $\theta$  and tilt angle  $\tau$  of the received polarization);
- local climatic factors (e.g., severity of the rain climate); and
- sensitivity to cross-polar interference (e.g., whether the system employs frequency reuse).

In systems operating in only one polarization state, depolarization causes a small apparent increase in the path attenuation. For systems using dual-orthogonal polarizations to increase channel capacity, however, the wanted signal received in either channel will sometimes be contaminated by interference from a cross-polarized component. Similar interference may occur for nearly-colocated satellites that employ orthogonal polarizations to increase inter-system isolation.

Occasionally, channel isolation may degrade sufficiently to impair performance, and must be accounted for in the design of frequency re-use systems. Depolarization is often the most significant path impairment for 6/4 GHz satellite systems [Allnutt, 1984], and can be the limiting performance factor for some 14/11 GHz satellite paths, especially at lower path elevation angles in moderate rain

climates [Rogers and Allnutt, 1986]. (The latter case is illustrated in the example calculations in § 5.6.) For frequencies of 20 GHz and above, performance is usually limited by path fading, at least for fade margins up to 10 - 15 dB and a minimum operational XPD margin of 15 dB.

Digital and adaptive-impairment mitigation techniques tend to benefit system performance in a frequency re-use environment. An exception is up-link power control, for which large increases in transmit power may generate substantial interference to adjacent links [McEwan and Leitao, 1982].

### 5.1.3 Cross-polarization isolation and discrimination

The polarization quantity of interest for frequency re-use telecommunication systems is the cross-polar isolation (XPI), defined as the decibel ratio of the (desired) co-polar power received in a channel to the (undesired) cross-polar power received in that same channel. In practice, XPI is difficult to measure because the cross-polarized component cannot be distinguished from noise in the co-polar channel. The quantity usually measured in experiments is the cross-polar discrimination (XPD), defined as the ratio of the co-polarized power received in one channel to the cross-polarized power detected in the orthogonal channel (both arising from the same transmitted signal).

Theory predicts that XPD and XPI are equivalent for most practical situations, and slant-path measurements with switched polarizations [Cox and Arnold, 1984] have confirmed that conclusion. The subsequent discussion is thus mainly in terms of the measured quantity, XPD.

### 5.1.4 Polarization states

Any electromagnetic wave is characterized by a polarization state, specified in terms of the electric field vector. In the general case, as the wave progresses in time the tip of the electric vector traces an ellipse in a plane perpendicular to the propagation direction. A representative polarization ellipse is displayed in Figure 5.1.

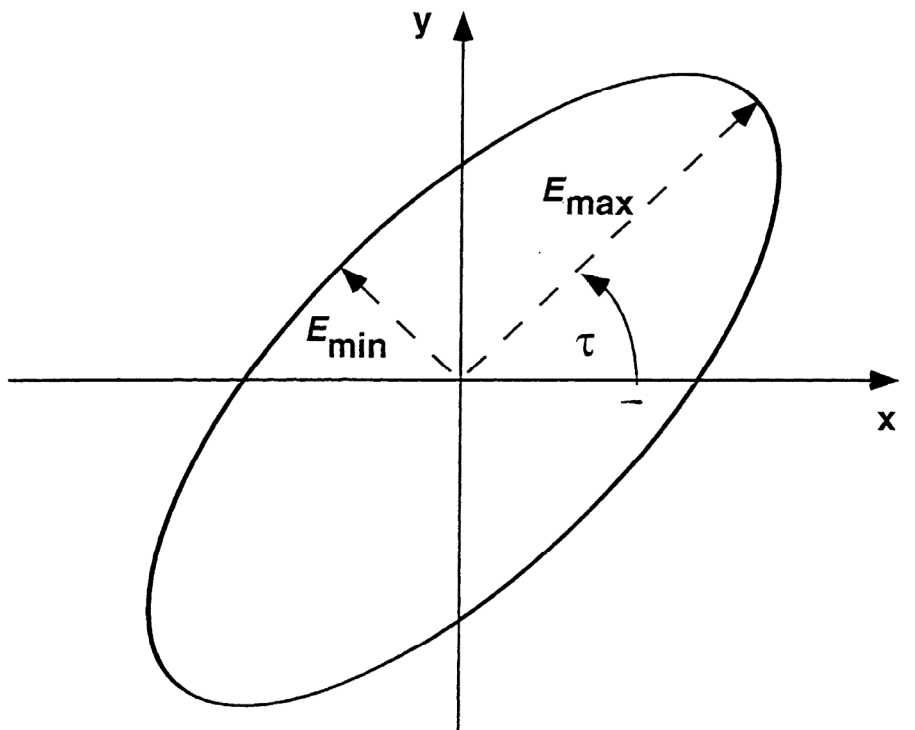


FIGURE 5.1

**Polarization ellipse of representative elliptically-polarized radio wave**

The polarization state of a wave is completely specified by its polarization ellipse (i.e., the amplitudes of the semimajor axis,  $E_{max}$ , and the semiminor axis,  $E_{min}$ ) and the sense of rotation of the vector (defined as right-hand for clockwise rotation as the wave propagates away from the observer, and left-hand for counter-clockwise rotation). As shown in Figure 5.1, the polarization ellipse may be tilted at an angle  $\tau$  with respect to a particular coordinate frame (e.g., as defined by the local horizontal and vertical at an earth terminal). In fact, the wave from a satellite as observed by an earth station is almost always tilted with respect to the local horizontal at the ground [see Equation (5.8)].

There are two particularly important cases of the polarization state:

- if  $E_{max}$  and  $E_{min}$  are equal in magnitude, the polarization state is said to be *circular*, (right-hand or left-hand circular, depending on the sense of rotation); and
- if  $E_{max}$  is nonzero and  $E_{min}$  is zero, the electric vector maintains a constant orientation defined by  $E_{max}$ , and the polarization state is said to be *linear*.

Pure polarization states are difficult to generate with actual antennas, and truly circular and linear polarizations are seldom attained in practice. A useful measure of the polarization purity is the voltage axial ratio,  $ar$ , defined by

$$ar = \left| \frac{E_{max}}{E_{min}} \right| \quad (5.1a)$$

or, in decibels,

$$AR = 20 \log \left| \frac{E_{max}}{E_{min}} \right| \quad \text{dB} \quad (5.1b)$$

In practice, waves with axial ratios less than about 1.4 (i.e., 3 dB) typically are considered to be “circular” polarization while those with axial ratios greater than about 10 (i.e., 20 dB) are classed as “linear” polarization.

### 5.1.5 Polarization orthogonality and mismatch

Successful operation in frequency re-use environments requires that coupling (cross talk) between the two polarizations be limited to a some minimum level for a specified percentage of the time. Equivalently, the polarization isolation between the two signals must be greater than some minimum threshold as prescribed by performance standards. The isolation between two polarization states is proportional to the degree of orthogonality between those states, while the coupling between an antenna and an incident wave is proportional to how nearly identical are the polarization states. Any corresponding reduction in coupling is called polarization mismatch.

It can be shown theoretically [Beckmann, 1968] that two polarizations are orthogonal when their polarization ellipses have the same axial ratio, their major axes are mutually perpendicular, and the senses of rotation are opposite. Ideal conditions are seldom achieved in actual systems, but this definition permits the analysis of coupling of a wave with an antenna, or of cross talk between dual-polarized signals in a frequency re-use system.

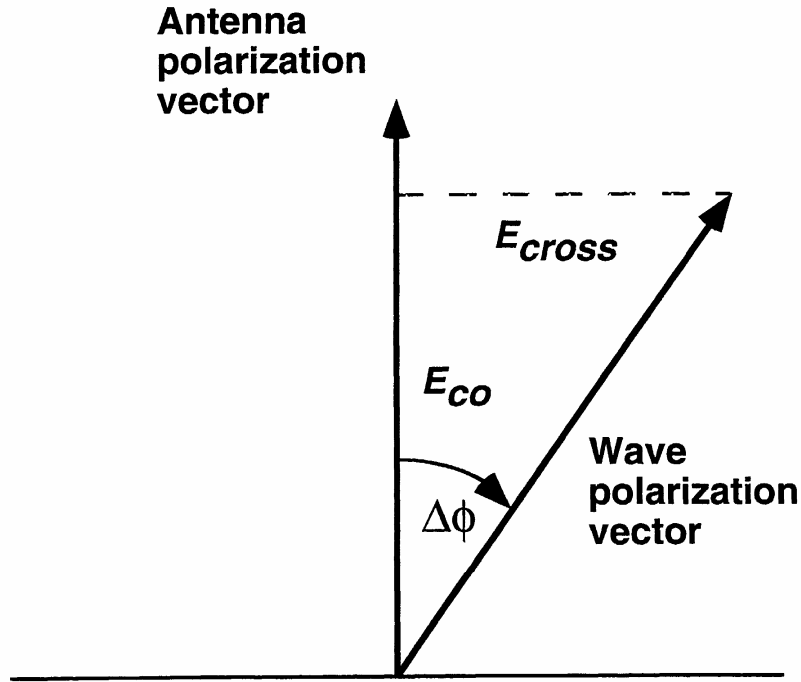


FIGURE 5.2

**Relation between linearly-polarized antenna and linearly-polarized wave rotated by angle with respect to antenna polarization**

For example, consider the linearly-polarized signal radiated by an elemental dipole. To detect this signal, an antenna characterized by the same (linear) polarization state is normally used. Suppose, however, that the wave polarization has been rotated by the propagation medium through an angle  $\Delta\phi$  with respect to the antenna polarization, as shown in Figure 5.2. In this case the (voltage) ratio of the polarization components of the wave with respect to the antenna polarization is simply

$$\left| \frac{E_{cross}}{E_{co}} \right| = \tan(\Delta\phi) \quad (5.2a)$$

with  $\Delta\phi$  the angle between the polarization vectors of the incident wave and the receive antenna. The square of the voltage ratio yields the power ratio, known as the cross-polarization ratio (*cpr*):

$$cpr = \left| \frac{E_{cross}}{E_{co}} \right|^2 = \tan^2(\Delta\phi) \quad (5.2b)$$

which is written in decibel units as

$$CPR = 20 \log(\tan \Delta\phi) \quad \text{dB} \quad (5.2c)$$

The CPR quantifies the cross talk generated at an antenna when the polarization axes of the antenna and the incident wave are misaligned by an angle  $\Delta\phi$ .

The cross-polarization ratio CPR is the inverse of cross-polarization isolation, XPI, as defined in § 5.1.3. This correspondence is applied in § 5.3.1 to specify the degradation in signal isolation caused by wave-antenna polarization mismatch when a linearly-polarized wave is rotated by the ionosphere (Faraday rotation).

## 5.2 Relation between depolarization and attenuation

Methods exist to calculate the scattering parameters of representative precipitation particles [Oguchi, 1983], which can be used as inputs to models that relate depolarization and attenuation on a propagation path, at least for the rain medium [Nowland *et al.*, 1977]. Such models have proven to be very useful for the prediction of system impairments. Although they are unable to account directly for other depolarization effects such as those caused by weakly-attenuating ice crystals, such effects can generally be incorporated in an approximate fashion by an empirical correction factor.

Path attenuation depends on the bulk loss of the propagation medium, while depolarization depends primarily on the bulk asymmetry of the medium [Rogers, 1985]. Instantaneous correlation between XPD and attenuation on a path is therefore often poor [Ippolito, 1981], but experiments verify that correlation is good on a statistical basis, at least for that portion of the distribution that is dominated by attenuating precipitation (rain). With a suitable model, it is thus possible to estimate XPD statistics from measured or predicted rain attenuation statistics.

The general form for semi-empirical expressions relating XPD (dB) to the co-polarized attenuation,  $A_p$  (dB), exceeded for  $p$  percent of the time on the same path is [Nowland *et al.*, 1977]

$$XPD = U - V \log (A_p) \quad \text{dB} \quad (5.3)$$

Various expressions of this type have been proposed [Olsen and Nowland, 1978; Dissanayake *et al.*, 1980; Chu, 1982; Stutzman and Runyon, 1984; Fukuchi *et al.*, 1984] for telecommunication system applications. The method of Recommendation ITU-R P.618 follows this same formalism.

### 5.2.1 Computation of long-term XPD statistics

The recommended XPD model, found in § 4.1 of Recommendation ITU-R P.618, is considered valid for frequencies,  $f$ , in the range  $8 \text{ GHz} \leq f \leq 35 \text{ GHz}$ , and path elevation angles  $\theta \leq 60^\circ$ . (Note, however, that the attenuation prediction procedure of Recommendation ITU-R P.618 is only recommended for frequencies up to 30 GHz.) An example XPD calculation with the method can be found in § 5.6.

The ITU-R prediction method has been developed from the general form of Equation (5.3) above. Additional terms have been derived to account explicitly for the dependence of XPD on frequency, path elevation angle, wave polarization state, and ice-crystal depolarization.

#### 5.2.1.1 Ice depolarization

Depolarizing ice crystals frequently exist above the rain region in thunderstorms, and sometimes in clouds unaccompanied by rain. The ITU-R prediction method incorporates an empirical correction to estimate the statistical XPD component generated by ice particles.

By combining the expressions for rain and ice depolarization from Recommendation ITU-R P.618, an equivalent expression for the net path depolarization may be written as

$$XPD_p = XPD_{rain} [0.85 - 0.05 \log p] \quad \text{dB} \quad (5.4)$$

where the term in brackets accounts for the effects of ice depolarization. Equation (5.4) demonstrates that in the model, the ice contribution to the net path XPD decreases as the time percentage decreases.

For time percentages,  $p$ , of 1.0, 0.1, 0.01, and 0.001%, the factor in brackets assumes the respective values of 0.85, 0.90, 0.95, and 1.0. Thus, at a time percentage of 1%, the net  $XPD_p$  (in dB) after accounting for ice depolarization is 85% of  $XPD_{rain}$  (e.g., if  $XPD_{rain}$  does not exceed 30 dB for 1% of the time, the corresponding  $XPD_p$  degrades to 25.5 dB after accounting for ice effects). At a time percentage of 0.001%, however, no adjustment is applied for ice depolarization.

### 5.2.1.2 Frequency dependence

In Figure 5.3, the relation between rain depolarization and rain attenuation given by the method in § 4.1 of Recommendation ITU-R P.618 is plotted for frequencies of 8, 12, 20 and 30 GHz, assuming circular polarization ( $\tau = 45^\circ$ ) and an elevation angle of  $30^\circ$  (but ignoring the small canting-angle term). The  $XPD_{rain}$  (and consequently,  $XPD_p$ ) corresponding to a fixed value of  $A_p$  decreases (worsens) as the frequency decreases. Conversely, over the range of the model,  $A_p$  increases (becomes worse) as frequency increases. Therefore, the determination of the relative importance of attenuation and depolarization in a frequency re-use telecommunication system requires estimates of both quantities.

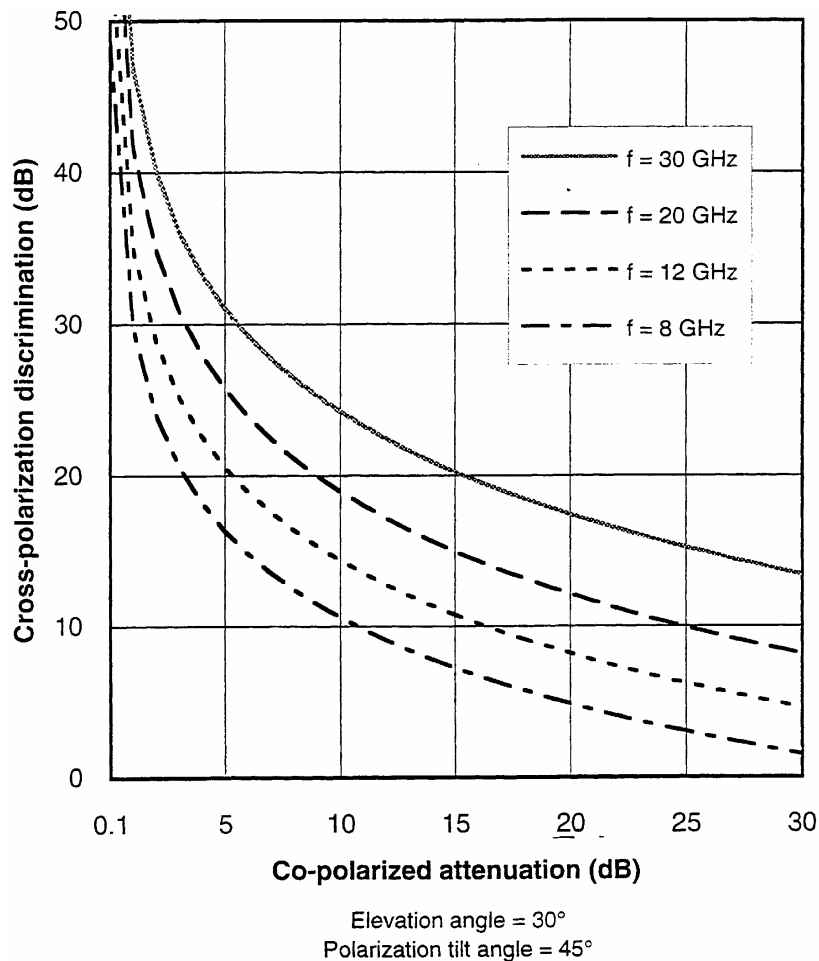


FIGURE 5.3

**Plot of rain XPD vs co-polar rain attenuation,  
illustrating frequency dependence**

In the 6/4 GHz frequency bands, however, path attenuation is low and rain attenuation estimates are not very useful for predicting XPD statistics. For these bands, where depolarization can be quite important, the frequency-scaling method given in § 4.3 of Recommendation ITU-R P.618 can be used with attenuation estimates for a higher frequency (e.g., 8 GHz) or with measured attenuation statistics for a higher frequency, if available, to estimate the cross-polarization.

To estimate XPD statistics at frequencies below about 8 GHz, it is also possible to employ relationships between XPD, point rain rate, and effective path length [Oguchi, 1977; Kobayashi, 1977]. A simple technique to predict an overall cumulative distribution of XPD with this approach has been proposed by Olsen and Nowland [1978].

The XPD corresponding to a fixed value of attenuation increases as frequency increases, so the XPD predicted for a given frequency and system configuration tends to yield a conservative estimate for higher frequencies. For example, an XPD estimate for the upper frequency limit of 35 GHz in the ITU-R model represents a conservative estimate for frequencies above 35 GHz.

### 5.2.1.3 Dependence on time percentage

Three terms in the XPD prediction method depend on time percentage. Foremost among these is the relation between  $XPD_p$  and co-polar attenuation,  $A_p$ . The required  $A_p$  value(s) are obtained from measured or predicted cumulative rain attenuation statistics for the propagation path in question. As shown in § 5.2.1.1, the empirical adjustment that is applied to the estimated  $XPD_{rain}$  to account for ice depolarization also depends on the time percentage.

The other term that is explicitly dependent on time percentage is the canting-angle term,  $C_\sigma$ , given by

$$C_\sigma = 0.0052 \sigma^2 \quad \text{dB} \quad (5.5)$$

where  $\sigma$  is the effective standard deviation (deg) of the canting-angle distribution, with values of  $0^\circ$ ,  $5^\circ$ ,  $10^\circ$  and  $15^\circ$  for the respective time percentages of 1.0, 0.1, 0.01, and 0.001%. As evident in Figure 5.4,  $\sigma$  depends linearly on the logarithm of the time percentage over the range of applicability of the model, and can be fit with the corresponding simple equation

$$\sigma = -5 \log(p) \quad \text{deg} \quad (5.6)$$

To obtain a more convenient form for machine calculation, Equations (5.5) and (5.6) may be combined to yield

$$C_\sigma = 0.13 (\log p)^2 \quad \text{dB} \quad (5.7)$$

for the range  $0.001 \leq p \leq 1.0$ . The resulting correction is small, ranging from zero at  $p = 1\%$  to 1.17 dB at  $p = 0.001\%$ .

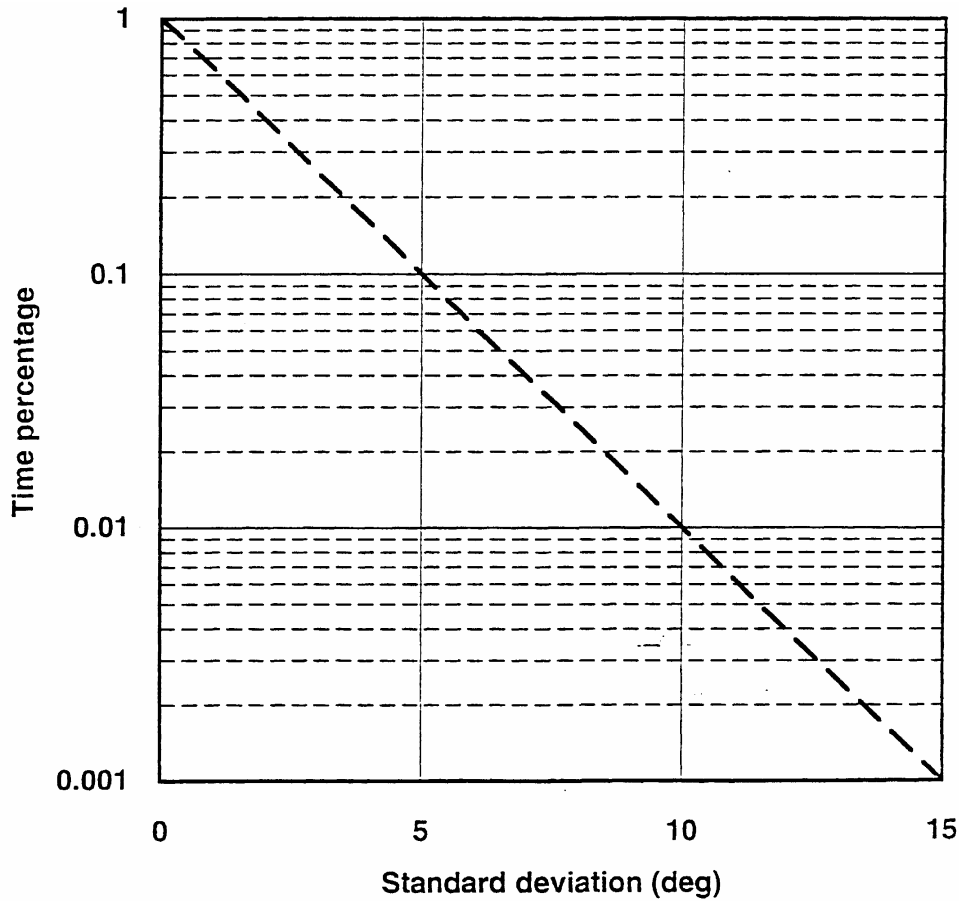


FIGURE 5.4

**Relation between standard deviation of the canting-angle distribution and time percentage**

### 5.2.2 Dependence on path configuration

The achievable performance of a propagation link with respect to depolarization depends not only on the geometry of the path, but also on the type of polarization and, for linear and elliptical polarization, on the polarization tilt angle with respect to local vertical at the earth station. The path elevation angle also influences the net asymmetry perceived by a wave during propagation through rainfall (maximum for a horizontal path, but virtually nil at zenith where the raindrops appear nearly symmetrical to the incident wave). As shown in § 5.2, XPD depends statistically on path attenuation, which itself is strongly dependent on path elevation angle.

Asymmetric hydrometeors tend to fall with their major symmetry axes aligned on average with the local vertical [Cox, 1981], thus the tilt angle of linear or elliptical polarization is quite important.

Given the satellite and earth station locations, the path elevation and azimuth angles and range to the satellite can be calculated using standard methods (e.g., [Morgan and Gordon, 1989]). In the most general case, the satellite boresight beam intersects the Earth at a point ( $a'$ ,  $b'$ ) where  $a'$  is the latitude

and  $b'$  is the difference between the satellite longitude and the longitude of the intersection point. The polarization tilt angle,  $\tau$ , of linear or elliptical polarization referenced to the vertical at the earth station, may be computed from [Shkarofsky and Moody, 1976]

$$\tau = \arctan \left[ \frac{\sin a' \cdot \cos a \cdot \sin b - \cos a' \cdot \sin b' \cdot \sin a}{\sin a' \cdot \sin a + \cos a' \cdot \sin b' \cdot \cos a \cdot \sin b} \right] \quad (5.8a)$$

where  $a$  is the earth station latitude (positive for the Northern hemisphere, negative for the Southern hemisphere), and  $b$  is the satellite longitude minus the earth station longitude (in degrees East).

However, if the satellite boresight beam intersects the Earth at the same longitude as the satellite longitude ( $b' = 0$ ), Equation (5.8a) reduces to

$$\tau = \arctan (\sin b / \tan a) = 90^\circ - \arctan (\tan a / \sin b) \quad (5.8b)$$

still referenced to vertical at the earth station, or

$$\tau = \arctan (\tan a / \sin b) \quad (5.8c)$$

referenced to the horizontal at the earth station [Barton, 1975], which is the preferred reference, as the local horizontal is always perpendicular to the propagation path. The above derivation assumes that one satellite polarization axis is parallel to the equator. However, if the polarization at the satellite is rotated from this reference direction by an angle  $\Delta\zeta$ , the value of  $\tau$  given by Equation (5.8) is simply incremented by  $\pm\Delta\zeta$  (with the sign depending on the sense of polarization rotation at the satellite).

For circular polarization, the tilt angle  $\tau$  is set equal to  $45^\circ$ .

### 5.2.3 Evaluations of model performance

Evaluations of XPD models with measured data [Yamada and Karasawa, 1990] confirm good performance of the method in Recommendation ITU-R P.618. Results of such tests have also been used to improve the model by quantifying the terms for raindrop canting angle and ice-crystal depolarization in terms of time percentage.

### 5.2.4 Joint statistics of XPD and attenuation

If available, joint cumulative probability distributions of XPD and attenuation are preferred for systems design [Howell *et al.*, 1992], particularly for Earth-space paths where the variability in path XPD for a given  $A_p$  (mainly caused by ice depolarization) is large for attenuations near the system fade margin. When applied to the calculation of fading margins in systems using dual polarization, however, the use of an equiprobability relation between  $XPD_p$  and  $A_p$  for outage calculations may give similar results as the use of joint probabilities [van Cappellen *et al.*, 1980].

The conditional probability distribution of XPD for a given value of attenuation can be modelled by assuming that the cross-polar to co-polar voltage ratio,  $r = 10^{-XPD/20}$ , obeys a normal distribution. Parameters of the distribution are: the mean value,  $r_m$ , which is found to be very close to  $10^{-XPD_{rain}/20}$ , where  $XPD_{rain}$  is calculated with the method in Recommendation ITU-R P.618; and the standard deviation,  $s_r$ , which assumes the almost-constant value of 0.038 for  $3 \text{ dB} \leq A_p \leq 8 \text{ dB}$ . These results for the conditional probability distribution of XPD for a given value of attenuation are based on studies with the SIRIO satellite [Mauri *et al.*, 1987].

### 5.2.5 Long-term frequency and polarization scaling

A method for scaling measured or predicted XPD statistics for one frequency and polarization tilt angle to another frequency and tilt angle is provided in § 4.3 of Recommendation ITU-R P.618. This method is particularly useful for scaling measured XPD statistics to another frequency and for extending statistics predicted with the method of § 4.1 down to the 6/4 GHz bands.

## 5.3 Dependence of XPD and XPI on physical processes

Expressions describing the dependence of path depolarization on the physical mechanisms (rotation of the polarization plane, differential attenuation and differential phase shift) that cause the effect can be derived. While not as useful for system applications as are the statistical predictions described above, the results clarify the physical processes that generate path depolarization.

### 5.3.1 Faraday rotation in the ionosphere

As discussed in § 5.1.5, the degradation in cross-polarization isolation caused by rotation of the plane of linear polarization is given by

$$\Delta XPI = -20 \log (\tan \Delta\phi) \quad \text{dB} \quad (5.9)$$

where  $\Delta\phi$  is the net rotation. For a one-way traversal of the ionosphere at an elevation angle of  $30^\circ$ , Recommendation ITU-R P.531 provides a worst-case estimate of  $\Delta\phi = 108^\circ$  at 1 GHz. Estimates for other frequencies can be derived from  $1/f^2$  scaling, as described in § 7.3.1.

Based on these data, Faraday rotation will seldom exceed  $1^\circ$  at frequencies of 14/12 GHz (corresponding to a path XPI of 35 dB, a modest degradation), and will be negligible at 30/20 GHz. At 6/4 GHz, however,  $\Delta\phi$  can reach several degrees in regions where ionospheric impairments are strong (i.e., near the magnetic equator and in the auroral zones), and at frequencies below about 250 MHz may exceed several rotations of the polarization plane.

As viewed from an earth station, the linear polarization planes rotate in opposite directions on the up- and down-links. It is therefore not possible to compensate for Faraday rotation by rotating the feed system of the antenna, if the same antenna is used for both transmitting and receiving. Compensation methods involving feed rotation can be used for various cases [Wolff, 1985]. As already noted, this effect is not observed with circular polarization.

### 5.3.2 Precipitation effects

#### 5.3.2.1 Differential attenuation

The rotation  $\Delta\tau$  (deg) of a plane of polarization caused by differential attenuation,  $\Delta A$  (dB), between orthogonal components of the polarization vector (e.g., with respect to the axes of a canted raindrop) may be expressed as [Lee, 1977]

$$\Delta\tau = |\phi - \tau| - \tan^{-1} \left[ (10^{-\Delta A/20})^{\pm 1} \tan |\phi - \tau| \right] \quad \text{deg} \quad (5.10)$$

where  $\phi$  is the “average canting angle” of the depolarizing medium (about  $0^\circ$  on average for rain and ice events [Cox, 1981]), and  $\tau$  is the tilt angle of the incident polarization vector; the  $\pm$  sign is positive for incident left-hand (LH) elliptical polarization and negative for RH polarization. Equation (5.10) predicts unequal rotations for RH and LH polarizations, indicating how differential attenuation deorthogonalizes incident orthogonal polarizations.

Existing propagation data [Hendry *et al.*, 1980; Cox and Arnold, 1982; Jakoby and Rucker, 1993] indicate that on average  $\Delta A$  is about 0.25 dB for co-polar attenuation  $A_p = 5$  dB, about 0.75 dB for  $A_p = 10$  dB, and about 1.5 dB for  $A_p = 15$  dB, but can approach 2 dB for the latter case. Hence, substantial polarization rotations may be encountered in systems with large attenuation margins. Nevertheless, the corresponding degradation in XPD is overshadowed by the XPD created by degradation of the axial ratio of the wave (see next section).

### 5.3.2.2 Differential phase

Any differential phase shift,  $\Delta\beta$ , experienced by an incident wave induces a rotation of the polarization vector, given by [Lee, 1977]

$$\Delta\tau' = |\phi - \tau| + 0.5 \tan^{-1}[(2 \cot |\phi - \tau| \cos \Delta\beta / (1 - \cot^2 |\phi - \tau|))] \quad (5.11)$$

and furthermore causes a degraded value of the voltage axial ratio,  $AR$ , of the wave:

$$AR = 20 \log \{ \tan [ 0.5 ( \pi - \sin^{-1} (\pm \sin \Delta\beta \sin 2 |\phi - \tau|) ) ] \} \quad \text{dB} \quad (5.12)$$

where again the  $\pm$  sign is positive for incident left-hand (LH) elliptical polarization and negative for RH polarization.

Measurements of differential phase shift indicate that at 12 GHz,  $\Delta\beta$  can approach  $6^\circ$  in heavy snow; about  $15^\circ$  in rain, possibly reaching  $30^\circ$  in very heavy rain (when attenuation will also be very high); and  $20^\circ$  in ice crystals above the rain or in mixed ice/rain regimes. The rotation of the plane of polarization  $\Delta\tau'$  caused by differential phase thus seldom exceeds a few degrees.

Among the above contributions, the degradation in axial ratio is the primary contributor to XPD on most propagation paths. Statistics of path XPD arising from the sum of these effects are estimated with a relation between XPD and path attenuation as provided in Recommendation ITU-R P.618.

## 5.4 Data relevant to cross-polarization compensation

Experiments have shown a strong correlation between 6 GHz and 4 GHz rain depolarization on Earth-space paths, both in the long term and on an event basis [Ogawa and Allnutt, 1982; Matsunaka *et al.*, 1983], demonstrating the feasibility of up-link depolarization compensation utilizing concurrent down-link depolarization data. The experiments were conducted at path elevation angles of  $38^\circ$  and  $9^\circ$ , respectively, in different climates. Only differential phase effects were apparent, even for severe rain events, and single-parameter compensation for differential phase is sufficient at 6/4 GHz. Analytical investigations [Overstreet and Bostian, 1979; McEwan *et al.*, 1981] indicate that single-parameter depolarization compensation systems may also be useful for some applications at higher frequencies.

Measurements at 6 and 4 GHz indicate that 99% of the XPD variations are slower than  $\pm 4$  dB/s, or equivalently, less than  $\pm 1.5$  deg/s in the mean path differential phase shift. Therefore, the time constant of a depolarization compensation system at these frequencies need only be about 1 s [Matsunaka *et al.*, 1983; Allnutt, 1984].

Cross-polarization measurements [Howell, 1977; Fimbel and Ramat, 1977] have also shown that the relative phase between the co- and cross-polar signals is typically fairly constant (of the order of  $\pm 20^\circ$ ), but that under certain conditions, abrupt changes of the order of  $180^\circ$  can occur. Abrupt changes in XPD of several decibels have been observed to occur within 0.1 to 0.3 s, coincident with lightning strokes, suggesting changes in the alignment of ice crystals [Howell, 1977; Watson *et al.*, 1979].

In some dual-polarized systems operating at frequencies above 10 GHz, site diversity or up-link power control may be required to reduce rain impairments, especially at low elevation angles. To evaluate the magnitude of the cross-polarized component that remains after applying site diversity or power control, data in the form of joint depolarization and attenuation statistics are required (see § 5.2.4). Measurements at an elevation angle of  $6.6^\circ$  [Yamada *et al.*, 1985] have shown that tropospheric scintillation leads to increased durations of low-level attenuation events without causing depolarization, thus significantly affecting such joint statistics.

### 5.5 Incorporation of path XPD into system XPI

The cross-polar terms contributed by a satellite antenna ( $XPI_{sat}$ ), the path XPD, and an earth station antenna ( $XPI_{es}$ ) are complex quantities with both amplitude and phase components that add as vectors in the complex plane. The net XPD detected by the receiver is the sum of these and possibly other system contributions of potentially quite different amplitudes and phases.

An example is shown in Figure 5.5, where the arbitrary vectors  $V_1$ ,  $V_2$  and  $V_3$  are summed in the complex plane (referenced to the phase of  $V_1$ ) to yield a resultant,  $\mathcal{R}$ . If  $V_1$  and  $V_2$  correspond to the respective residual isolations  $XPI_{sat}$  and  $XPI_{es}$ , and  $V_3$  to the path XPD, the resultant  $\mathcal{R}$  is only weakly dependent on the path depolarization, and the net isolation is dominated by system effects when antenna isolations are poor. In order for path depolarization to exert a regular and predictable effect on the system isolation, the path XPD during impaired conditions must dominate the residuals.

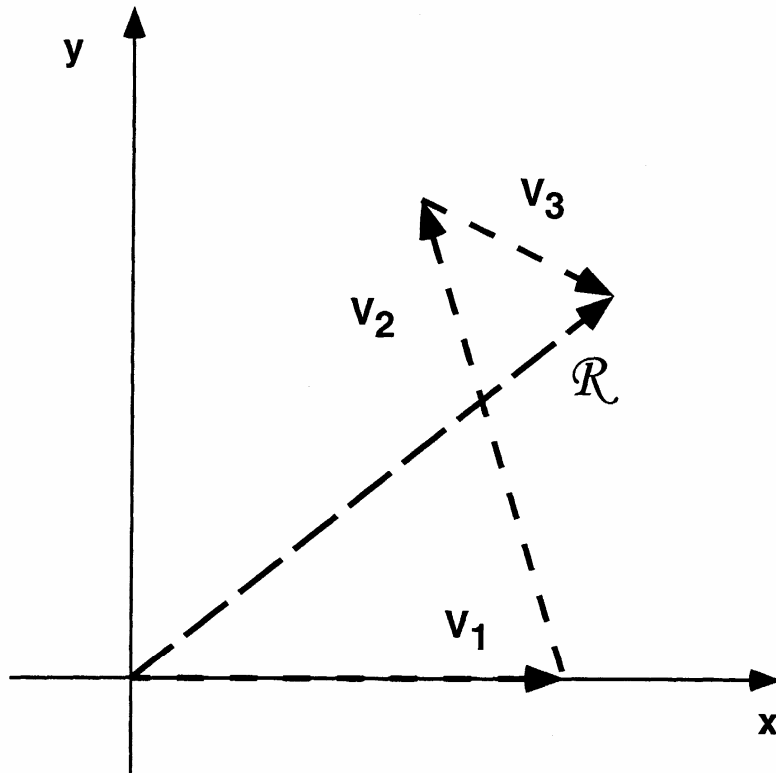


FIGURE 5.5

**Addition of three arbitrary vectors in the complex plane to yield a resultant,  $\mathcal{R}$**

Under the simplifying assumption of worst-case (co-linear) addition, the individual XPD components combine by simple voltage addition:

$$XPD_{net} = -20 \log [10^{-XPI_{sat}/20} + 10^{-XPD_{path}/20} + 10^{-XPI_{es}/20}] \quad (5.13)$$

In this case, the net XPD is dominated by, and is always lower (worse) than, the least (poorest) value of XPI or XPD in the summation.

The clear-sky system cross-polarization isolation may vary with satellite station-keeping manoeuvres, antenna mispointing, and refractive ray bending that leads to off-axis signal reception (unless compensated for by the antenna tracking system). In operational frequency re-use systems, the cross-polar residual isolations of the satellite and earth station antennas are kept small, or coding or some type of cross-polar cancellation may be used to maintain tolerable isolation. If the satellite or earth station component of isolation is poor, system performance in a dual-polarized environment can be dominated by equipment effects, independent of path impairments.

## 5.6 Example calculation of path XPD

To illustrate its use, the procedure of Recommendation ITU-R P.618 is applied to estimate the path depolarization for a representative Earth-space path. Because the method relates statistics of  $XPD_p$  to co-polar rain attenuation, values of  $A_p$  should be available for all time percentages of interest at the outset of the calculation. In this example, a cumulative distribution of rain attenuation is calculated for a hypothetical propagation path using the prediction procedure of Recommendation ITU-R P.618. If available, measured attenuation statistics for the desired frequency, or statistics scaled from attenuation data at another frequency, could also be used as the source for the  $A_p$  statistics.

### 5.6.1 Step-by-step application of the method

Assume that impairment statistics are required to plan a 12 GHz linearly-polarized up-link path to a geostationary satellite. The earth station is located at a latitude of  $45^\circ$ , and the difference between the satellite and station longitudes is  $55^\circ$ . The boresight of the satellite beam intersects the Earth at the same longitude as the satellite longitude. The terminal is situated in ITU-R rain climatic zone H, for which the rain rate exceeded for 0.01% of the time is expected to be 32 mm/h (see Recommendation ITU-R P.837). The terminal height above mean sea level is 100 m (i.e.,  $h_s = 0.1$  km).

For the given configuration, the path elevation angle is computed to be  $15.6^\circ$ , and the polarization tilt angle is computed from Equation (5.8c) to be  $50.7^\circ$  with respect to horizontal at the ground. From Recommendation ITU-R P.838, the specific-attenuation coefficients for 12 GHz corresponding to the elevation and tilt angles are calculated to be  $k = 0.0176$  and  $\alpha = 1.207$ . By applying the rain-attenuation prediction procedure of Recommendation ITU-R P.618 (see § 3.2.5 of this handbook for a detailed example calculation), the cumulative rain-attenuation distribution of Figure 5.6 is obtained.

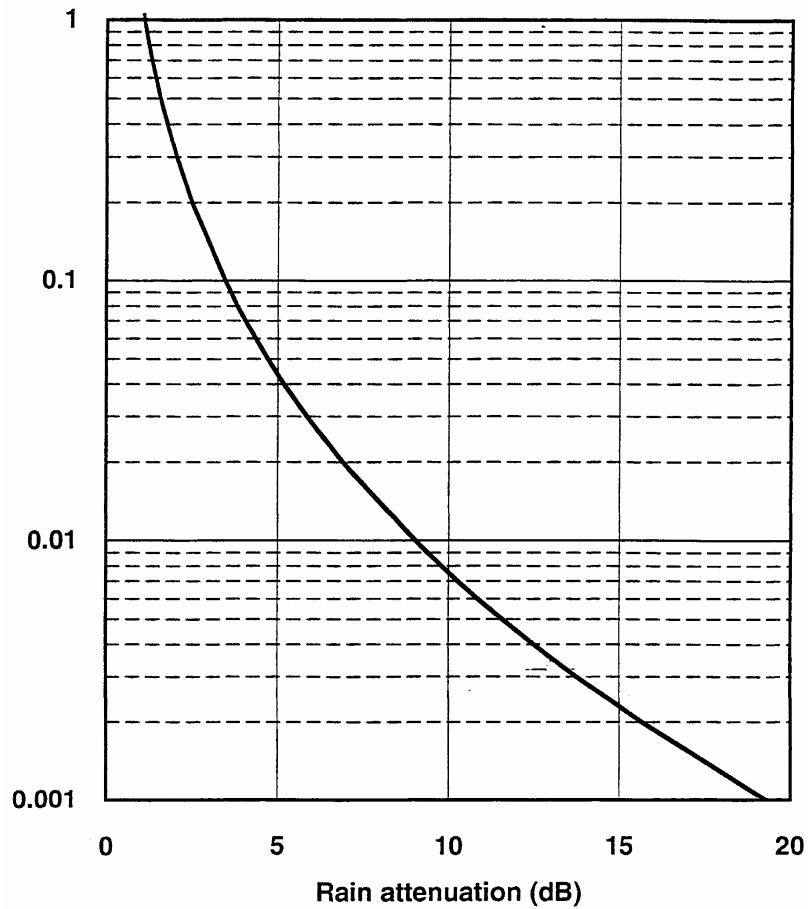


FIGURE 5.6  
Rain attenuation statistics for 12 GHz propagation path  
in example calculation

Once the required rain attenuation statistics are available, application of the step-by-step XPD prediction method of § 4.1 of Recommendation ITU-R P.618 is quite straightforward, as illustrated here:

*Step 1:* The frequency-dependent term for  $f = 12$  GHz is computed to be

$$C_f = 30 \log f = 32.4 \quad \text{dB} \quad (5.14)$$

*Step 2:* Since  $8 \leq f \leq 20$  GHz, the required coefficient  $V(f)$  in the attenuation-dependent term is

$$V(f) = 12.8 f^{0.19} = 20.5 \quad (5.15)$$

This coefficient is used in conjunction with the  $A_p$  values shown in Figure 5.6 to construct a table of rain-attenuation dependent terms for the required time percentages from the expression

$$C_A = V(f) \log A_p = 20.5 \log A_p \quad \text{dB} \quad (5.16)$$

While the resulting table is not reproduced here, the procedure is quite straightforward, especially in a computer or spreadsheet implementation.

*Step 3:* The polarization improvement factor for  $\tau = 50.7^\circ$  is

$$C_\tau = -10 \log [1 - 0.484 (1 + \cos 4\tau)] = 0.17 \quad \text{dB} \quad (5.17)$$

*Step 4:* For  $\theta = 15.6^\circ$ , the elevation angle term is

$$C_\theta = -40 \log (\cos \theta) = 0.65 \quad \text{dB} \quad (5.18)$$

*Step 5:* Using the curve fit of § 5.2.1.3, the canting-angle correction is computed for the required time percentages from Equation (5.7):

$$C_\sigma = 0.13 (\log p)^2 \quad \text{dB} \quad (5.19)$$

The corrections are tabulated versus time percentage,  $p$ , as were the  $C_A$  coefficients in Step 2.

*Step 6:* With the above coefficients calculated in Steps 1 - 5, the rain depolarization component is calculated and tabulated for the desired time percentages with the expression

$$XPD_{rain} = 32.4 - 20.5 \log A_p + 0.17 + 0.65 + 0.13 (\log p)^2 \quad \text{dB} \quad (5.20)$$

*Step 7:* For the desired time percentages,  $p$ , the correction for ice depolarization is calculated from

$$C_{ice} = XPD_{rain} (0.3 + 0.1 \log p)/2 \quad \text{dB} \quad (5.21)$$

and the computations similarly tabulated.

*Step 8:* The net XPD corresponding to the required time percentages,  $p$ , is finally computed with

$$XPD_p = XPD_{rain} - C_{ice} \quad \text{dB} \quad (5.22)$$

The resulting cumulative statistics of  $XPD_p$  are presented for time percentages of 0.001% to 1% in Figure 5.7 for propagation performance assessment of the planned Earth-space link. Figures 5.6 and 5.7 are used to estimate the respective attenuation and XPD margins that are required to achieve a specified level of path availability or system performance.

## 5.6.2 Example of a system application

The attenuation and XPD estimates of Figures 5.6 and 5.7 can be applied to predict whether the performance of the planned link will be dominated by depolarization or attenuation impairments. As mentioned in § 5.2.4, it is preferable to use joint statistics of XPD and attenuation, if available, for this purpose, but such joint statistics are rare. Otherwise, equiprobable statistics of depolarization and attenuation are usually reliable indicators of the relative impairment levels.

The desired equiprobable plot of  $XPD_p$  versus  $A_p$ , derived from Figures 5.6 and 5.7 using equiprobable time percentage as a parameter, is shown in Figure 5.8. The predicted XPD levels are rather severe with respect to attenuation, which is not unexpected for the specified geometry (fairly low elevation angle and a polarization tilt angle near the worst-case value of  $45^\circ$ ).

Assume for illustration that the specified up-link path availability is 99.99% (i.e., unavailability of 0.01%). From Figure 5.6, the path attenuation exceeded for 0.01% of the time is 9.0 dB. If this fade margin can be provided for the link, Figure 5.8 indicates that the corresponding equiprobable XPD level is 13.4 dB, representing a significant level of cross-polarization interference for many systems. If this level of XPD is not tolerable in regard to performance objectives, the system design may have to incorporate reduction or restoration techniques [Allnutt, 1989] to reduce the effects of the cross-polarization impairments.

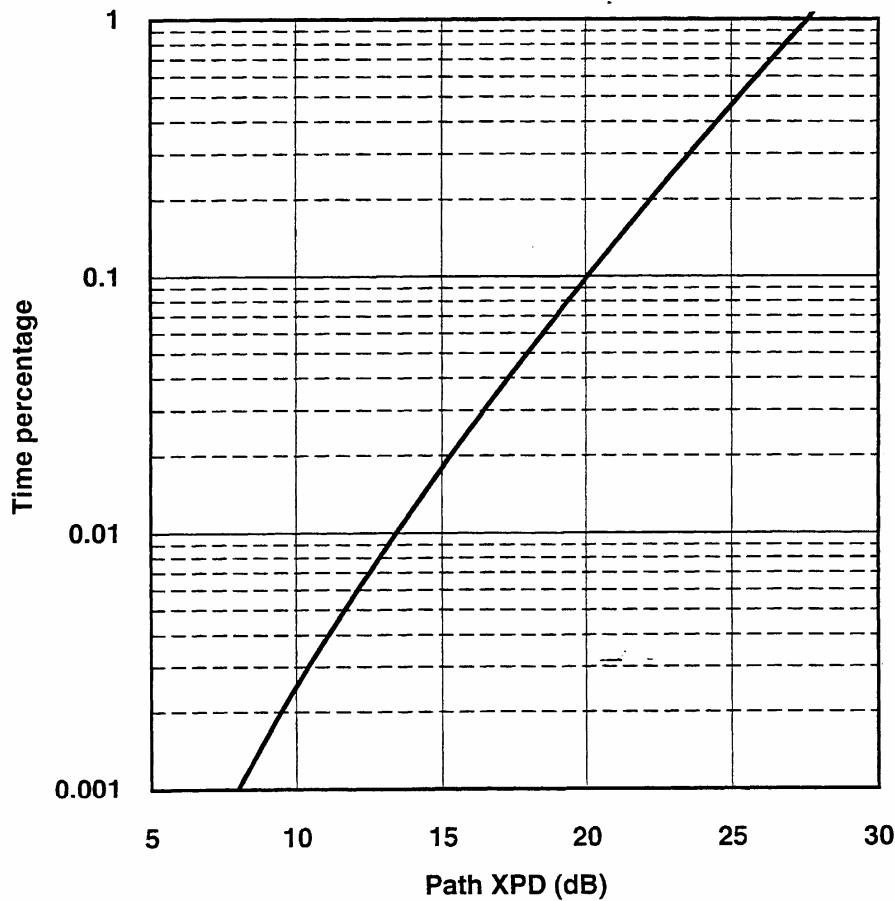


FIGURE 5.7

**Cumulative XPD statistics for 12 GHz  
propagation path in example calculation**

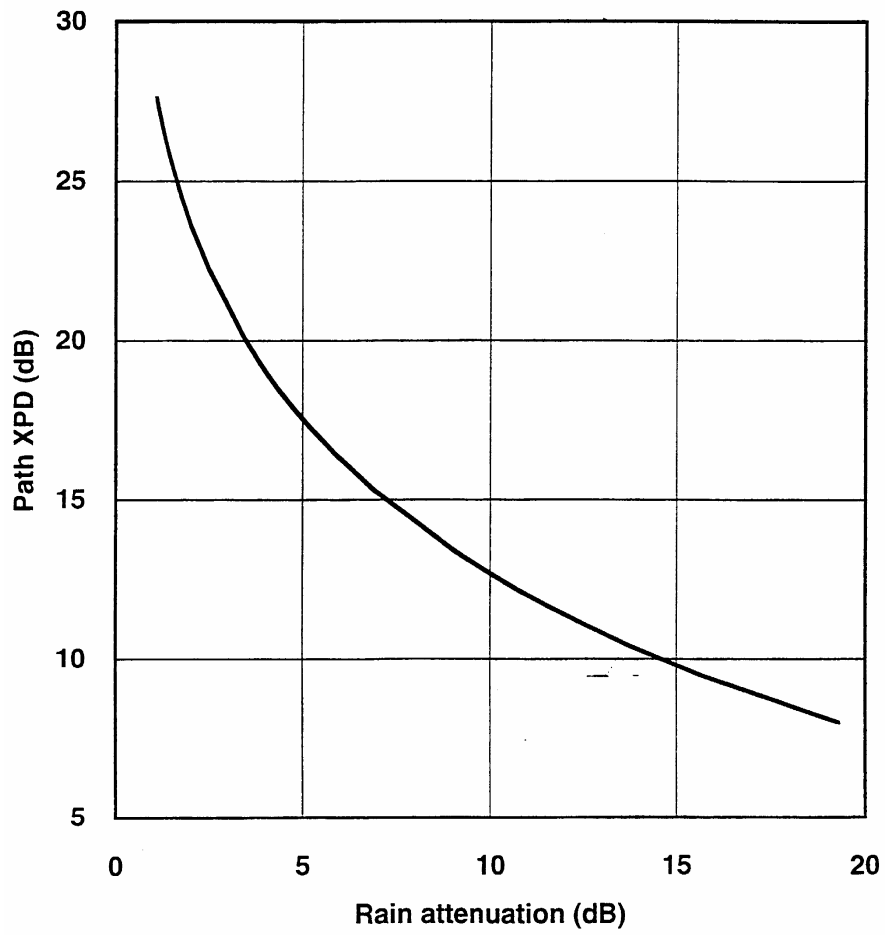


FIGURE 5.8

**Equiprobable plot of path XPD vs co-polar rain attenuation from example calculation**

REFERENCES FOR CHAPTER 5

- ALLNUTT, J.E. [1984] The system implications of 6/4 GHz satellite-to-ground signal depolarization: Results from the INTELSAT propagation measurement programme," *Intl. J. Satell. Commun.*, Vol. 2, 73-80.
- ALLNUTT, J.E. [1989] *Satellite-to-Ground Radiowave Propagation*, Chap. 5, Depolarization effects, 249-318. Peter Peregrinus Ltd., London.
- BARTON, S.K. [1975] Polarization distortion in systems employing orthogonal polarization frequency reuse. *Marconi Rev.*, XXXVIII, 153-168.
- BECKMANN, P. [1968] *The Depolarization of Electromagnetic Waves*, § 1.5, Mathematical representation of polarization, 24-38. Golem Press, Boulder, USA.
- CHU, T.S. [1971] Restoring the orthogonality of two polarizations in radio communication systems, I. *BSTJ*, Vol. 50, 9, 3063-3069.
- CHU, T.S. [1982] A semi-empirical formula for microwave depolarization versus rain attenuation on Earth-space paths. *IEEE Trans. Comm.*, Vol. COM-30, 12, 2550-2554.
- COX, D.C. [1981] Depolarization of radio waves by atmospheric hydrometeors in Earth-space paths: A review. *Radio Sci.*, Vol. 16, 5, 781-812.
- COX, D.C. and ARNOLD, H.W. [1982] Results from the 19- and 28-GHz COMSTAR satellite propagation measurements at Crawford Hill. *Proc. IEEE*, Vol. 70, 5, 458-488.
- COX, D.C. and ARNOLD, H.W. [1984] Comparison of measured cross-polarization isolation and discrimination for rain and ice on a 19-GHz space-Earth path. *Radio Sci.*, Vol. 19, 2, 617-628.
- DiFONZO, D.F., TRACHTMAN, W.S. and WILLIAMS, A.W. [1976] Adaptive polarization control for satellite frequency reuse systems. *COMSAT Tech. Rev.*, Vol. 6, 2, 253-283.
- DISSANAYAKE, A.W., HAWORTH, D.P. and WATSON, P.A. [1980] Analytical models for cross-polarization on Earth-space radio paths for frequency range 9-30 GHz. *Ann. Télécommunic.*, Vol. 35, 11-12, 398-404.
- FIMBEL, J. and RAMAT, P. [1977] Mesures de l'affaiblissement et de la depolarization a 20 GHz a partir du satellite ATS-6. *Proc. ATS-6 Meeting*, ESA Publ. SP-131, 79-84, Oct.
- FUKUCHI, H., AWAKA, J. and OGUCHI, T. [1984] Improved theoretical formula for the relationship between rain attenuation and depolarization," *Electron. Lett.*, Vol. 20, 21, 859-860.
- HENDRY, A., McCORMICK, G.C. and ANTAR, Y.M.M. [1980] Differential propagation constants on slant paths through snow as measured by 16.5 GHz polarization diversity radar. *Preprints URSI Comm. F Open Symp.*, Lennoxville, Canada, 6.7.1-6.7.6, 26-30 May.
- HOWELL, R.G. [1977] Crosspolar phase variations at 20 and 30 GHz on a satellite-Earth path. *Electron. Lett.*, Vol. 13, 405.
- HOWELL, R.G., HARRIS, J.W. and MEHLER, M. [1992] Satellite crosspolar measurements at BT Laboratories. *BT Tech. J.*, Vol. 10, 4, 52-67.

- IPPOLITO, L.J. [1981] Radio propagation for space communications systems. *Proc. IEEE*, Vol. 69, 6, 697-727.
- JAKOBY, R. and RÜCKER, F. [1993] Three years of crosspolar measurements at 12.5, 20 and 30 GHz with the Olympus satellite. *Proc. Olympus Utilisation Conf.*, Seville, Spain, 567-572, 20-22 April.
- KOBAYASHI, T. [1977] Degradation of cross-polarization isolation due to rain. *J. Radio Res. Labs. (Japan)*, Vol. 24, 114, 101-107.
- LEE, M.K. [1977] Cross-polarization performance of the RCA Satcom system. *RCA Rev.*, Vol. 38, 171-210, June.
- MATSUNAKA, N., MATSUZAWA, K., YUKI, H. and FURUTA, O. [1983] Correlation of 6 and 4 GHz rain-induced depolarization at low elevation angles. *Proc. URSI Comm. F Symp.*, Louvain, Belgium.
- MAURI, M., PARABONI, A. and TARDUCCI, D. [1987] Depolarization measurements and their use in the determination of dual polarization links performance. *Alta. Freq.*, Vol. LVI, 1-2, 47-55.
- McEWAN, N.J., GUNES, M. and MAHMOUD, M.S. [1981] RF methods for adaptive cancellation of cross-polarization in microwave satellite systems. *IEE Conf. Publ. No. 195*, Pt. 2, 188-192.
- McEWAN, N.J. and LEITAO, M.J. [1982] Propagation studies for feeder link design. Bradford University Research Ltd., Report 329, prepared for ESA under ESTEC Contract No. 4471/80/NL/DG, August.
- MORGAN, W.L. and GORDON, G.D. [1989] *Communications Satellite Handbook*, Chap. 6, Satellite Orbits, 774-870. Wiley-Interscience, New York.
- NOWLAND, W.L., OLSEN, R.L. and SHKAROFSKY, I.P. [1977] Theoretical relationship between rain depolarization and attenuation. *Electron. Lett.*, Vol. 13, 22, 676-678.
- OGAWA, A. and ALLNUTT, J.E. [1982] Correlation of 6 and 4 GHz depolarization on slant paths. *Electron. Lett.*, Vol. 18, 5, 230-232.
- OGUCHI, T. [1977] Scattering properties of Pruppacher-and-Pitter form raindrops and cross polarization due to rain: Calculations at 11, 19.3 and 34.8 GHz. *Radio Sci.*, Vol. 12, 1, 41-51.
- OGUCHI, T. [1983] Electromagnetic wave propagation and scattering in rain and other hydrometeors. *Proc. IEEE*, Vol. 71, 9, 1029-1078.
- OLSEN, R.L. and NOWLAND, W.L. [1978] Semi-empirical relations for the prediction of rain depolarization statistics: Their theoretical and experimental basis. *Proc. Int. Symp. on Antennas and Propagation*, 477-480, Sendai, Japan, August.
- OVERSTREET, W.P. and BOSTIAN, C.W. [1979] Crosstalk cancellation on linearly and circularly polarized communications satellite links. *Radio Sci.*, Vol. 14, 6, 1041-1047.
- ROGERS, D.V. [1985] Propagation considerations for satellite broadcasting at frequencies above 10 GHz. *IEEE J. Select. Areas Commun.*, Vol. SAC-3, 1, 100-110.

- ROGERS, D.V. and ALLNUTT, J.E. [1986] System implications of 14/11 GHz path depolarization. Part I: Predicting the impairments. *Intl. J. Satell. Commun.*, Vol. 4, 1-11.
- SHKAROFSKY, I.P. and MOODY, H.J. [1976] Performance characteristics of antennas for direct broadcasting satellite systems including effects of rain depolarization. *RCA Review*, Vol. 37, 279-319. (Sign error in equation 38 corrected in Shkarofsky, I.P. [1977] Depolarisation due to precipitation in satellite communications, *RCA Review*, Vol. 38, 257-309.)
- STUTZMAN, W.L. and RUNYON, D.L. [1984] The relationship of rain-induced cross-polarization discrimination to attenuation for 10 to 30 GHz Earth-space radio links. *IEEE Trans. Antennas Propagat.*, Vol. AP-32, 7, 705-710.
- VAN CAPPELLEN, J., MAWIRA, A., NEESSEN, J. and ZELDERS, F. [1980] Joint statistics of attenuation and cross-polarization measured with the OTS satellite. *Proc. NATO/AGARD Conf.*, No. 284, Paris.
- WATSON, P.A., McEWAN, N.J., DISSANAYAKE, A.W. and HAWORTH, D.P. [1979] Attenuation and cross-polarization measurements at 20 GHz using the ATS-6 satellite with simultaneous radar observations. *IEEE Trans. Ant. Prop.*, Vol. AP-27, 11-17.
- WOLFF, R.S. [1985] Minimization of Faraday depolarization effects on satellite communication systems at 6/4 GHz. *Intl. J. Satell. Commun.*, Vol. 3, 275-286.
- YAMADA, M., YASUKAWA, K., FURUTA, O., KARASAWA, Y. and BABA, N. [1985] A propagation experiment on Earth-space paths of low elevation angles in the 14 and 11 GHz band using the INTELSAT-V satellite. *Proc. Intl. Symp. Ant. Prop.*, Kyoto.
- YAMADA, M. and KARASAWA, Y. [1990] Model testing for XPD on Earth-space paths. Presented at URSI XXIII General Assembly, Prague, Czech., 28 August - 5 September.

## CHAPTER 6

### CLEAR AIR EFFECTS

#### 6.1 Loss due to defocusing and wave-front incoherence

The regular decrease of refractive index with height causes ray-bending and hence a defocusing effect at low elevation angles [ITU-R Handbook on Radiometeorology]. The magnitude of the defocusing of the antenna beam has been evaluated by Yokoi *et al.* [1970] and Crane [1971]. The loss is independent of frequency and is less than 0.4 dB at 3° elevation, even for very high values of refractivity at ground level. Expressions are provided in § 2.3.2 of Recommendation ITU-R P.618 to estimate the defocusing (beam-spreading) losses on paths at very low elevation angles. The loss is implicitly accounted for in the prediction methods for low-angle fading found in §§ 2.4.2 and 2.4.3 of the Recommendation.

Small-scale irregularities of the refractive index structure of the atmosphere cause incoherence in the wavefront at the receiving antenna. This results in both the rapid signal fluctuations discussed in the next section and an antenna-to-medium coupling loss that can be described as a decrease of the antenna gain. In practice, signal loss due to wave-front incoherence is probably only significant for large-aperture antennas, high frequencies, and elevation angles below 5°. Measurements made in Japan with a 22 m antenna [Yokoi *et al.*, 1970] suggest that at 5° elevation angle the loss is about 0.2 to 0.4 dB at 6/4 GHz. Measurements with a 7 m antenna at 15.5 GHz and 31.6 GHz gave losses of 0.3 and 0.6 dB, respectively, at a 5° elevation angle [Yamada and Yokoi, 1974].

#### 6.2 Scintillation and multipath effects

##### 6.2.1 General

Small-scale irregularities in the atmospheric refractive index cause rapid amplitude variations. Tropospheric effects in the absence of precipitation are unlikely to produce serious fading in space telecommunication systems operating at frequencies below about 10 GHz and at elevation angles above 10°. At low elevation angles and at frequencies above about 10 GHz, on the other hand, tropospheric scintillations can on occasion cause serious degradations in performance.

Irregularities in the ionosphere can also cause scintillation; information on this effect is given in § 7.4.

Tatarskii introduced a theoretical formula for the estimate of log-amplitude fluctuations based on the assumption that the spatial structure of the atmospheric refractive index is in accordance with a Kolmogorov-type spectrum [Tatarskii, 1961]. When the atmospheric turbulence lies in the inertial subrange of refractive index irregularities, the variance of log-amplitude in dB is given by

$$\sigma_x^2 = 42.9 \left( \frac{2\pi}{\lambda} \right)^{\frac{7}{6}} \int_0^L C_n^2(r) r^{\frac{5}{6}} dr \quad \text{dB}^2 \quad (6.1)$$

where  $L$  is the effective path length between the boundary of turbulence and the reception point;  $\lambda$  is the wavelength of the radio wave; and  $C_n$  is the structure parameter of the refractive index varying along the Earth-space path. It is known that the structure parameter depends not only on the variance of the atmospheric refractive index but also on the outer scale of irregularities [Ishimaru, 1978]. Therefore, it is not feasible to identify values of such parameters along a given slant path directly from the generally available meteorological quantities. Consequently, it remains difficult to calculate  $C_n$ .

For this reason, an empirical model was used by the ex-CCIR based on measured data at a frequency of 7.3 GHz, an elevation angle of 1°, and an antenna diameter of 36.6 m [Crane, 1976], with theoretical scaling for the frequency, elevation angle, and antenna diameter. This earlier model was composed of simple factors and was known to yield estimated values close to the measured values reported at that time. However, the model did not include meteorological parameters, and therefore could not account for regional and seasonal dependencies. The revised method in Recommendation ITU-R P.618 was developed to account for these factors based on the work by Karasawa *et al.* [1988a, b], Crane [1976], Lo *et al.* [1984], Rucker and Ortgies [1985], and Banjo and Vilar [1986].

## 6.2.2 Background of the scintillation model

### 6.2.2.1 Seasonal and diurnal variations

Based on a number of scintillation measurements [Karasawa *et al.*, 1988a; Banjo and Vilar, 1986; Vander Vorst *et al.*, 1982; Rucker and Ortgies, 1985], the seasonal and diurnal variations can be summarized as follows:

- 1) In mid-latitude regions where the seasonal variation of the meteorological environment is relatively large, scintillation has a marked seasonal dependence with a maximum during the summer months. For diurnal variations, larger scintillations were found to occur around 12:00-15:00, but the diurnal variation is smaller than seasonal variation in general. Figure 6.1 shows the diurnal and seasonal variations in the Yamaguchi measurements ( $f = 11.45$  GHz, elevation angle of 6.5°) [Karasawa *et al.*, 1988a].
- 2) The average value of scintillation intensity for each month shows a high correlation to the wet term refractivity  $N_{wet}$  (N unit), due to water vapour in the atmosphere, averaged over one month [Ortgies, 1989]. Figure 6.2 shows the relationship between the monthly-averaged r.m.s. fluctuation and  $N_{wet}$  from the Yamaguchi measurements.

In the scintillation prediction model of Recommendation ITU-R P.618, the relationship shown in Figure 6.2 was adopted with a minor modification incorporating scintillation data from other regions.

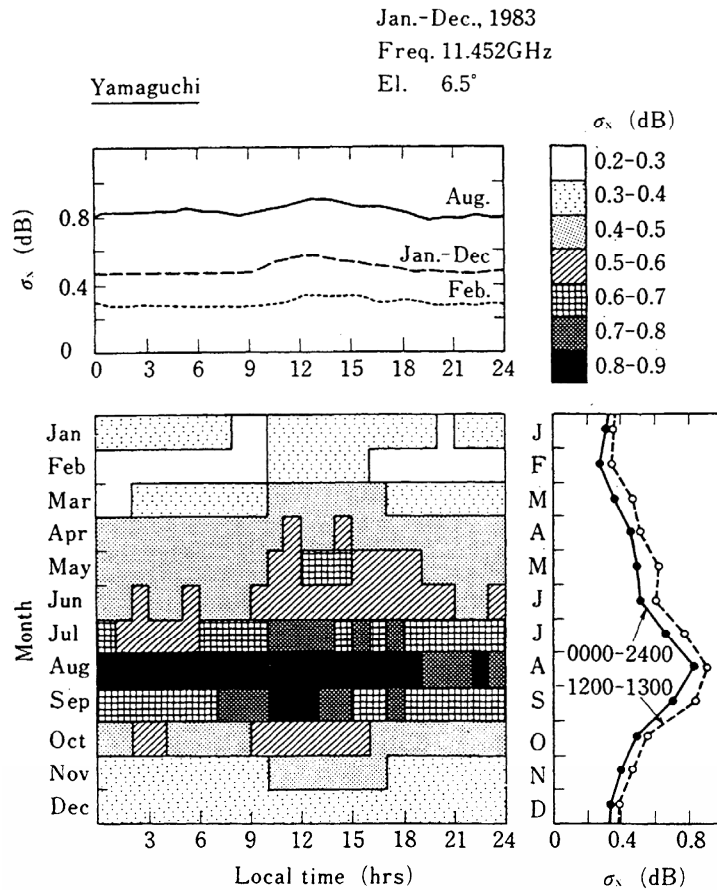


FIGURE 6.1

**Diurnal and seasonal variations of scintillation in a mid-latitude region.  
 Top left: diurnal variation. Bottom left: diurnal and seasonal variations.  
 Bottom right: seasonal variation**

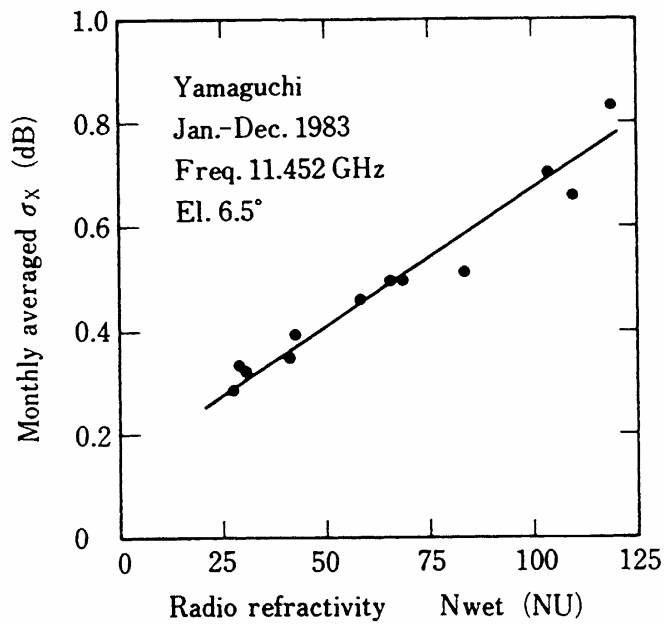


FIGURE 6.2

**Relation between monthly-averaged r.m.s. fluctuation and  $N_{wet}$   
 in the Yamaguchi measurement**

### 6.2.2.2 Frequency dependence

The frequency dependence of log-amplitude variation for frequencies at 11.5 GHz and 14.2 GHz was found to be the frequency raised to the power of 0.35 (i.e.,  $f^{0.35}$ ) [Karasawa *et al.*, 1988a]. It is also necessary to account for frequency effects due to antenna size. After eliminating the dependence due to the aperture averaging effect, a net frequency dependence of  $f^{0.45}$  was obtained for the frequencies above. The net frequency dependence, in the case of reception with sufficiently small antennas, is slightly smaller than the theoretical value of  $f^{7/12}$  derived from the Kolmogorov spectrum. Other experimental values range from  $f^0$  to  $f^{0.5}$  [Yokoi *et al.*, 1970; Thompson *et al.*, 1975; Ortgies and Rucker, 1992].

For this reason, the ITU-R prediction method uses  $f^{7/12}$  which is the theoretical value given in Equation (6.1).

### 6.2.2.3 Elevation angle dependence

The amplitude variation due to scintillation is proportional to  $(\text{cosec } \theta)^n$ . In one experiment, [Karasawa *et al.*, 1988a], long-term data at elevation angles  $\theta$  of 4.0° (satellite at 57°E), 6.5° (60°E), and 9.0° (63°E) were collected during September and October 1985, 1983, and 1982, respectively. The power  $n$  of  $(\text{cosec } \theta)^n$  was found to be about 1.3, much larger than the theoretical value of 11/12. Based on this and other measured data, the expression  $(\text{cosec } \theta)^{1.2}$  was adopted for the prediction method.

### 6.2.2.4 Antenna aperture diameter dependence

It is well known that the intensity of scintillation decreases with increasing diameter of the antenna aperture, due to wavefront incoherence [Tatarskii, 1961]. This phenomenon is called the antenna averaging effect. The formula in Recommendation ITU-R P.618 was that proposed by Haddon and Vilar [1986].

### 6.2.2.5 Probability density function (PDF) of signal-level variations

In the experiment cited above [Karasawa *et al.*, 1988a], the following results were obtained.

- 1) The probability density function of the amplitude variations (in dB) during relatively short time periods (about one hour) showed a Gaussian distribution, including fairly large scintillations with r.m.s. fluctuations up to 1.6 dB;
- 2) The distribution of the standard deviation itself for long-term variations over a month was closely approximated by a gamma distribution; likewise, there was not a very large deviation from a gamma distribution on a yearly basis; and
- 3) Between the monthly averaged value  $m$  of  $\sigma_\chi$  and the standard deviation  $\sigma_{\sigma_\chi}$  of  $\sigma_\chi$ , the relation  $m^2 = 10\sigma_{\sigma_\chi}^2$  was satisfied, which indicates that one of the two parameters essential for the determination of the gamma distribution is directly determined by the other.

Based on this, the formula used in Recommendation ITU-R P.618 was derived [Karasawa *et al.*, 1988b]. Figure 6.3 shows the time percentage dependent factor ( $\eta$  in the figure) for both signal fade and enhancement. The curve given by the dotted line was used in the development of the Recommendation ITU-R P.618 method. In contrast, experiments carried out in Europe at elevation angles of the order of 30° showed that the probability density of the standard deviation itself for long-term variations (item 2 above) is best approximated by a log-normal distribution when corrected for receiver noise [Ortgies, 1989; Haddon and Vilar, 1986].

### 6.2.2.6 Polarization dependence

Fluctuations measured simultaneously with one antenna at two different frequencies are found to be well correlated in time. Measurements at two different polarizations show that scintillation is independent of polarization [Cox, 1981].

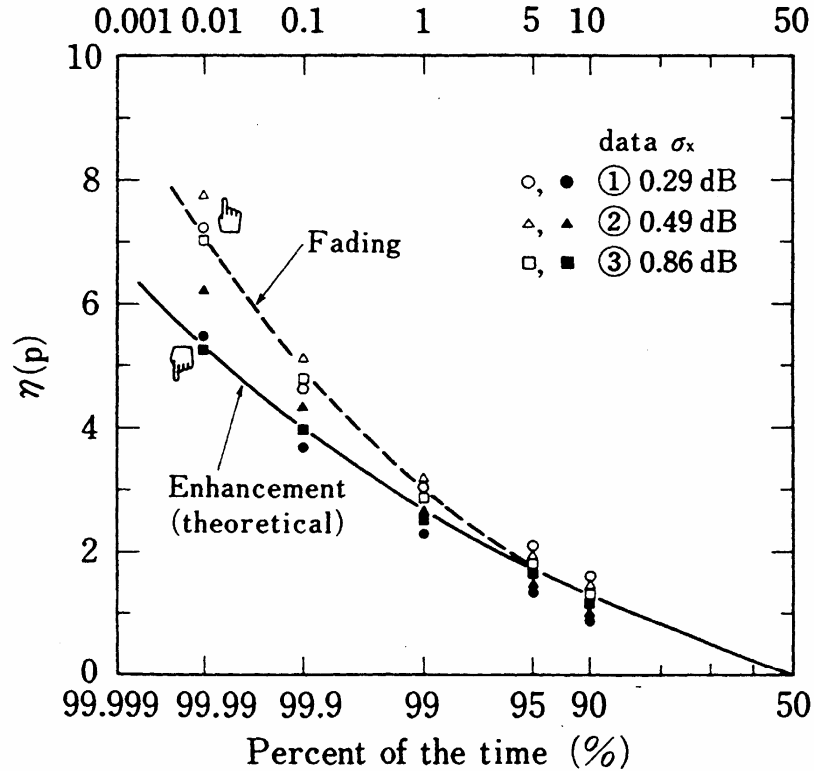


FIGURE 6.3

Time percentage factor for fading and enhancement

### 6.2.3 Accuracy and applicable range of the prediction method

#### 6.2.3.1 Accuracy and applicability of r.m.s. fluctuation prediction

The prediction accuracy of the ITU-R method was evaluated based on experimental data from a number of different climatic regions.

Figure 6.4 shows a scattergram between measured and predicted values for various conditions [Karasawa *et al.*, 1988b]. The parameter range covers frequencies from 7.3 to 14.2 GHz, elevation angles from 4° to 30°, and different climatic regions. It can be expected to apply for frequencies greater than 20 GHz. However, at elevation angles below 4°, unusually large signal fading caused by refractive index irregularities is likely to occur. Therefore, careful attention should be paid to applications of the model for very low-elevation angle cases (see § 6.2.4).

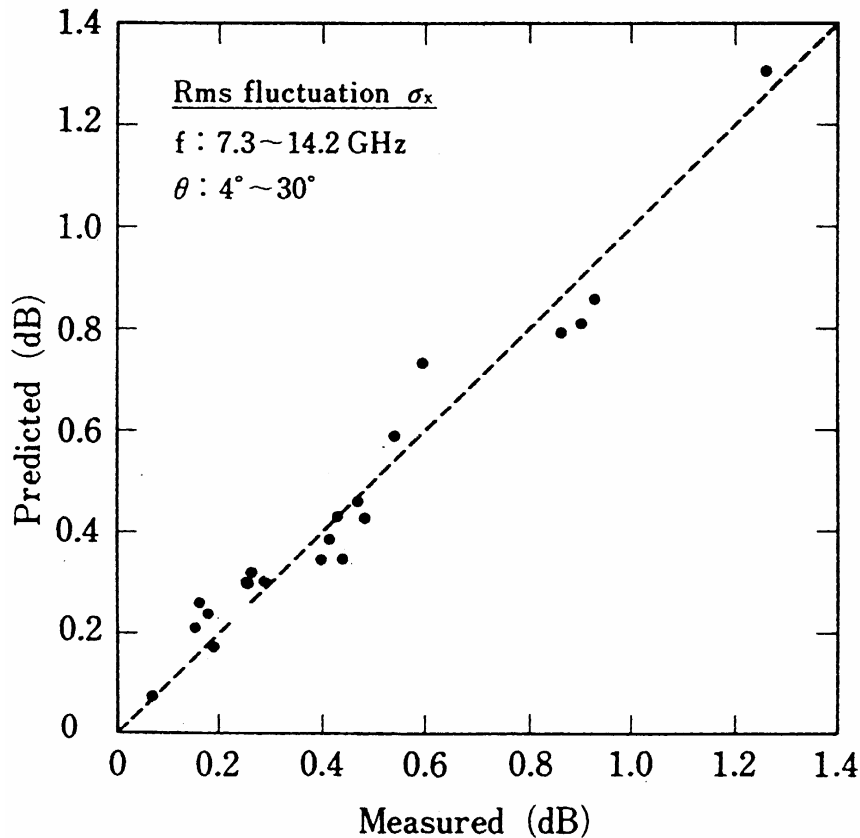


FIGURE 6.4

**Scattergram of r.m.s. fluctuation between measurements and predictions for various conditions (for detailed information, see Karasawa *et al.* [1988b])**

### 6.2.3.2 Accuracy and applicability of PDF prediction

Very good prediction accuracy was confirmed for data obtained in Japan and UK [Karasawa *et al.*, 1988b; Lo *et al.*, 1984; Banjo and Vilar, 1986]. However there are yet insufficient data for complete testing of the model. Moreover, few data at low-elevation angles (particularly below 4°) are available at the present time, so the applicability of the model to cases at very low-elevation angles still remains uncertain.

Therefore, the model of Recommendation ITU-R P.618 is expected to give an accurate prediction for scintillation fading occurring on Earth-space paths at elevation angles above approximately 4°. In the case of Earth-space paths at elevation angles below 4°, an empirical prediction method is found in §§ 2.4.2 and 2.4.3 of Recommendation ITU-R P.618.

### 6.2.4 Signal variations at elevation angles lower than about 5°

Clear-air refractive fading increases rapidly with decreasing path elevation angle. At elevation angles below about 5°, multipath effects due to large-scale tropospheric stratification and possibly surface reflection become increasingly important, and occur concurrently with defocusing (§ 6.1) and amplitude scintillation (§ 6.2.1). The propagation mechanism resulting from this complex

combination of phenomena is generally known as low-angle fading. An empirical method to predict fade statistics for elevation angles below  $5^\circ$  has been developed [Olsen, 1995], and is found in §§ 2.4.2 and 2.4.3 of Recommendation ITU-R P.618.

#### 6.2.4.1 Empirical model

The ITU-R method predicts the low-angle refractive fade distribution,  $A_{ref}(p)$ , resulting from the effects of defocusing (beam spreading), scintillation, and multipath. Climate and terrain conditions are accounted for by a geoclimatic factor,  $K_w$ , which is a function of a latitude factor  $C_{Lat}$  and a parameter  $C_0$  related to conditions for the lowest (most-affected) part of the propagation path. Calculations are first performed for the average worst month, from which statistics for the average year may also be derived. The shallow-fading part of the distribution is based on an interpolation between the fade depth exceeded for 63% of the average worst month or average year, and the time percentage that deep fading exceeds 25 or 35 dB (depending on model behaviour).

As low-angle fading on Earth-space paths is observed to behave similarly to terrestrial multipath fading, the model was developed by combining the limited low-angle fading data with the much more extensive knowledge of multipath fading on terrestrial links. Low-angle data measured at 7.3 GHz in the elevation angle range  $1^\circ$ - $4^\circ$  at Ottawa [McCormick and Maynard, 1972; Webber and McCormick, 1980] and Alert at 38 GHz [Lam, 1987] helped establish the elevation-angle dependence. Data for 4 and 30 GHz at St. John's [Webber and McCormick, 1980] support the use of the same frequency dependence for multipath fading as that employed for terrestrial links (Recommendation ITU-R P.530). Data for Ottawa ( $45^\circ\text{N}$ ,  $75^\circ\text{W}$ ) and Alert ( $83^\circ\text{N}$ ,  $62^\circ\text{W}$ ), together with  $1^\circ$  data for Eureka ( $80^\circ\text{N}$ ,  $86^\circ\text{W}$ ) [Strickland *et al.*, 1977; Kurniawan, 1986],  $3.3^\circ$  data for Goonhilly ( $50^\circ\text{N}$ ,  $5^\circ\text{W}$ ) [Bryant, 1992], and  $3.2^\circ$  data for Isfjord ( $78^\circ\text{N}$ ,  $13.6^\circ\text{E}$ ) [Gutteberg, 1983] provide additional support for the elevation-angle and frequency dependence, as well as a reasonable test of using the same climatic variability for multipath fading as employed for terrestrial links. Antenna diameters used for the measurements ranged from 0.45 m to 9 m, covering a large range of sizes likely to be employed in practice.

Model performance is illustrated in Figure 6.5, which compares measured and predicted worst-month clear-air fading distributions for Alert at several elevation angles. When the method was evaluated against data for very-low-angle paths, the mean and standard deviation of the prediction error were 0.4 dB and 5.3 dB, respectively, if logarithmic interpolation and extrapolation as described in § 6.2.4.1.2 is used to obtain the required climatic predictor,  $p_L$  [Olsen, 1995]. However, as the data base is small and since most of these data were also employed in the development of the method, it is anticipated that prediction errors confronted in practice may be somewhat larger. For comparison, the standard deviation of the prediction error computed from the much-larger set of terrestrial propagation data is 6.3 dB [Olsen and Tjelta, 1996].

Additional details of the model are supplied in the following two subsections.

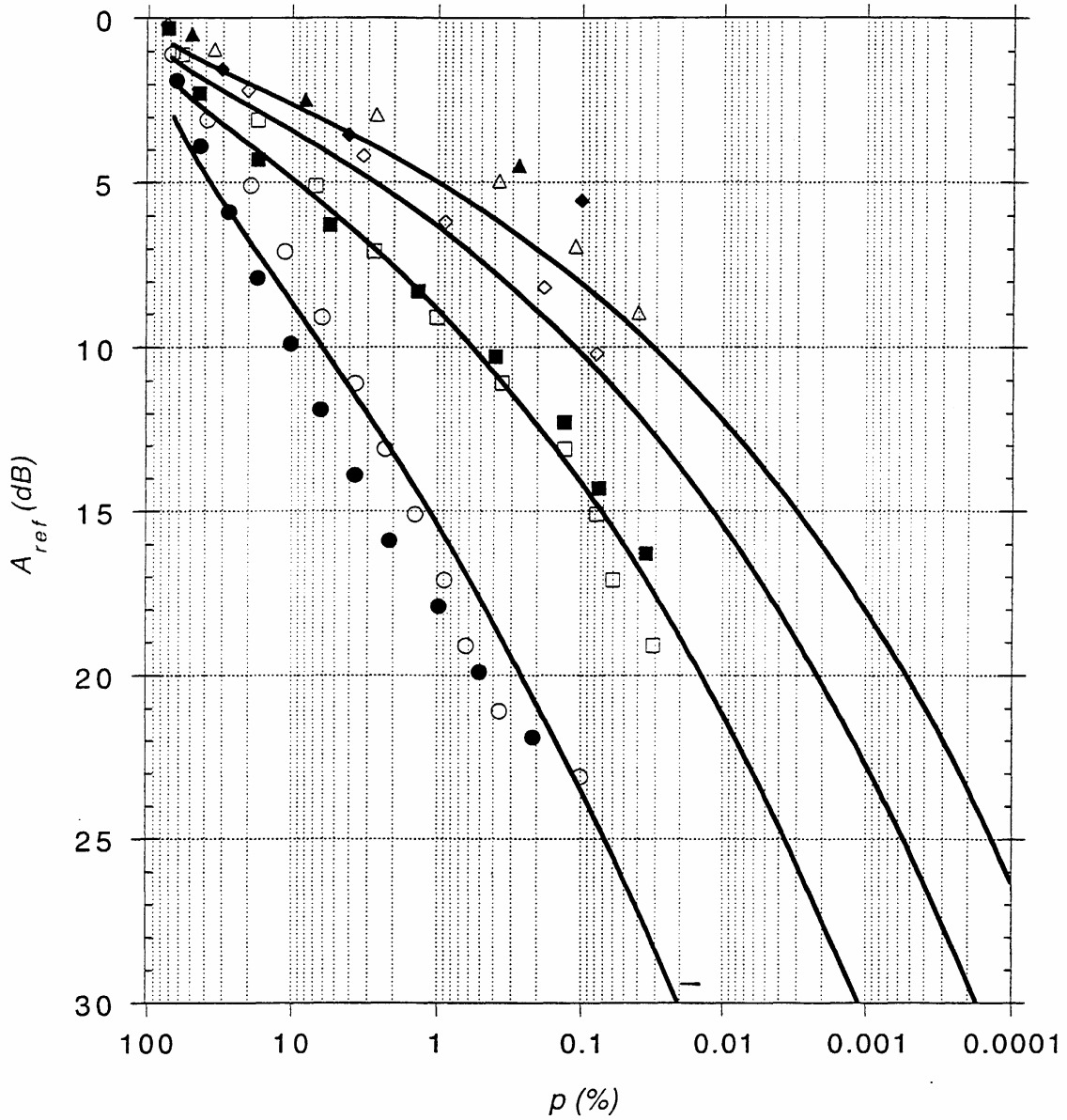


FIGURE 6.5

**Comparison of measured and predicted worst-month clear-air fading distributions for Alert**

Measured data for specified elevation angles: ○, ● 1.5°; □, ■ 2.5°; ◇, ◆ 3.5°; △, ▲ 4.5°. The open and filled data points represent different data sets at the designated angles.

———— Predicted distributions (based on  $p_L = 0.37\%$ , as determined by logarithmic extrapolation from Figure 9 of Recommendation ITU-R P.453).

The maximum monthly time percentage exceeded at every fade threshold defines the “worst-month” distribution for each elevation angle.

### 6.2.4.1.1 Beam spreading loss

Equation (23) of Recommendation ITU-R P.618 for the beam-spreading loss  $A_{bs}$  on low- and mid-latitude links is a regression fit to curve A of Figure 1 of Recommendation ITU-R P.834 at elevation angles of 1.5, 2.5, and 3.5° [Crane, 1971], and is considered typical of long-term median beam-spreading loss over inland continental locations. Data indicate that  $A_{bs}$  is much more severe at high latitudes in the warmer months of the year [Lam, 1987; Kurniawan, 1986]. Thus, the slope coefficient of Equation (24) of Recommendation ITU-R P.618 is based on a regression fit to the “worst-month” median fade depths for high-latitude locations, after subtracting the atmospheric attenuation estimated by the method of Recommendation ITU-R P.676.

### 6.2.4.1.2 Fading distribution

Equations (38) and (39) of Recommendation ITU-R P.618 are based on the assumptions, supported by model evaluations, that the deepest fading is due to multipath and that the fade distribution is approximately described by a model similar to that for terrestrial paths in Method 1 of Recommendation ITU-R P.530. The frequency terms in these equations are the same as those of Method 1 after rounding. Earth-space data at 4 and 30 GHz [Webber and McCormick, 1980] support the model, as do testing results based on data for frequencies ranging from 6 to 38 GHz. The path-length term in Method 1 was combined with a path-inclination expression to derive the elevation-angle terms in Equations (38) and (39).

The geoclimatic factor  $K_w$  for the average worst month given in Equation (33) of Recommendation ITU-R P.618 accounts for climate effects, particularly the varying occurrence of atmospheric layers with extreme refractivity gradients. Although  $K_w$  should in principle include the effects of both surface-based and elevated layers, the predictor variable  $p_L$  (applicable to the lowest 100 m of the atmosphere) yields good results in the method. Unlike the terrestrial case, a separate correction factor for large bodies of water was determined to be unnecessary for Earth-space paths. The empirical expression used in the method for the logarithmic geoclimatic factor  $G_a$  for the average year is based partly on terrestrial data and partly on Earth-space data. The shallow portion of the observed cumulative distributions is well-fitted with the same empirical shallow-fading relation used for terrestrial links.

Maps in Figures 7 to 10 of Recommendation ITU-R P.453 are used to determine the predictor variable  $p_L$  in Equation (33) of Recommendation ITU-R P.618. Tests of the model [Olsen, 1995] show that the most appropriate  $p_L$  values are found by logarithmic interpolation between map contours or, if  $p_L$  values are required for time percentages less than 1%, by logarithmic extrapolation based on the two nearest contours.

It may be desirable in some cases to obtain expansions of the maps in Recommendation ITU-R P.453 in the area of the link in question and precisely plot the point corresponding to the earth station location to obtain the  $p_L$  value. Since the maps are on a Mercator projection, the following relation should be employed to plot the site latitude  $\xi$ :

$$\Delta z_L = \Delta z \left[ \frac{\ln[\tan(45^\circ + 0.5\xi)] - \ln[\tan(45^\circ + 0.5\xi_1)]}{\ln[\tan(45^\circ + 0.5\xi_2)] - \ln[\tan(45^\circ + 0.5\xi_1)]} \right] \quad (6.2)$$

where  $\Delta z$  is the distance (e.g., in mm) between the nearest lower and upper latitude grid lines at latitudes  $\xi_1$  and  $\xi_2$ , respectively (e.g., 30° and 45°), and  $\Delta z_L$  is the required distance (e.g., in mm) between the lower latitude grid line and the point corresponding to the earth terminal. The site longitude can be found by linear interpolation.

#### 6.2.4.2 Characteristics of low-angle fading

The ITU-R prediction method provides cumulative fading statistics. Other characteristics of low-angle fading can be illustrated by reference to measured data. For example, in the measurements made at Isfjord at an elevation angle of  $3.2^\circ$ , the fading statistics were found to follow Nakagami-Rice distributions (see Recommendation ITU-R P.1057) with average values of power ratio of the random-to-steady component of -20 dB, -13 dB, and -10 dB for the best month, worst month, and worst day, respectively [Gutteberg, 1981].

Statistics of fade dynamics for 6 GHz data measured in Canada on a  $1^\circ$  path [Strickland *et al.*, 1977] indicated that 90% of the fades exceeding 20 dB lasted less than about 11 sec, and 90% of the fades exceeding 12 dB lasted less than about 35 sec. The rate-of-change of the signal level exceeded 1 dB/sec for 1% of the time, and 4 dB/sec for 0.1% of the time. Rate-of-change statistics are also available at frequencies of 4 and 30 GHz [Webber and McCormick, 1980] and 38 GHz [Lam, 1987]. (Analyses of fading dynamics depend critically on the data sampling and filtering techniques used, and comparisons of results should of course employ similar parameters.)

Space diversity may be beneficial in reducing the fade margins required for Earth-space links operating at very low elevation angles. Several diversity measurements have been performed. In the 6 GHz experiment cited above, good diversity improvement was obtained with a vertical terminal separation of 180 m, but results for horizontal spacing were inconclusive [Strickland *et al.*, 1977]. In a different measurement [McCormick and Maynard, 1972], good performance was achieved with a horizontal separation of 300 m, while in another [Strickland, 1981], the improvement was poor with a separation of 500 m. Site-diversity measurements conducted at an elevation angle of  $3.2^\circ$  at Isfjord [Gutteberg, 1983] showed a significant reduction in joint fading compared to single-path fading, but it was uncertain whether the improvement was due to the lateral spacing (1 150 m) between the two sites or to the relative height difference of the terminals as viewed from the satellite.

The diversity data for Eureka [Strickland, 1981] have been used to design an operational 6/4 GHz space-diversity system at that site. Measurements subsequently conducted over a period of almost 9 months to characterize system performance for these paths observed severe summertime refractive fading, and demonstrated the considerable decrease in path unavailable time that can be achieved with site diversity. Applications of site diversity for the refractive-fading case are similar in concept to those used to overcome rain fading (see § 3.3.1 of this handbook), but the scale is different because the relevant propagation mechanisms are different.

### 6.3 Propagation delays

Additional propagation delays superimposed on the delay due to free space propagation are produced by refraction through the troposphere, precipitation, and the ionosphere. Recommendation ITU-R P.834 provides a method for estimating the average propagation delay (and the variation in delay) due to the troposphere. At frequencies above 10 GHz, the ionospheric time delay is generally smaller than that for the troposphere; (see § 7.3.2).

Range determination to centimetre accuracy requires careful consideration of the various contributions to excess range delay. The water vapour contribution, which amounts to 10 cm for a zenith path and a reference atmosphere with  $7.5 \text{ g/m}^3$  surface water vapour concentration (2 km scale height), is found to be the largest source of uncertainty. This is true even though the dry atmosphere adds 2.3 m to the zenithal excess range delay [Flock *et al.*, 1982].

The mean and variance of the propagation delay in the precipitation-free atmosphere can be derived from the regression relation between surface refractivity and range error developed in the USA

[Bean and Dutton, 1966]. Details of the procedure, particularly that for estimating the delay error variance, are given elsewhere [Nuspl *et al.*, 1975].

Most published statistics of surface refractivity are given on a monthly basis, but estimates of the standard deviation for any time period  $T$  can be obtained by combining the one-month estimates with a semi-empirical frequency spectrum of the delay. Figure 6.6 shows curves of the standard deviation of delay along a two-way Earth-space path as a function of "cutoff frequency"  $f_c = 1/T$  and for one-month standard deviations of 10, 20 and 30  $N$ -units;  $f_c$  is the frequency below which the delay fluctuations are increasingly attenuated due to the finite observation period  $T$ . A typical path elevation angle of  $\theta = 30^\circ$  has been assumed, along with an effective path length of 10 km, and average wind speeds normal to the path of  $U = 2, 5, \text{ and } 10 \text{ m/s}$ . For elevation angles other than  $30^\circ$ , values obtained from the graph as well as the indicated wind speeds must be divided by the factor  $2 \sin \theta$ . The distribution of the delay fluctuations can be assumed to be Gaussian.

The curves in Figure 6.6 are based on an average frequency spectrum and do not reflect the distribution of extreme variations that can occur. An approximate upper limit for short observation periods  $T$  is given by  $\sigma_{\Delta\tau} \approx 0.25/\sin \theta \text{ (ns)}$  for  $\theta \geq 10^\circ$ .

The change in delay due to a rain cell crossing the propagation path can be estimated using an approach similar to that used to calculate attenuation [Nuspl *et al.*, 1975] in the range up to about 15 GHz. Since the delay variation is around 0.2 nsec, the delay variation due to rain can be ignored in general.

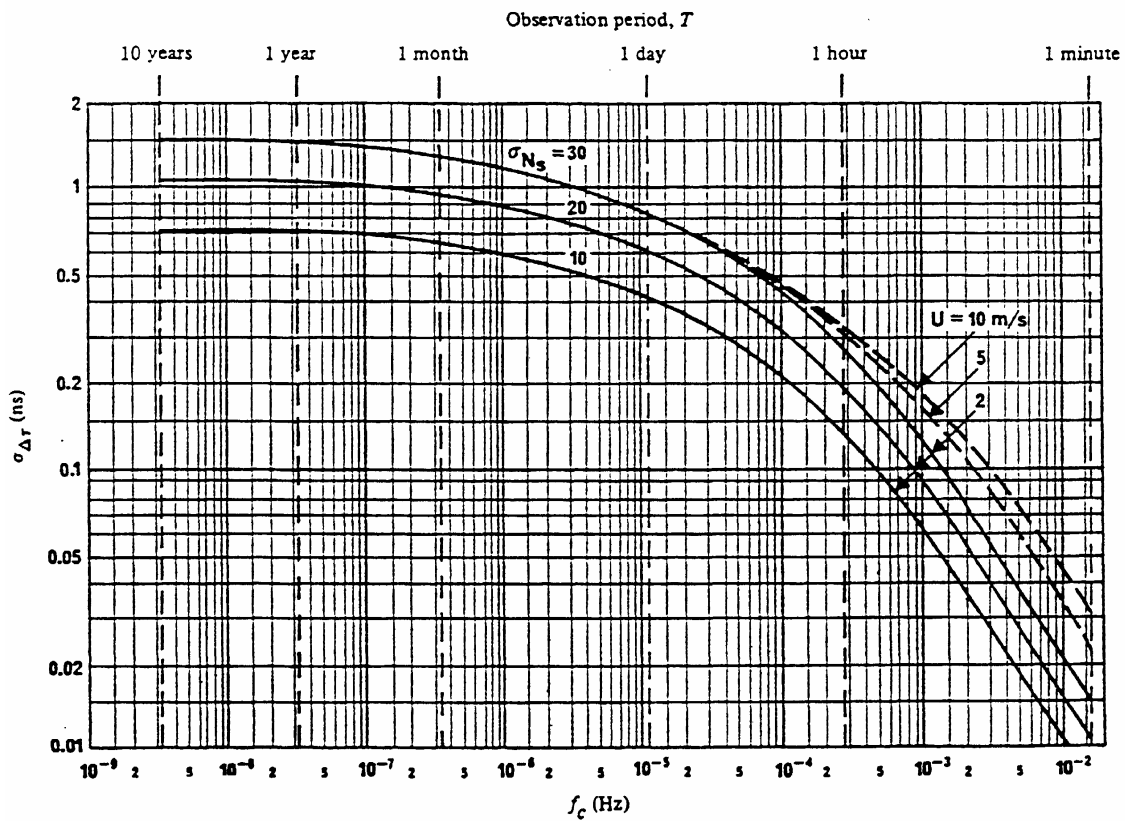


FIGURE 6.6

**Cumulative frequency dependence of the standard deviation of delay  $\sigma_{\Delta\tau}$  for a two-way Earth-space path at  $30^\circ$  elevation. Each curve corresponds to the specified values of standard deviation  $\sigma_{N_s}$  for a one-month period.**

## 6.4 Angle of arrival

The gradient of the refractive index of the atmosphere causes a bending of the radio ray, and therefore the angle of arrival varies from that calculated based on the geometry of the path. Since the refractive index varies largely with altitude, the angle-of-arrival variation is much greater in elevation than in azimuth. In addition, turbulent irregularities of the refractive index can give rise to angle-of-arrival scintillations. Both these effects decrease markedly with elevation angle, and are generally insignificant for elevation angles above  $10^\circ$ . The effects are independent of frequency.

Published information concerning measurements of angle-of-arrival variation is not extensive. Recommendation ITU-R P.618 (§ 7) gives typical values of the angle-of-arrival variation due to refraction and the short-term fluctuations due to turbulence. The physical causes are discussed in more detail in Recommendation ITU-R P.834 and in Chapter 4 of the ITU-R Handbook on Radiometeorology. A statistical analysis of short-term variations is given in [Fukuchi *et al.*, 1988].

For very low elevation angles, under certain meteorological conditions, it may be necessary to account for ducting. Recommendation ITU-R P.834 and the ITU-R Handbook on Radiometeorology provide prediction models and background information.

REFERENCES FOR CHAPTER 6

- BANJO, O.P. and VILAR, E. [1986] Measurement and modeling of amplitude scintillations on low-elevation Earth-space paths and impact on communication systems, *IEEE Trans. Commun.*, Vol. COM-34, 8, 774-780.
- BEAN, B.R. and DUTTON, E.J. [1966] *Radio Meteorology*, Dover Publications, New York, USA.
- BRYANT, D.L. [1992] Low elevation angle 11 GHz beacon measurements at Goonhilly Earth station. *BT Technol. J.*, vol. 10, pp. 68-75.
- COX, D.C. [1981] Depolarization of radio waves by atmospheric hydrometeors on Earth-space paths: A review, *Radio Sci.*, Vol. 16, 5, 781-812.
- CRANE, R.K. [1971] Propagation phenomena affecting satellite communication systems operating in centimetre and millimetre wavelength bands, *Proc. IEEE*, Vol. 59, 173-188.
- CRANE, R.K. [1976] Low elevation angle measurement limitations imposed by the troposphere: An analysis of scintillation observations made at Haystack and Millstone, MIT Lincoln Lab. Tech. Rep. 518, Lexington MA.
- FLOCK, W.L., SLOBIN, S.D. and SMITH, E.K. [1982] Propagation effects on radio range and noise in Earth-space telecommunications, *Radio Sci.* Vol. 17, 6, 1411-1427.
- FUKUCHI, H., NAKAMURA, K., OKAMOTO, K. and OKUYAMA, T. [1988] Angle-of-arrival fluctuation at 20 GHz on Earth-space path, *Journal of Electromagnetic Waves and Applications*, vol. 2, 671-681.
- GUTTEBERG, O. [1981] Measurement of tropospheric fading and cross-polarization in the arctic using Orbital Test Satellite, IEE Conf. Publ. No. 195, Part 2, 71-75. *IEE Second Int. Conf. Antennas Propagat.*, Heslington, York, UK.
- GUTTEBERG, O. [1983] Low elevation propagation in high-latitude regions. Final Report, ESTEC Contract no 5032/82 NL GM(SC), Norwegian Telecom, Kjeller, Norway, April.
- HADDON, J. and VILAR, E. [1986] Scattering induced scintillations from clear air and rain on Earth space paths and the influence of antenna aperture, *IEEE Trans. Antennas Propagat.*, Vol. AP-34, 8, 646-657.
- ISHIMARU, A. [1978] *Wave propagation and scattering in random media*, New York: Academic Press.
- KARASAWA, Y., YASUKAWA, K. and YAMADA, M. [1988a] Tropospheric scintillation in the 14/11 GHz bands on Earth-space paths with low elevation angles, *IEEE Trans. Antennas Propagat.*, Vol. AP-36, 4, 563-569.
- KARASAWA, Y., YAMADA, M. and ALLNUTT, J.E. [1988b] A new prediction method for tropospheric scintillation on Earth-space paths, *IEEE Trans. Antennas Propagat.*, Vol. AP-36, 11, 1608-1614.
- KURNIAWAN, Z. [1986] Satellite link performance monitoring - Project Hurricane. Final Report, Telesat Canada, January.
- LAM, W.I. [1987] Low angle signal fading at 38 GHz in the high arctic. *IEEE Trans. Antennas Propagat.*, vol. 35, pp. 1495-1499.

- LO, P., BANJO, O.P. and VILAR, E. [1984] Observation of amplitude scintillations on a low elevation Earth-space path, *Electron. Lett.*, Vol. 20, 7.
- McCORMICK, K.S. and MAYNARD, L.A. [1972] Measurements of SHF tropospheric fading along Earth-space paths at low elevation angles, *Electron. Lett.*, Vol. 8, 10, 274-276.
- NUSPL, P.P., DAVIES, N.G. and OLSEN, R.L. [1975] Ranging and synchronization accuracies in a regional TDMA experiment, *Proc Third Int. Digit. Sat. Comm. Conf.*, Kyoto, Japan.
- OLSEN, R. [1995] Summary of worldwide procedures for the prediction of clear-air fading distributions on very-low-angle satellite links. *Symp. Proc.*, URSI Open Symp. on Wave Propagation and Remote Sensing, Ahmedabad, India, 20-24 November.
- OLSEN, R. and TJELTA, T. [1996] World-wide techniques for predicting the multipath fading distribution on terrestrial LOS links: Background and results of tests. (To be published in *IEEE Trans. Antennas Propagat.*, 1997).
- ORTGIES, G. [1989] Ein modell zur Beschreibung von Mikrowellenszintillationen mit Hilfe meteorologischer Parameter, *Kleinheubacherberichte* Vol. 32, 309-315.
- ORTGIES, G. and RÜCKER, F. [1992] Frequency-scaling of slant-path amplitude scintillations, *Proc URSI Comm. F Open Symposium*, Ravenscars (UK), 7.8.1-7.8.5.
- RÜCKER, F. and ORTGIES, G. [1985] Diurnal and seasonal variations of OTS amplitude scintillations, *Electron. Lett.*, Vol. 21, 4, 143-145.
- STRICKLAND, J.I. [1981] Site diversity measurements of low-angle fading and comparison with a theoretical model, *Ann. des Telecomm.*, Vol. 36, 7-8, 457-463.
- STRICKLAND, J.I, OLSEN, R.O. and WERSTIUK, H.L. [1977] Measurements of low angle fading in the Canadian Arctic, *Ann. des Telecomm.*, 11-12, 530-535.
- TATARSKII, V.I. [1961] *Wave propagation in a turbulent medium* (translated by R.A. Silverman), New York, McGraw-Hill.
- THOMPSON, M.C., WOOD, L.E., LAMES, H.B. and SMITH, D. [1975] Phase and amplitude scintillation in the 10 to 40 GHz band, *IEEE Trans. Antennas Propagat.*, Vol. AP-23, 6, 792-797.
- VANDER VORST, A. VANHOENACKER, D. and MERCIER, L. [1982] Fluctuations on OTS-Earth co-polar link against diurnal and seasonal variations, *Electron. Lett.*, Vol. 18, 21, 915-917.
- WEBBER, R.V. and McCORMICK, K.S. [1980] Low angle measurements of the ATS-6 beacons at 4 and 30 GHz, *Ann. des Telecomm.*, Vol. 35, 11-12, 494-500.
- YAMADA, M. and YOKOI, H. [1974] Flux density of celestial radio sources at 15.5 31.6 GHz, *Electron. Comm. Japan*, Vol. 57-B, 3, 79-85.
- YOKOI, H., YAMADA, M. and SATOH, T. [1970] Atmospheric attenuation and scintillation of microwaves from outer space, *Publ. Astronom. Soc. Japan*, 22, 511-524.

## CHAPTER 7

### TRANSIONOSPHERIC PROPAGATION

#### 7.1 Introduction

Radiowaves at frequencies at VHF and above are capable of penetrating the ionosphere, and therefore provide transionospheric communications. For transionospheric communications, the most significant degradations due to background ionization include Faraday Rotation and Group Delay. These degradations are all related to the Total Electron Content (TEC) along the propagation path. On the other hand, the leading degradation due to irregularities is a phenomenon commonly called scintillation. These will be the main subject matter of this chapter.

#### 7.2 Total Electron Content (TEC)

Denoted as  $N_T$ , the total electron content (TEC) can be evaluated by

$$N_T = \int_s N_e(s) ds \quad \text{electrons/m}^2 \quad (7.1)$$

where  $N_e$  is the electron density (in  $\text{m}^{-3}$ ) along the path and  $s$  is the propagation path in metres. Typically  $N_T$  varies from 1 to 200 TEC units (1 TEC unit =  $10^{16}$  electrons/ $\text{m}^2$ ). Even when the precise propagation path is known, the evaluation of  $N_T$  is difficult because  $N_e$  is highly variable in space and time [Davies, 1980; Soicher and Gorman, 1985].

For modelling purposes, the TEC value is usually quoted for a vertical path using the relationship  $N_e(s) ds = N_e(h) \sec \phi dh$ , where  $\phi$  is the zenith angle of the ray at a mean ionospheric height ( $\sim 400$  km). From a knowledge of the TEC, Faraday rotation and group delay can be estimated for communications applications. The estimate is provided below.

#### 7.3 Effects due to background ionization

##### 7.3.1 Faraday rotation

When propagating through the ionosphere, a linearly polarized wave will suffer a gradual rotation of its plane of polarization due to the presence of the geomagnetic field and the anisotropy of the plasma medium. The magnitude of Faraday rotation,  $\Omega$ , will depend on the frequency of the radiowave, the geomagnetic field strength, and the electron density of the plasma as:

$$\Omega = \frac{KM}{f^2} N_T \quad (7.2)$$

where  $K = 2.36 \times 10^4$  (in MKS units),  $\Omega$  is in radians,  $M$  is the value of  $B_L \sec \phi$  at 420 km of height,  $B_L$  the longitudinal component of the Earth's magnetic induction, in Tesla, along the ray path,  $\phi$  is the zenith angle of the ray, and  $f$  is the frequency in Hertz. Typical values of  $\Omega$  as a function of frequency for representative TEC values are shown in Figure 7.1.

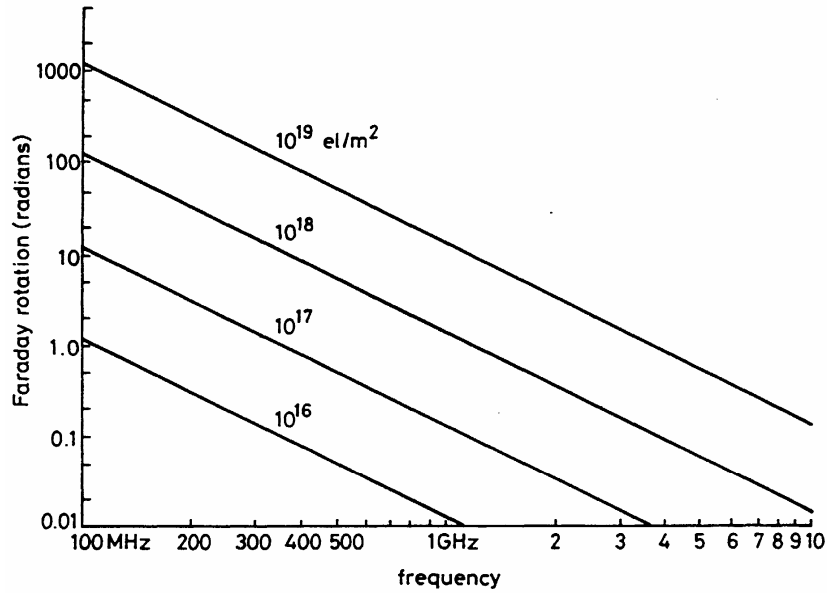


FIGURE 7.1

**Faraday rotation as a function of TEC and frequency**

Table 7.1 gives the Faraday rotation in degrees which would be exceeded for the stated percentages of time, at a frequency of 1 GHz, during a complete year of observation, at both sunspot maximum ( $R_{12} = 157$ ) and minimum periods ( $R_{12} = 42$ ).

TABLE 7.1

**Faraday rotation at 1 GHz exceeded for given percentages of time**

Time percentage	99	90	50	10	1	0.1	0.01	Period	R <sub>12</sub>
Rotation (degrees)	3	7	23	43	64	75	82	1979-80	157
	1	2	7	14	30	41	47	1977-78	42

**7.3.2 Group delay**

The presence of charged particles in the ionosphere slows down the propagation of radio signals along the path and produces a phase advance. The time delay in excess of the propagation time in free space, commonly denoted as  $\Delta\tau_g$ , is called the group delay. It is an important factor to be considered for digital communication systems and navigational positioning systems. This quantity is given by:

$$\Delta\tau_g = 1.34 \times 10^{-7} N_T / f^2 \tag{7.3}$$

where

$\Delta\tau_g$  = delay time in seconds with reference to propagation in a vacuum

$f$  = frequency in Hz

$N_T$  = TEC in electrons/m<sup>2</sup>

Figure 7.2 is a plot of time delay  $\Delta\tau_g$  versus frequency  $f$  for several values of electron content along the ray path.

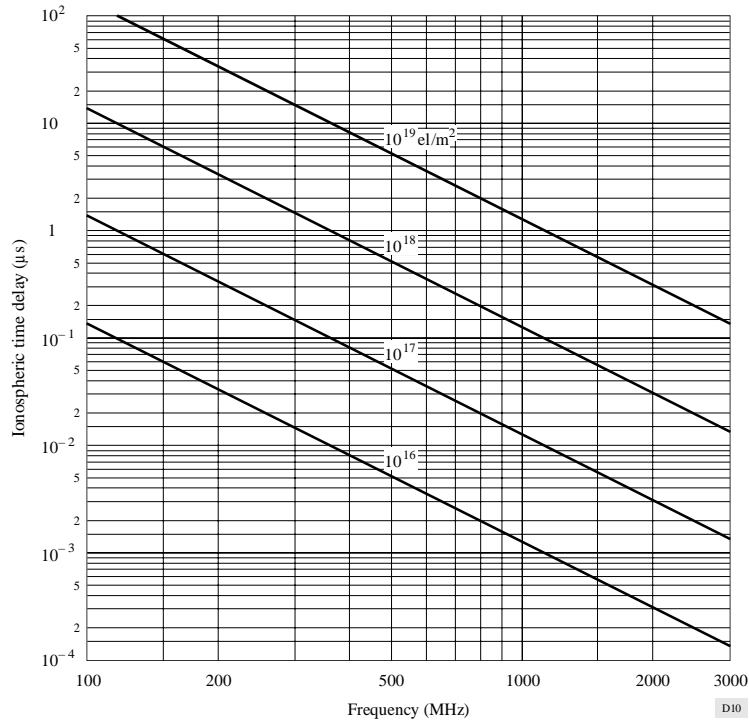


FIGURE 7.2

**Ionospheric time delays versus frequency for various values of electron content**

Figure 7.3 shows the yearly percentage of daytime hours that the time delay will exceed 20 ns at a period of relatively high solar activity using a total electron content model developed by Bent *et al.* [1981].

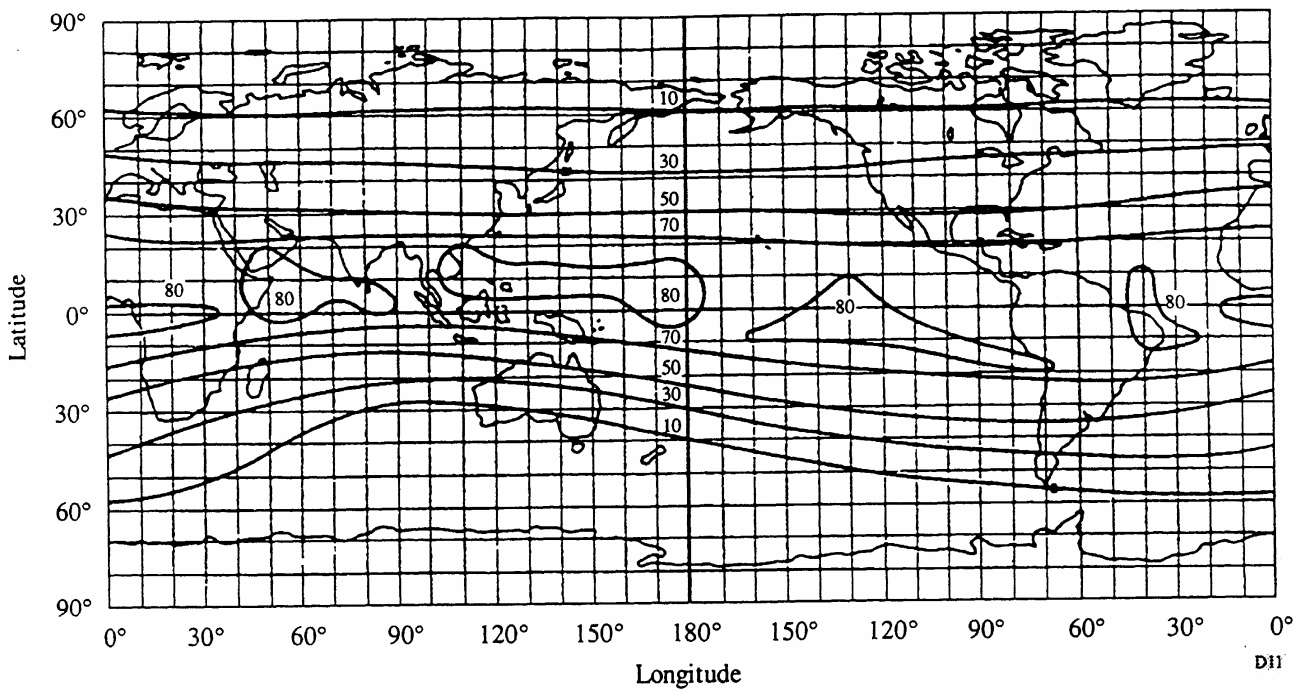


FIGURE 7.3

**Contours of percentage of yearly average day-time hours when time delay at vertical incidence at 1.6 GHz exceeds 20 ns (sunspot number = 140)**

### 7.3.3 Dispersion

When trans-ionospheric signals occupy a significant bandwidth the propagation delay (being a function of frequency) introduces dispersion. The differential delay across the bandwidth is proportional to the integrated electron density along the ray path. For example, for an integrated electron content of  $5 \times 10^{17}$  electron/m<sup>2</sup>, a signal with a pulse length of 1  $\mu$ s will sustain a differential delay of 0.02  $\mu$ s at 200 MHz while at 600 MHz the delay would be only 0.00074  $\mu$ s (see Figure 7.4) [Millman and Olsen, 1980; Mawira, 1990].

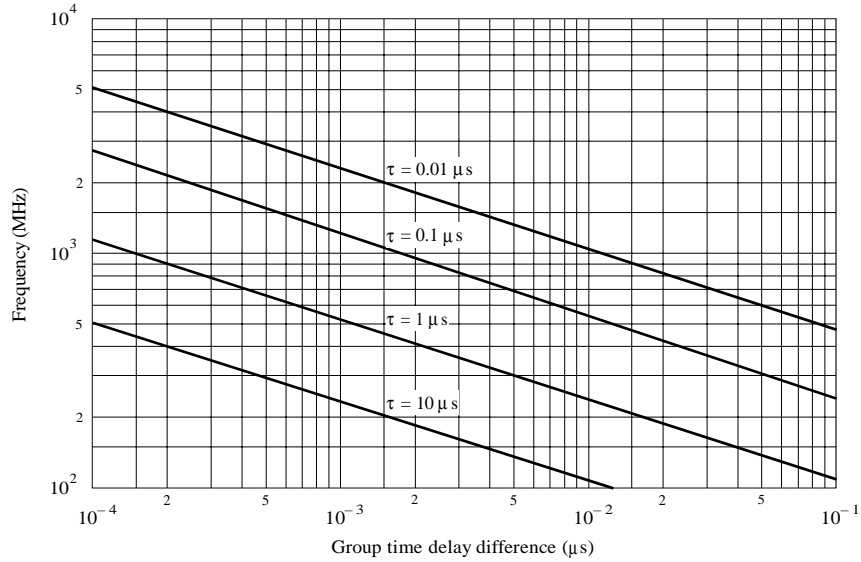


FIGURE 7.4

**Difference in the time delay between the lower and upper frequencies of the spectrum of a pulse of width  $\tau$ , transmitted through the ionosphere, one-way traversal**

### 7.3.4 Doppler frequency shift

The effect of frequency change due to the temporal variability of the ionosphere upon the apparent frequency of the carrier, or the Doppler shifted carrier, is a second order effect. For example, at  $f = 1.6$  GHz (GPS system), the observed frequency change  $\Delta f$  at high latitudes is:

$$\frac{\Delta f}{f} < 10^{-9} \quad (7.4)$$

### 7.3.5 Direction of arrival of the ray

When radiowaves propagate obliquely through the ionosphere, they undergo refraction which produces a change in the direction of arrival of the ray.

### 7.3.6 Absorption

When direct information is not available, ionospheric absorption loss can be estimated from available models according to the  $(\sec \phi)/f^2$  relationship, for frequencies above 30 MHz where  $\phi$  is the zenith angle of the propagation path in the ionosphere [Davies, 1990]. For equatorial and mid-latitude regions, radiowaves of frequencies above 70 MHz will assure penetration of the ionosphere without significant absorption.

Measurements at middle latitudes indicate that, for a one-way traverse of the ionosphere at vertical incidence, the absorption at 30 MHz under normal conditions is typically 0.2 to 0.5 dB. During a solar flare, the absorption will increase but will be less than 5 dB. Enhanced absorption can occur at high latitudes due to polar cap and auroral events; these two phenomena occur at random intervals, last for different periods of time, and their effects are functions of the locations of the terminals and the elevation angle of the path. Therefore for the most effective system design these phenomena should be treated statistically bearing in mind that the durations for auroral absorption are of the order of hours and for polar cap absorption are of the order of days.

#### 7.3.6.1 Auroral absorption

Auroral absorption results from increases of electron concentration in the D and E regions produced by incident energetic electrons. The absorption is observed over a range of  $10^\circ$  to  $20^\circ$  latitude centred close to the latitude of maximum occurrence of visual aurorae. It occurs as a series of discrete absorption enhancements each of relatively short duration, i.e., from minutes up to a few hours, with an average duration of about 30 minutes, and usually showing an irregular time structure [Hargreaves and Cowley, 1967]. Night enhancements tend to consist of smooth fast rises and slow decays. Typical magnitudes at 127 MHz are shown in Table 7.2.

TABLE 7.2

**Auroral absorption at 127 MHz (dB)**

Percentage of the time	Angle of elevation	
	$20^\circ$	$5^\circ$
0.1	1.5	2.9
1	0.9	1.7
2	0.7	1.4
5	0.6	1.1
50	0.2	0.4

#### 7.3.6.2 Polar cap absorption

Polar cap absorption occurs on relatively rare occasions at geomagnetic latitudes greater than  $64^\circ$  [Bailey, 1964]. The absorption is produced by ionization at heights greater than about 30 km. It usually occurs in discrete, though sometimes overlapping, events which are nearly always associated with discrete solar events. The absorption is long-lasting and is detectable over the sunlit polar caps. Polar cap absorption occurs most usually during the peak of the sunspot cycle, when there may be 10 to 12 events per year. Such an event may last up to a few days. This is in contrast to auroral absorption, which is frequently quite localized, with variations in periods of minutes.

A remarkable feature of polar cap absorption event is the great reduction in the absorption during hours of darkness for a given rate of electron production.

## 7.4 Effects due to ionization irregularities

### 7.4.1 Scintillation effects

One of the most severe disruptions along a transionospheric propagation path for signals from VHF to C-band is caused by ionospheric scintillation. Principally through the mechanisms of forward scattering and diffraction, small-scale irregular structures in the ionization density produce the scintillation phenomenon in which the steady signal at the receiver is replaced by one which is fluctuating in amplitude, phase, and apparent direction of arrival. Depending on the modulation scheme of the system, various aspects of scintillation affect the system performance differently [Yeh and Liu, 1982]. The most commonly used parameter characterizing the intensity fluctuations is the scintillation index  $S_4$ , defined by:

$$S_4 = \left( \frac{\langle I^2 \rangle - \langle I \rangle^2}{\langle I \rangle^2} \right)^{1/2} \quad (7.5)$$

where  $I$  is the intensity of the signal and  $\langle \rangle$  denotes time averaging [Briggs and Parkin, 1963].

The scintillation index  $S_4$  is related to the peak-to-peak fluctuations of the intensity. The exact relation depends on the distribution of the intensity. The intensity distribution is best described by the Nakagami distribution [Fang and Liu, 1987] for a wide range of  $S_4$  values. As  $S_4 \rightarrow 1.0$ , it approaches the Rayleigh distribution. Occasionally,  $S_4$  may exceed 1, reaching values as high as 1.5. This is due to focusing. For values less than 0.6,  $S_4$  shows a consistent  $f^{-1.5}$  frequency dependence for most multifrequency observations in the VHF and UHF bands. Recent equatorial observations at gigahertz frequencies, however, suggested values higher than 1.5 for the spectral index. As the scintillation becomes stronger such that  $S_4$  exceeds 0.6, the spectral index decreases. This is due to the saturation of scintillation for Rayleigh fading under the strong influence of multiple scattering.

Empirically, Table 7.3 provides a convenient conversion between  $S_4$  and the approximate peak-to-peak fluctuations  $P_{fluc}$  in decibels [Fang and Liu, 1987].

TABLE 7.3

**Empirical conversion table for scintillation indices**

$S_4$	$P_{fluc}$
0.1	1.5
0.2	3.5
0.3	6
0.4	8.5
0.5	11
0.6	14
0.7	17
0.8	20
0.9	24
1.0	27.5

### 7.4.2 Geographic, seasonal and solar dependence

Geographically, there are two intense zones of scintillations, one at high latitudes [Hoppe *et al.*, 1991] and the other centred within  $\pm 20^\circ$  of the magnetic equator as shown in Figure 7.5. Severe scintillations have been observed up to gigahertz frequencies in these two sectors, being most pronounced in the equatorial sector, while in the middle latitudes scintillations mainly affect VHF signals [Basu *et al.*, 1988]. In all sectors there is a pronounced night-time maximum of the activity [Aarons, 1982, 1993].

At polar latitudes and at equatorial latitudes, the most dramatic changes occur over a sunspot cycle with a sunspot maximum producing strong effects in the anomaly region of the equator ( $12 - 15^\circ$  from the magnetic equator as shown in Figure 7.5) and in the polar region. In the auroral region, magnetic storms play the dominant role in producing scintillations during any part of the sunspot cycle. During low sunspot years, the polar region and the anomaly region have, for the most part, low fading levels. For equatorial scintillation from 1.5 to 4 GHz, peak activity is as shown in Figure 7.6 [Aarons, 1993]. Peak-to-peak fluctuations at the magnetic equator are of the order of 5 - 6 dB in both high and low sunspot years for 1.5 GHz. At anomaly latitudes, peak-to-peak fluctuations can be over 20 dB for many hours during years of sunspot maximum. At 4 GHz the peak-to-peak fluctuations of RF signal level exceed 10 dB in magnitude.

In terms of temporal characteristics, the fading rate of ionospheric scintillation is about 0.1 Hz to 1 Hz. A scintillation event has typically an onset after local ionospheric sunset and can last from 30 minutes to hours. For an equatorial station at years of solar maximum, ionospheric scintillation occurs almost every evening after sunset.

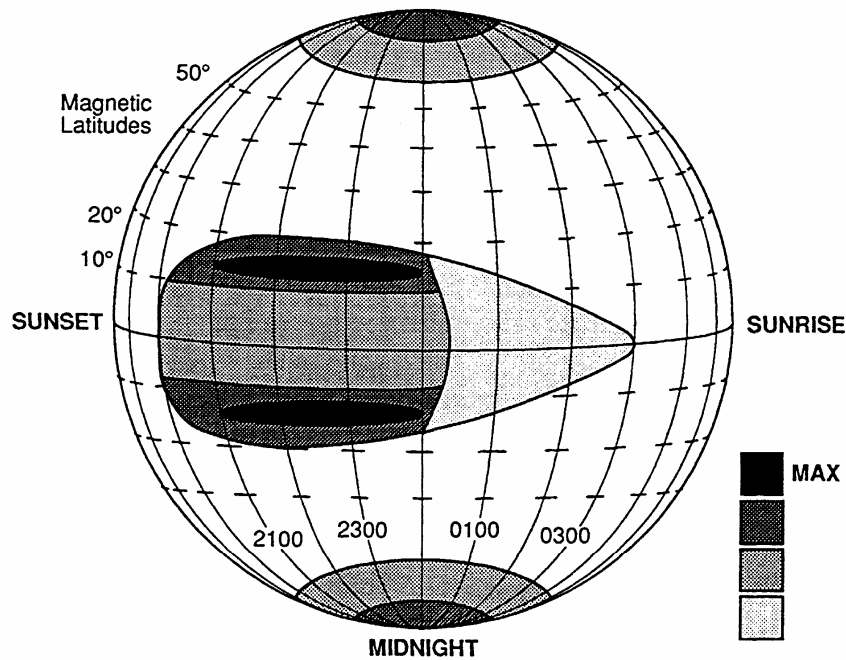


FIGURE 7.5

**Illustrative picture of fading depths during high sunspot years**

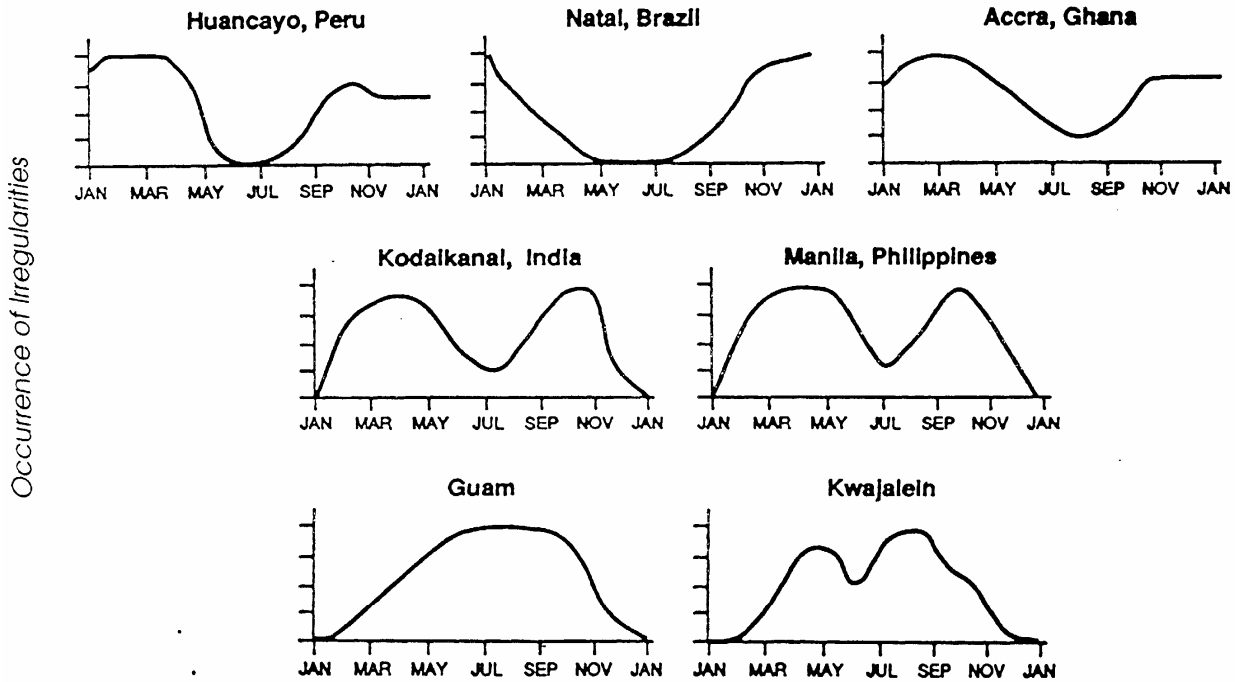
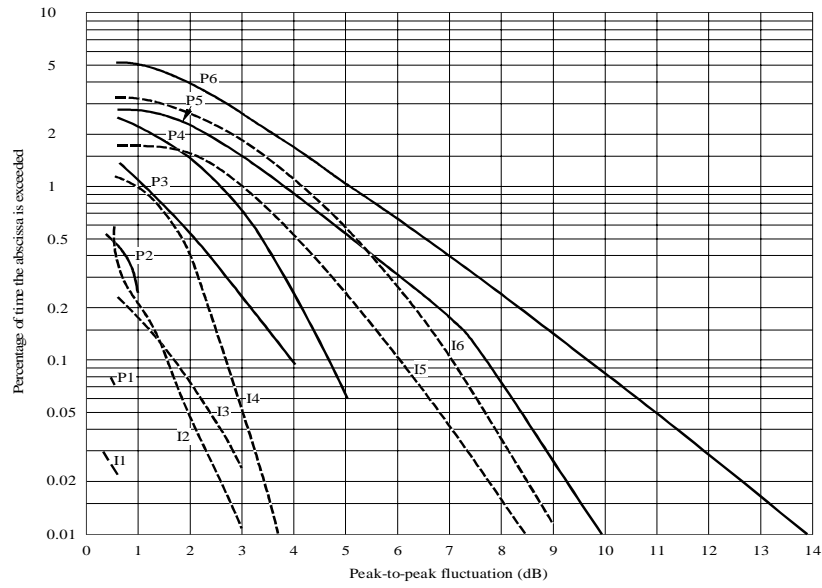


FIGURE 7.6

**Occurrence pattern of 1.5 GHz scintillation at the magnetic equator**

**7.4.3 Scintillation models**

To model the scintillation phenomenon one needs to understand the physical mechanisms that generate these irregularities [Goodman and Aarons, 1990]. Current knowledge about these irregularities, however, does not provide sufficient basis for the construction of a comprehensive model. It has been suggested that spread-F irregularities are responsible for scintillations. Spread-F irregularities are essentially evening and night-time events in the F region. Depending on latitudinal locations, the occurrence of spread-F has distinctive patterns relating to seasonal variations and magnetic activities. Since spread-F has been studied continuously from the early 1930s and enormous amounts of data are available, radio physicists have attempted to devise empirical models for predicting scintillations based on spread-F models. A more recent model has been constructed based on numerous satellite propagation observations, particularly on observations performed in the DNA Wideband Satellite Experiment [Secan *et al.*, 1996]. With these inputs, models incorporate geographical, seasonal, diurnal, and solar activity as well as magnetic activity dependence. These models have been shown to be successful in predicting UHF scintillations. The most essential element of these models is provided below.



*P* curves refer to a 20° elevation angle pointing to an eastward synchronous satellite while *I* curves refer to a 30° elevation angle pointing to a westward synchronous satellite.

Curve	Period	SSN range
I1,P1	March 75-76	10-15
I2,P2	June 76-77	12-26
I3,P3	March 77-78	20-70
I4,P4	October 77-78	44-110
I5,P5	November 78-79	110-160
I6,P6	June 79-80	153-165

FIGURE 7.7

**Annual statistics of 4 GHz ionospheric scintillation observed at Hong Kong Earth station (Curves I1, P1, I3-I6, P3-P6) and Taipei Earth station (Curves P2 and I2)**

Available long-term observational data forms the basis for establishing these models. A typical example for an equatorial ionospheric path at 4 GHz is shown in Figure 7.7 [Fang and Pontes, 1981]. The annual occurrence statistics of peak-to-peak amplitude fluctuations,  $P_{fluc}$  in decibels, are given for two links. Curves for different years when sunspot numbers (SSN) change from 10 to 165 are labelled. For link budget calculation,  $P_{fluc}$  is related to signal level loss  $L_p$  by:

$$L_p = \frac{1}{\sqrt{2}} P_{fluc} \quad (7.6)$$

## 7.5 Conclusion

To summarize, Table 7.4 estimates maximum values for ionospheric effects at a frequency of 1 GHz. It is assumed that the total zenith electron content of the ionosphere is  $10^{18}$  electrons/m<sup>2</sup> column. An elevation angle of about 30° is also assumed. The values given are for the one-way traversal of the waves through the ionosphere.

TABLE 7.4  
**Estimated maximum ionospheric effects at 1 GHz for  
 elevation angles of about 30° one-way traversal**

Effect	Magnitude	Frequency dependence
Faraday rotation	108°	$1/f^2$
Propagation delay	0.25 μs	$1/f^2$
Refraction	< 0.17 milliradians	$1/f^2$
Variation in the direction of arrival	0.2 min of arc	$1/f^2$
Absorption (polar cap absorption)	0.04 dB	$-1/f^2$
Absorption (auroral + polar cap absorption)	0.05 dB	$-1/f^2$
Absorption (mid-latitude)	< 0.01 dB	$1/f^2$
Dispersion	0-4 ns/MHz	$1/f^3$
Scintillation	See § 7.4	See § 7.4

As communications and computer techniques rapidly advance, the conventional approach of singling out propagation degradation as the physical effects, such as Faraday rotation, group delay and scintillations, is no longer adequate. Wave propagation in the ionosphere is a complicated phenomenon and manifests itself differently for different types of systems. For instance, fading level is a prime concern to a low-margin communications system in determining the link availability; excess time delay is a prime concern to a navigation system in determining the range and location; depolarization is a concern to a remote-sensing system which uses dual polarization returns to identify the target; nonstationary property is a prime concern to a tracking/surveillance system which has a requirement of setting proper dwell time when sweeping through the space; and common volume scattering is a prime concern to a jamming/anti-jamming system which has to be able to control the level of wanted to unwanted interference. Consequently, propagation can only be adequately addressed with a proper reference to the communications and computer technology of the system to be used.

REFERENCES FOR CHAPTER 7

- AARONS, J. [1982] Global Morphology of ionospheric scintillations, *Proc. IEEE*, Vol. 70, 360-378.
- AARONS, J. [1993] The longitudinal morphology of equatorial F-layer irregularities relevant to their occurrence, *Space Science Reviews*, Vol. 63, 209-243.
- BAILEY, D.K. [1964] Polar cap absorption. *Planet and Space Sci.*, Vol. 12, 495-541.
- BASU, S. , MACKENZIE, E. and BASU, S. [1988] Ionospheric constraints on VHF/UHF communications links during solar maximum and minimum periods, *Radio Sci.*, Vol. 23, 363-378.
- BENT, R.B. *et al.* [1981] The development of a highly-successful worldwide empirical ionospheric model and its use in certain aspects of space communications and worldwide total content investigation, *Effects of the Ionosphere on Space Systems and Communications*, ed. by T.M. Goodman, Naval Research Lab., Washington, D.C. 20375, United States Government Printing Office Stock No. 008-051-00064-0.
- BRIGGS, B.H. and PARKIN, I.A. [1963] On the variation of radio star and satellite scintillations with zenith angle. *J. Atmos Terr Phys.*, Vol. 25, 334-365.
- DAVIES, K. [1980] Recent progress in satellite radio beacon studies with particular emphasis on the ATS-6 radio beacon experiment, *Space Science Review*, 25, 357-430.
- DAVIES, K. [1990] *Ionospheric Radio*. IEE Electromagnetic Waves Series 31, Peter Peregrinus Ltd.
- FANG, D.J. and LIU, C.H. [1987] Propagation, Chapter 29, in *Antenna Handbook*, Y.T. Lo and S.W. Lee, editors, Van Nostrand Reinhold, New York.
- FANG, D.J. and PONTES, M.S. [1981] 4/6 GHz ionospheric scintillation measurements during the peak of sunspot cycle 21. *COMSAT Tech. Rev.*, Vol. 11, 2, 293-320.
- GOODMAN, J.M. and AARONS, J. [1990] Ionospheric effects on a modern electronic system, *Proc. IEEE* Vol. 78, 512-528.
- HARGREAVES, J.K. and COWLEY, F.C. [1967] Studies of auroral space absorption at three magnetic latitudes. *Planet and Space Sci.*, Vol 15, 1571-1585.
- HOPPE, U.-P., OFSTAD, A.E. and VAN EYKEN, A.P. [1991] Scintillations in trans-ionospheric radio signals: studying their cause with EISCAT and the NAVSTAR GPS satellites, *1991 Nordic Society for Space Research Conference Proceedings*, Danish Meteorological Institute Scientific Report 93-1, 123.
- MAWIRA, A. [1990] Slant path 30 to 12.5 GHz copolar phase difference, first results from measurements using the OLYMPUS satellite, *Electronics Letters*, Vol. 26, 15, 1138-1139.
- MILLMAN, G.H. and OLSEN, K.A. [1980] Ionospheric dispersion effects on wideband transmissions, *AGARD Conf Proc* No 284, Propagation Effects in Space/Earth Paths, 26-1 to 26-12.

- SECAN, J.A., BUSSEY, R.M., FREMOUW, E.J. and BASU, S. [1996] High-latitude upgrade to the WBMOD ionospheric scintillation model, *Proc. Ionospheric Effects Symposium*, 7-9 May.
- SOICHER, H. and GORMAN, F.J. [1985] Seasonal and day-to-day variability of total electron content at mid-latitudes near solar maximum, *Radio Science*, vol 20, 383-387.
- YEH, K.C. and LIU, C.H. [1982] Radiowave scintillations in the ionosphere, *Proc. IEEE*, Vol. 70, 324-360.

## CHAPTER 8

### **SURFACE REFLECTIONS AND LOCAL ENVIRONMENTAL EFFECTS (OF PARTICULAR INTEREST TO MOBILE-SATELLITE SYSTEMS)**

#### **8.1 Introduction**

Surface reflections and local environmental effects are important considerations for earth terminals employing wide beamwidth antennas, such as the communication terminals typically used in the mobile-satellite communication services. Such effects generally tend to impair the performance of a communications link, although signal enhancements are also occasionally observed.

Surface reflections are generated either in the immediate vicinity of the terminal or from distant reflectors such as mountains and large man-made structures. The reflected signals can interfere with the direct signal from the satellite to produce unacceptable levels of signal degradation. In addition to fading, signal degradations include inter-symbol interference arising from delayed replicas.

Local environmental effects include shadowing and blockage from objects and vegetation nearby the earth terminal. Another factor that affects communication links is radio-frequency emissions from noise sources in the local environment. These sources include broadband noise sources such as electrical equipment and motor vehicles, and out-of-band emissions from powerful transmitters such as radars.

The impact of the impairments depends on the specific application. For example, in the case of typical land mobile-satellite system (LMSS) links, measurements [Butterworth, 1984] and theoretical analysis (see Example Problem in § 8.2.6) indicate that the specular reflection component is usually negligible for path elevation angles above 20°. For handheld terminals, however, specular reflections may be important, as the low antenna directivity increases the potential for significant specular reflection effects.

For mobile-satellite system (MSS) link design, reflection multipath fading in combination with possible shadowing and blockage of the direct signal from the satellite is generally the dominant system impairment. However, it should be borne in mind that for frequencies below a few gigahertz, ionospheric propagation effects (Chapter 7) can be quite important, and for frequencies above a few gigahertz, tropospheric effects (Chapters 3-6) may not be negligible.

#### **8.2 Effects of the Earth's surface**

Prediction of the propagation impairments caused by reflections from the Earth's surface and from objects (buildings, vegetation) on the surface is difficult because the possible impairment scenarios are numerous, complex, and often cannot be easily quantified (for example, the degree of shadowing in LMSS links frequently cannot be precisely specified). Therefore, impairment prediction models for complicated situations (especially for LMSS links) tend to be primarily empirical, while more analytical models, such as used to predict sea-reflection fading (§ 8.2.2), have restricted regions of applicability. Nevertheless, the basic features of surface reflections and the resultant effects on propagating signals can be understood in terms of the general theory of surface reflections, as summarized here.

## 8.2.1 Reflection from the Earth

### 8.2.1.1 Specular reflection from a plane Earth

The reflection coefficient,  $R_0$ , of a plane surface is given by the expression:

$$R_0 = \frac{\sin \varphi - \sqrt{C}}{\sin \varphi + \sqrt{C}} \quad (8.1)$$

where  $\varphi$  is the grazing angle and

$$C = \eta - \cos^2 \varphi \quad \text{for horizontal polarization}$$

$$C = (\eta - \cos^2 \varphi) / \eta^2 \quad \text{for vertical polarization}$$

with:

$$\eta = \varepsilon_r(f) - j60\lambda\sigma(f)$$

where:

$\varepsilon_r(f)$  : relative permittivity of the surface at frequency  $f$

$\sigma(f)$  : conductivity (S/m) of the surface at frequency  $f$

$\lambda$  : free space wavelength (m)

This function is shown in Figure 8.1 as a function of the grazing angle for various frequencies and two sets of values for  $\varepsilon_r(f)$  and  $\sigma(f)$  corresponding to sea water and dry ground respectively [Hall, 1979]. (See also Recommendation ITU-R P.527 regarding the electrical characteristics of various types of Earth surface.) The angle at which the modulus of the reflection coefficient for vertical polarization is a minimum is known as the Brewster angle. This angle,  $\varphi_p$ , is approximately equal to  $\sin^{-1}(1/\sqrt{|\eta|})$ .

The specular reflection coefficient for vertical polarization is less than or equal to the coefficient for horizontal polarization. Thus the polarization of the reflected wave will be different from the polarization of the incident wave if the incident polarization is not purely horizontal or purely vertical. For example, a circularly polarized incident wave becomes elliptically polarized after reflection. Also, the sense of the rotation becomes reversed if the grazing angle is greater than the Brewster angle.

The calculation of magnitude and polarization of the reflected wave is usually accompanied by resolving the incident wave into horizontal and vertical components and then computing the magnitude and phase of each component of the reflected wave using Equation (8.1).

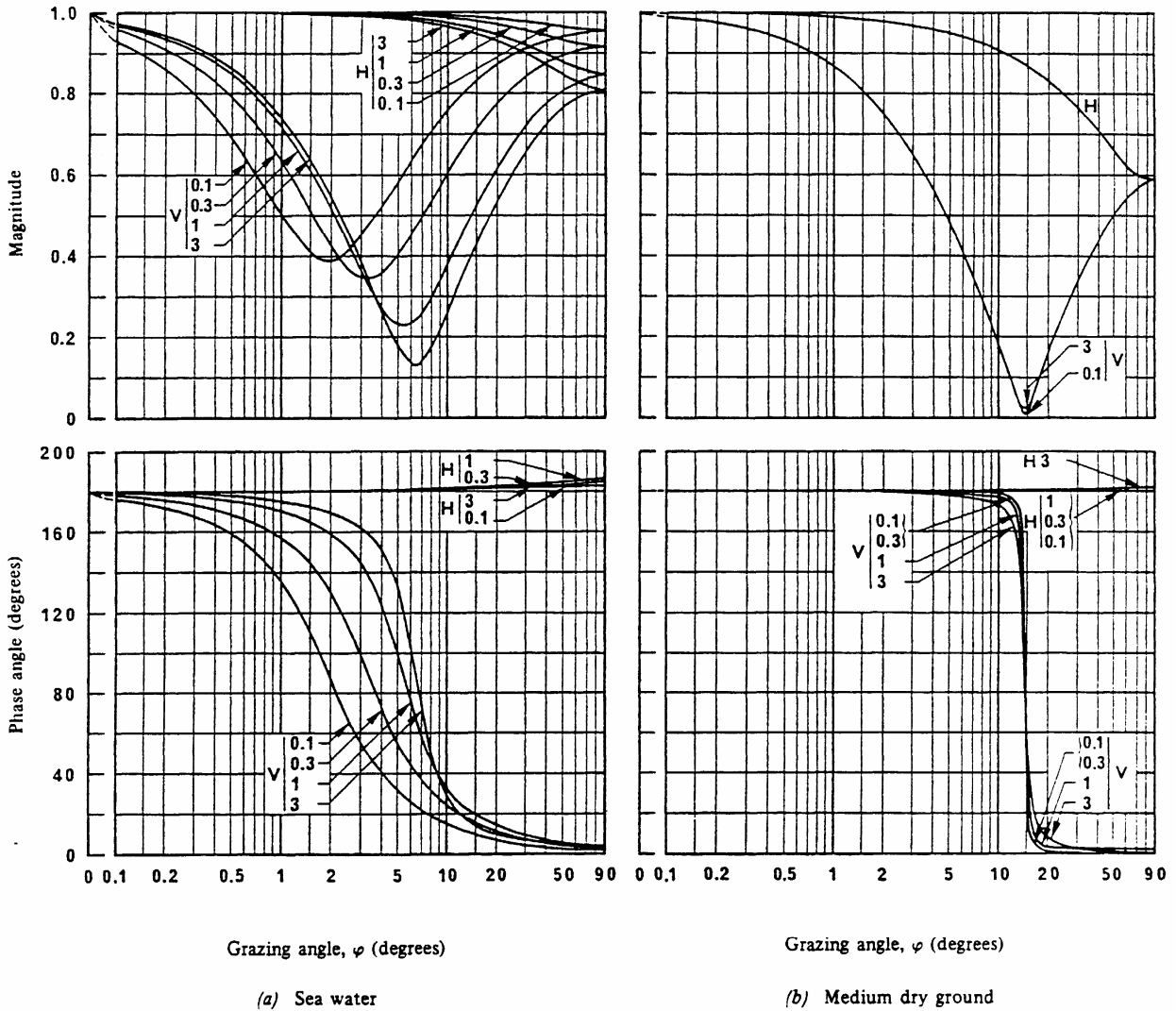


FIGURE 8.1

**Magnitude and phase of the reflection coefficient of a plane surface as functions of grazing angle,  $\phi$ , for vertical V and horizontal H polarizations.**

The frequencies are given in GHz.

NOTE – The characteristics of sea water and medium dry ground are given in Recommendation ITU-R P.527.

### 8.2.1.2 Specular reflection from a smooth spherical Earth

A signal reflected from a smooth spherical Earth, as shown in Figure 8.2, is called a specularly reflected signal because the incident grazing angle,  $\phi$ , is equal to the angle of reflection. The amplitude of the reflected signal is equal to the amplitude of the incident signal multiplied by the modulus of the reflection coefficient,  $R$ . The phase of the reflected signal is the sum of the phase changes due to reflection plus that due to the path length difference between the direct and reflected signal paths.

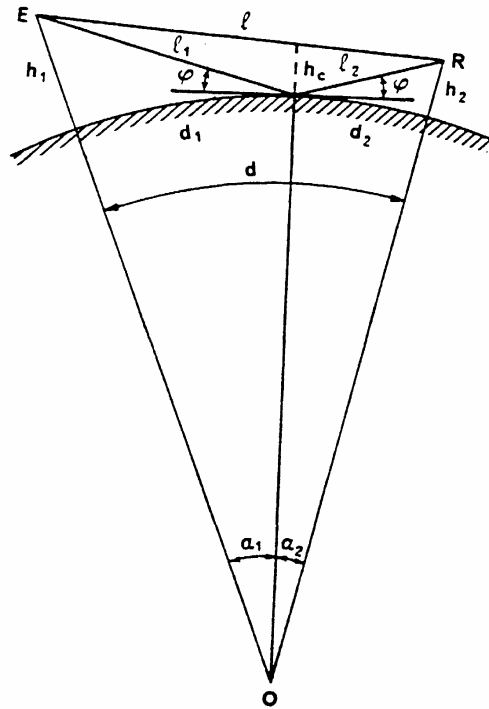


FIGURE 8.2

### Geometrical elements of reflection from a spherical Earth

An analysis of surface reflections requires a determination of the geometrical specular reflection point located at some distance,  $d_1$ , from one of the terminals. This is not easy to determine as an exact solution exists only for a flat Earth. Approximate solutions are available for small angular distances for terminals near the surface of the Earth and for very large distances between such terminals such as the case of an earth terminal and a geostationary satellite [Boithias, 1987].

For Earth-space paths  $l$  and  $l_1$  are nearly parallel because of the great distances involved. In this case:

$$d_1 \approx h \cot \theta \quad (8.2)$$

$$\Delta \approx 2h \sin \theta \quad (8.3)$$

$$\varphi \approx \theta + \frac{h}{a_e + h} \cot \theta \text{ radians} \quad (8.4)$$

where  $\theta$  is the elevation angle of the satellite,  $h$  is the height of the earth station above the surface and  $a_e$  is the effective Earth radius.

#### 8.2.1.3 Divergence factor

When rays are specularly reflected from a spherical surface, there is an effective reduction in the reflection coefficient which is actually a geometrical effect arising from the divergence of the rays. This effect is taken into account by writing the smooth spherical Earth reflection coefficient as

$$R = D R_0 \quad (8.5)$$

where  $R_0$  is the plane surface coefficient of Equation (8.1) and  $D$  is a divergence factor.

The divergence factor for Earth-space paths may be written:

$$D = \left[ 1 + \frac{2h \tan E}{a_e \sin \varphi} \right]^{-1/2} \quad (8.6)$$

Equation (8.6) has a value of  $\approx 1$  for elevation angles above about  $5^\circ$  and terminal heights below 2 km.

On a smooth spherical Earth, one can consider the reflection mechanism as the reflection of a single incident ray from a single geometrical point. The entire surface, however, contributes to the reflected signal with the major contribution coming from the surface Fresnel zones close to the geometrical reflection point.

The effective reflection coefficient of a spherical Earth, including the effects of divergence and partial reflection is:

$$R = FDR_0 \quad (8.7)$$

where  $F$  is the partial reflection coefficient. In theory,  $F$  can have a value between 0 and 2; in practice, for the majority of cases, it has a value between 0.1 and 1.2.

#### 8.2.1.4 Reflection from rough surfaces

In many practical cases, the surface of the Earth is not smooth. The reflection of radio signals from rough surfaces has been studied extensively [Beckmann and Spizzichino, 1963] but the complexity of the problem has prevented the development of engineering formulae which fully describe the reflection process.

One useful formula is a quantitative definition of the Rayleigh roughness criterion:

$$g = 4\pi(S_h / \lambda) \sin \varphi \quad (8.8)$$

where:

$S_h$ : standard deviation of the surface height about the local mean value within the first Fresnel zone:

$\lambda$ : free-space wavelength: and

$\varphi$ : grazing angle measured with respect to a tangent to the surface.

In general, a surface can be considered smooth for  $g < 0.3$ . When the surface is rough, the reflected signal has two components: one is a specular component which is coherent with the incident signal, the other is a diffuse component which fluctuates in amplitude and phase with a Rayleigh distribution.

#### 8.2.1.4.1 Specular reflection coefficient for rough surfaces

The specular component arises from coherent reflection, in the plane of incidence, from the Fresnel zones located about the geometrical reflection point. It can be described by a reflection coefficient  $R_s = \rho_s R$  where  $\rho_s$  is a reduction factor which is model dependent. For slightly rough surfaces with a random height distribution:

$$\rho_s = \exp(-g^2 / 2) \quad (8.9)$$

or very rough surfaces Equation (8.9) tends to underestimate  $\rho_s$ . Theoretical models which consider multiple reflections [DeSanto, 1981] agree with experimental data but require numerical integration techniques to compute.

A later derivation of  $\rho_s$  [Miller *et al.*, 1984] suggests that a better estimate for this quantity is given by the expression:

$$\rho_s = \exp(-g^2 / 2) I_0(g^2 / 2) \quad (8.10)$$

where  $I_0$  is the modified Bessel function of zero order. This expression produces good agreement for measured sea surface reflection coefficients.

#### 8.2.1.4.2 Amplitude of the diffuse reflection coefficient

The diffuse component of the reflected signal arises from scattering over a large area with the major contribution coming from regions well outside the first Fresnel zone. The region contributing to the diffuse scatter is known as the “glistening surface”. Signals are scattered from this surface without any preferential direction. It is possible to define a diffuse amplitude reflection coefficient:

$$R_d = \rho_d |R| \quad (8.11)$$

where  $\rho_d$  is a coefficient which depends only on the surface irregularities.

There is no simple expression for  $\rho_d$  in the literature. It has a value of zero for a smooth Earth. It has a maximum value for very rough surfaces and this upper limit depends on antenna directivity and the nature of the surface. For low directivity antennas over bare ground or the sea, it lies between 0.2 (-14 dB) and 0.4 (-8 dB) with a most probable value of 0.35 for very rough surfaces. For cases where the glistening surface is not fully illuminated because of high directivity antennas, screening or where surface vegetation introduces significant surface absorption,  $\rho_d$  is less than 0.2 and may be negligible.

Experimental measurements and theoretical analysis indicate that the diffuse component is statistically random with a Rayleigh distribution.

#### 8.2.1.4.3 Total reflected field

Figure 8.3 illustrates the specular and diffuse reduction factors measured for a sea surface [Beard, 1961]. Equation (8.9) is also plotted in the figure. The total field above a reflecting surface is the resultant of the direct field, the coherent specular component and the random diffuse component. The resultant field has a Nakagami-Rice distribution. If it is assumed that the total forward scattered power is constant, then the relationship:

$$\langle \rho_s \rangle^2 + \langle \rho_d \rangle^2 = \text{constant} \quad (8.12)$$

where  $\langle \rho \rangle$  indicates r.m.s. values, may be useful in estimating the reflected field. Antenna directivity must also be considered in computing this resultant field.

The reflection from rough surfaces is the subject of several theoretical studies. Unfortunately, no convenient engineering formulae exist at present for estimating the multipath fading which results from this type of reflection, although significant progress has been made for sea surfaces at frequencies near 1.5 GHz [Karasawa and Shiokawa, 1984a]. The methodology developed for this frequency is probably valid at lower frequencies and could be a basis for extension to higher frequencies.

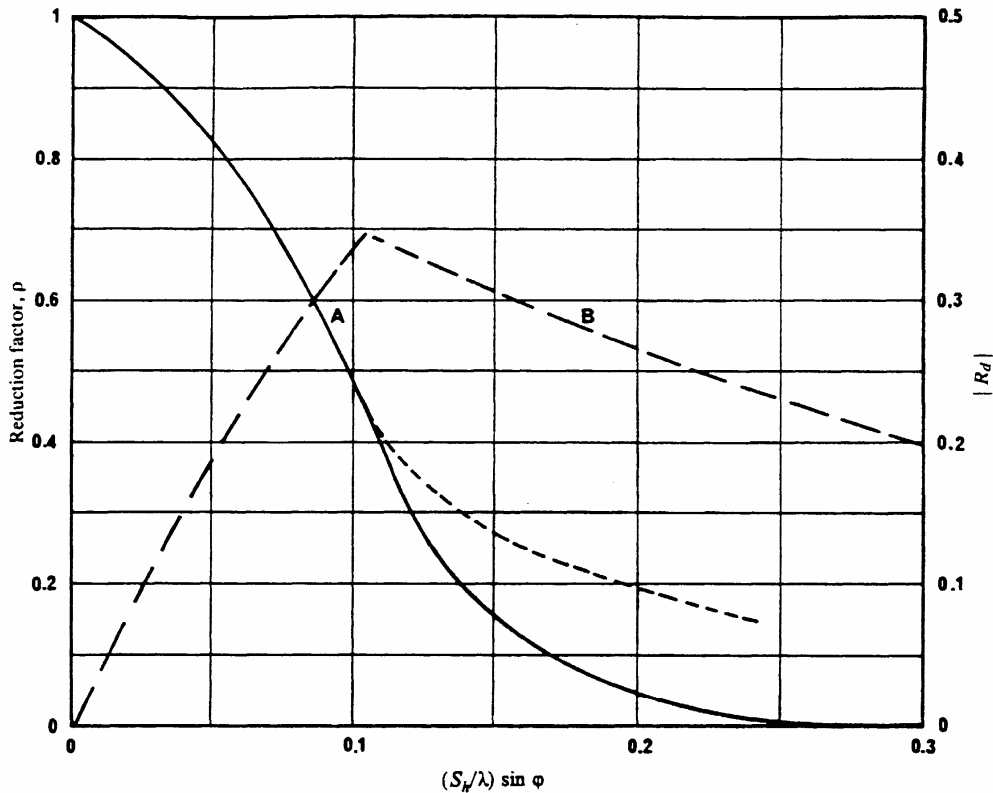


FIGURE 8.3

### Reflection from rough surfaces

Curve A is for the specular component. The solid line is calculated from Equation (8.9). The dashed line represents experimental data.

Curve B is an experimentally-measured diffuse reflection coefficient,  $R_d$ .

#### 8.2.1.5 Reflection multipath

Because of the existence of surface reflection phenomena as described above, signals may arrive at a receiver from multiple apparent sources. The combination of the direct (line-of-sight) signal with specular and diffusely-reflected waves causes signal fading at the receiver. The resultant multipath fading, on occasion in combination with varying levels of shadowing and blockage of the LOS component, can cause the received signal power to fade severely and rapidly for mobile terminals, and is therefore generally the dominant impairment in the mobile-satellite services.

Multipath models for LMSS links are found in § 5 of Recommendation ITU-R P.681, and for sea-reflection multipath for MMSS and AMSS links in § 4 of Recommendation ITU-R P.680 and § 4 of Recommendation ITU-R P.682, respectively. In addition, multipath fading is treated in §§ 8.2.2 and 8.2.4 of this handbook.

## 8.2.2 Fading due to sea reflection

### 8.2.2.1 General

Multipath fading due to sea reflection is caused by the interference between direct and reflected radiowaves. The reflected waves are composed of a coherent (specular reflection) component and an incoherent (diffuse) component that fluctuates with time due to the motion of sea waves. The coherent component is predominant under calm sea conditions and at low elevation angles, whereas the incoherent becomes significant in rough sea conditions. If the intensity of the coherent component and the variance of the incoherent component are both known, the cumulative time distribution of the signal intensity can be determined by statistical considerations [Beckmann and Spizzichino, 1963; Karasawa and Shiokawa, 1984a].

For historical reasons, a prediction model for multipath fading due to sea reflection was first developed for application to maritime mobile-satellite systems (MMSS) at frequencies near 1.5 GHz. Although the mechanism of sea reflection is common for MMSS and aeronautical mobile-satellite systems (AMSS), fading characteristics for AMSS are expected to be different from those for MMSS, because the speed and altitude of aircraft are so much greater than those of ships.

This section gives background information for the models to predict multipath fading due to sea reflection in Recommendation ITU-R P.680 (for MMSS) and Recommendation ITU-R P.682 (for AMSS).

### 8.2.2.2 Sea surface characteristics

The most common parameter used to describe sea condition is the significant wave height,  $H$ , defined as the average value of the peak-to-trough heights of the highest one-third of all waves. Empirically,  $H$  is related to the r.m.s. height,  $h_0$ , by [Kinsman, 1965]:

$$H = 4 h_0 \quad (8.13)$$

Table 8.1 shows some statistics of the occurrence of significant wave heights in various regions of the world [Long, 1975]. The mean value of significant wave height, as measured from the satellite "GEOS-III", was found to be between 2 m and 4 m, depending on season and latitude [Sandowell and Agreen, 1984].

**TABLE 8.1**  
**Relative frequency (in %) of significant wave heights in regions of the world**  
**[Long, 1975]**

Region	Height of waves (m)					
	0-0.9	0.9-1.2	1.2-2.1	2.1-3.6	3.6-6	>6
North Atlantic, between Newfoundland and England	20	20	20	15	10	15
Mid-equatorial Atlantic	20	30	25	15	5	5
South Atlantic, latitude of southern Argentina	10	20	20	20	15	10
North pacific, latitude of Oregon and south of Alaskan peninsula	25	20	20	15	10	10
East-equatorial Pacific	25	35	25	10	5	5
West wind belt of South Pacific, latitude of southern Chile	5	20	20	20	15	15
North Indian Ocean, north-east monsoon season	55	25	10	5	0	0
North Indian Ocean, south-west monsoon season	15	15	25	20	15	10
Southern Indian Ocean, between Madagascar and northern Australia	35	25	20	15	5	5
West wind belt of southern Indian Ocean on route between Cape of Good Hope and southern Australia	10	20	20	20	15	15
Averages over all regions	22	23	20.5	15.5	9.5	9.0

To calculate the incoherent multipath component, a model for  $\beta_0$ , the slope distribution of the sea surface facets, is needed. In general, the slope distribution must be weighted according to the radio frequency since not all the slopes will contribute towards scattering at a given frequency. The sea surface can be considered as a composite rough surface consisting of large-scale roughly periodic waves upon which smaller-scale waves are superimposed.

At 1.5 GHz the smaller-scale waves can be neglected, and the r.m.s. value of the sea surface slopes appear to fall between 0.04 to 0.07 in the case of wave height less than 4 m [Karasawa and Shiokawa, 1984a]. Figure 8.4 shows the relation between the r.m.s. slope and wave height. Values of r.m.s. slope as high as 0.2 have been observed elsewhere [US Dept. of Transportation, 1973].

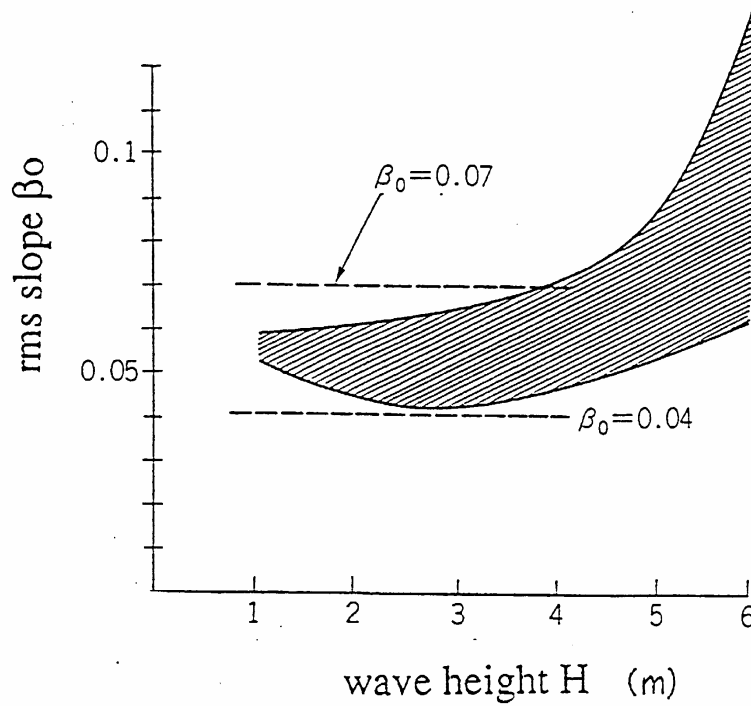


FIGURE 8.4

**Relation between wave height  $H$  and r.m.s. slope  $\beta_0$**   
**[Karasawa and Shiokawa, 1984a]**

### 8.2.2.3 Fading calculation model

#### 8.2.2.3.1 Theoretical background

The amplitude of the coherently reflected component,  $E_r^C$ , relative to the direct signal is given by:

$$E_r^C = |R|g_r \exp\left(\frac{-u^2}{2}\right) I_0\left(\frac{u^2}{2}\right) \quad (8.14)$$

with

$$u = \frac{(4\pi h_0 \sin \theta_i)}{\lambda} \quad (8.15)$$

where

- $R$  : specular reflection coefficient of the sea;
- $g_r$  : antenna gain towards the specular point, relative to boresight;
- $I_0$  : modified Bessel function of the first kind and of order zero;
- $\lambda$  : wavelength of the radio signal;
- $\theta_i$  : elevation angle.

The maximum fade depth,  $A_{max}^C$ , occurs when the coherent multipath signal is in anti-phase with the direct signal, and is given by:

$$A_{max}^C = -20 \log(1 - E_r^C) \quad \text{dB} \quad (8.16)$$

This value decreases rapidly with increasing wave height, elevation angle and frequency. In practice, due to the vertical motion of the ship antenna relative to the average sea surface height, the maximum fade value will seldom occur.

The incoherent component is random, both in amplitude and phase, as it originates from a large number of reflecting facets on the sea waves. The amplitude of this component is Rayleigh distributed and the phase has a uniform distribution. The variance of the amplitude is given by:

$$V(E_r^I) = \frac{1}{4\pi} \iint_{\text{sea surface}} |R|^2 g_r^2 \sigma \cot \theta_i d\theta_s d\phi_s \quad (8.17)$$

where

$\sigma$  : average scattering cross-section per unit area of a perfectly conducting rough surface free from multiple scattering, dependent on sea surface irregularities (namely,  $h_0$  and  $\beta_0$  described in § 8.2.2.2) and transmit and receive antenna polarizations;

$\theta_s, \phi_s$  : scattering angles as shown in Figure 8.5.

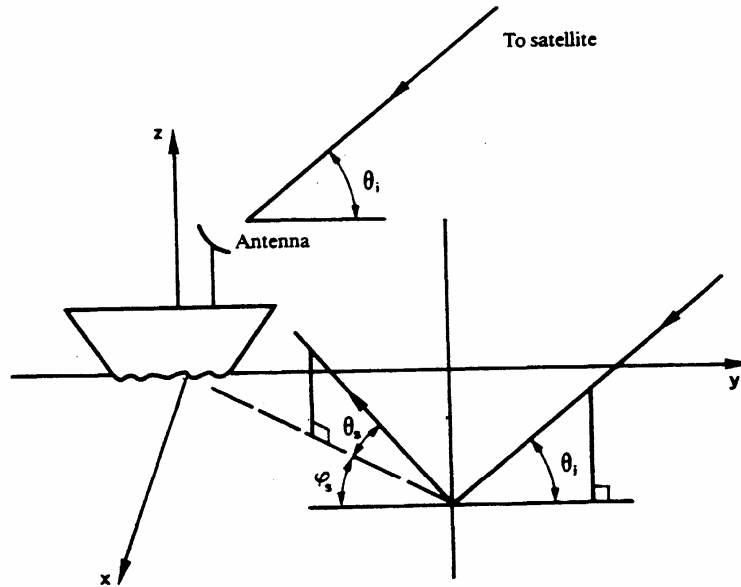


FIGURE 8.5

### Geometry of sea surface scattering

The amplitude of the resultant signal at the ship terminal, being the sum of the direct wave component, the coherent reflection and the incoherent reflection components, has a Nakagami-Rice distribution (see Recommendation ITU-R P.1057). The cumulative distribution of fading depends on the coherent-to-incoherent signal intensities. For example, in the case of rough sea conditions at 1.5 GHz, the coherent reflection from the sea is virtually non-existent and the coherent signal is composed only of the direct component [Karasawa and Shiokawa, 1984a; Dissanayake *et al.*, 1985]. Therefore, the fading is determined by the carrier-to-multipath ratio ( $C/M$ ), i.e., the power ratio of the direct signal and multipath component caused by incoherent reflections.

By adding  $A_{max}^C$ , and  $A^I(p)$  (signal fade due to the incoherent component as a function of time percentage,  $p$ ), a practical estimate of the combined fading effects of the coherent and incoherent multipath signal for the sea condition is obtained:

$$A^T(p) = A_{max}^C + A^I(p) \quad (8.18)$$

The maximum fade value due to the coherent component will not occur constantly because of the vertical motion of the ship antenna relative to the average sea surface height, therefore, the estimate using Equation (8.18) seems to give the worst-case value. In practice, for low elevation angles (less than  $10^\circ$ ) at around L-band frequencies, the maximum fading occurs when the significant wave height is between 1.5 m and 3 m, where the coherent reflected component is negligible. The dependence of fading depth on wave height in this range is relatively small [Karasawa and Shiokawa, 1984a; Ohmori *et al.*, 1985; Karasawa *et al.*, 1990a]. (See also § 8.3.3 which describes antenna motion for MMSS.)

Figure 8.6 shows fade depth not exceeded for 99% of the time and the corresponding carrier-to-multipath ratio,  $C/M$ , for circular polarization at 1.5 GHz under the condition of significant wave height from 1.5 to 3 m.

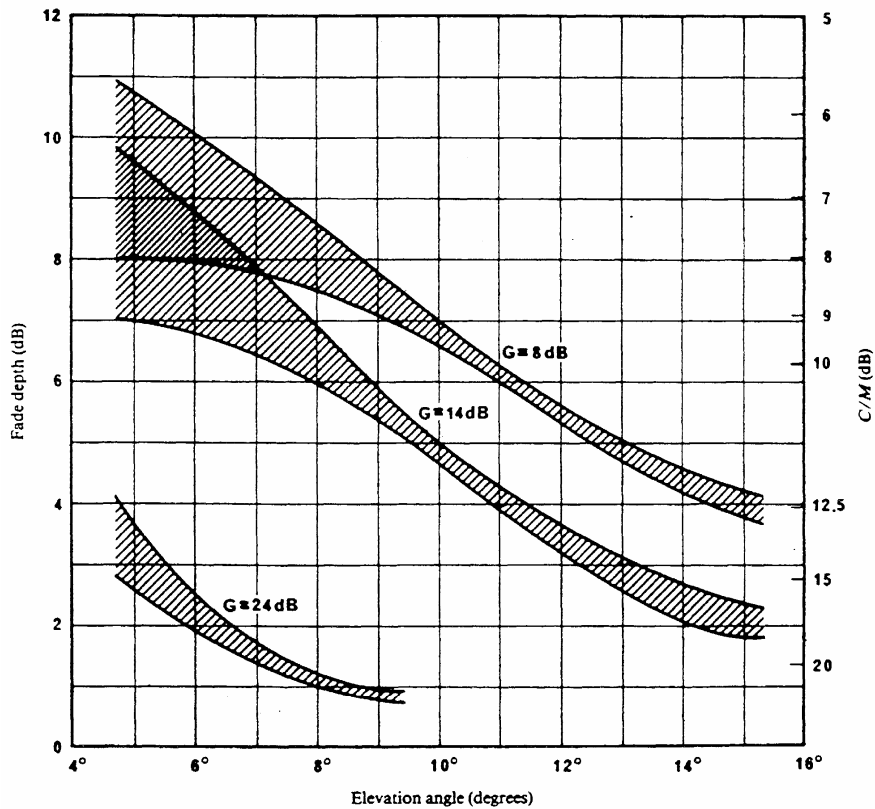


FIGURE 8.6

**Fade depth not exceeded for 99% of the time and the corresponding carrier-to-multipath ratio,  $C/M$**

Circular polarization at 1.5 GHz under the condition of significant wave height from 1.5 to 3 m (the coherent reflected component is negligible)

As the theoretical model is not suitable for engineering computations using a small calculator, simpler prediction models are useful for approximate calculation of fading or interference. Such simple methods for predicting multipath power or fading depth have been developed by Sandrin and Fang [1986] and Karasawa and Shiokawa [1988] for MMSS and Karasawa *et al.* [1990b] for AMSS. The detailed information is given in the next section.

### 8.2.2.3.2 Simple prediction method of fading depth for MMSS and AMSS

According to theoretical analysis as well as experimental results [Karasawa and Shiokawa, 1984a; 1988; Karasawa *et al.*, 1990b], most low-elevation angle Earth-space paths at 1.5 GHz approximately satisfy the following energy conservation law:

$$[\text{power of coherent component}] + [\text{average power of incoherent component}] \cong \text{constant} \quad (8.19)$$

If the above relation is satisfied, the maximum incoherent power can be estimated easily by the calculation of the coherent power at  $u = 0$ . For a more accurate estimate, small modifications of some parameter dependencies are necessary. The modified procedure has been adopted in Recommendation ITU-R P.680 for MMSS and Recommendation ITU-R P.682 for AMSS. Applicable conditions of the calculation methods are given in these Recommendations.

Figure 8.7 shows a scattergram of fading depth (i.e., fade for 99% of the time relative to that for 50%) in the case of MMSS between measured data and predicted values derived from the simple calculation method with the same conditions. In the figure,  $F_{dp2}$  are values from the method set out in Recommendation ITU-R P.680, while  $F_{dp1}$  are those from an alternative procedure with  $\theta = 2.0 \theta_i$  in Step 1 of the prediction method in place of  $\theta = 1.5 \theta_i$ . It is evident that the values given by the methods agree well with the experimental values although the methods are rather approximate.

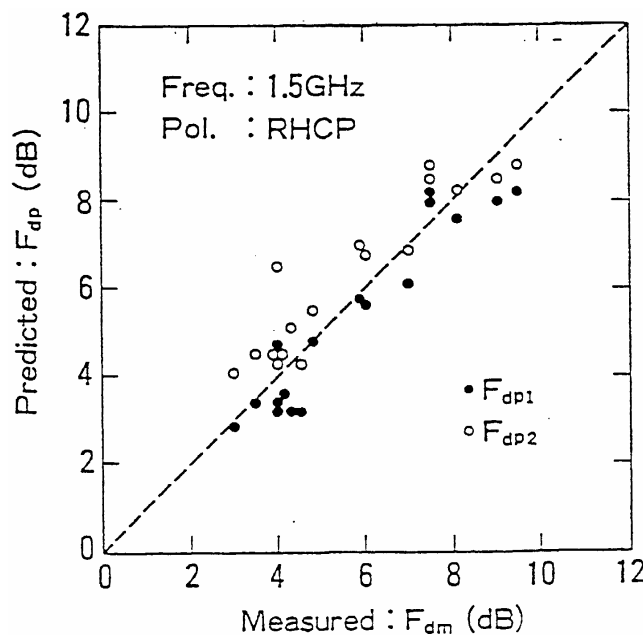


FIGURE 8.7

Scattergram of measured and predicted fading depths in MMSS

Figure 8.8 shows the altitude dependence of signal fade for 99% of time obtained from measurements with a helicopter [Karasawa *et al.*, 1990b], together with the calculated values from the simple estimation method in Recommendation ITU-R P.682 (solid line) and the theoretical model (shaded region) [Yasunaga *et al.*, 1986]. From the figure it can be seen that the simple prediction method agrees well with both the theoretical model and measured data even in the case of AMSS.

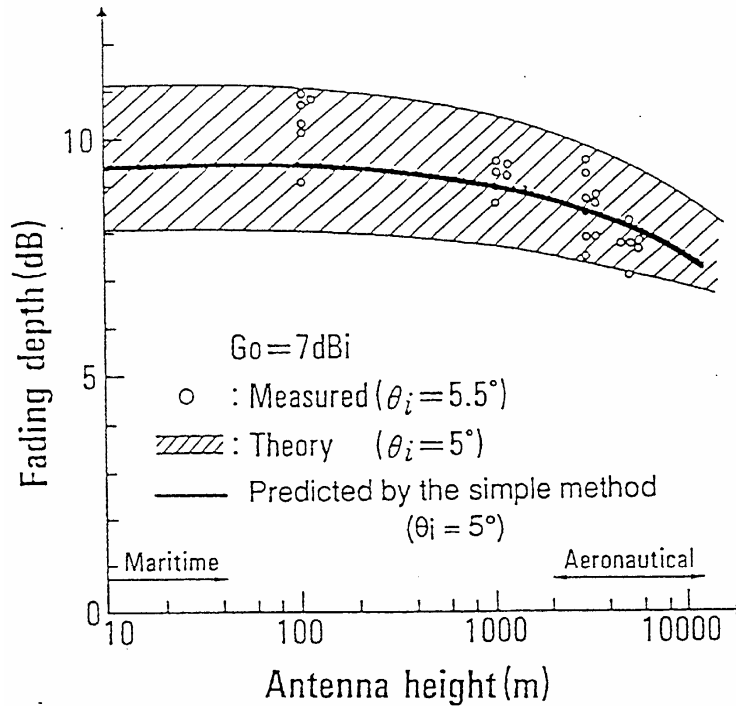


FIGURE 8.8

**Fade depth not exceeded for 99% of the time vs. antenna height**

### 8.2.2.3.3 Fading spectrum

In system design, particularly for digital transmission systems, it is important not only to estimate the fading depth but also to know the properties of temporal variations such as the frequency power spectrum and multipath fade duration statistics.

For MMSS, a theoretical analysis was carried out by Karasawa and Shiokawa [1984b]. Parameters affecting the spectrum such as wave height, wave direction, ship direction and velocity, path elevation angle, and antenna height variations due to ship motion (rolling/pitching) were taken into account.

In general, spectral bandwidth increases with increasing wave height, elevation angle, ship velocity, and the relative motion of the shipborne antenna. The dependence of the spectral shape on antenna polarization and antenna gain is usually very small. The calculated spectral shape generally follows a power law form of  $f^{-4}$ . Figure 8.9 shows the calculated power spectra of 1.5 GHz multipath fading for

three cases with wide spectral bandwidths, where the wave height is 5 m and the elevation angle is  $10^\circ$ . The -10 dB spectral bandwidth is about 5 Hz when receiving onboard a ship with significant motion.

Based on the model, the probable range of the -10 dB spectral bandwidth of 1.5 GHz fading is given in Recommendation ITU-R P.680.

Since the speed of aircraft is significantly higher than that of ships, the fluctuation speed of multipath fading in AMSS is much faster than that in MMSS, depending on flight elevation angle  $\theta_p$  measured from the horizontal plane. Calculated -10 dB spectral bandwidth is between about 20 Hz and 200 Hz for elevation angles of  $5^\circ$  to  $20^\circ$ , flight elevation angles of  $0^\circ$  to  $5^\circ$  at a speed of 1 000 km/h [Karasawa *et al.*, 1990b].

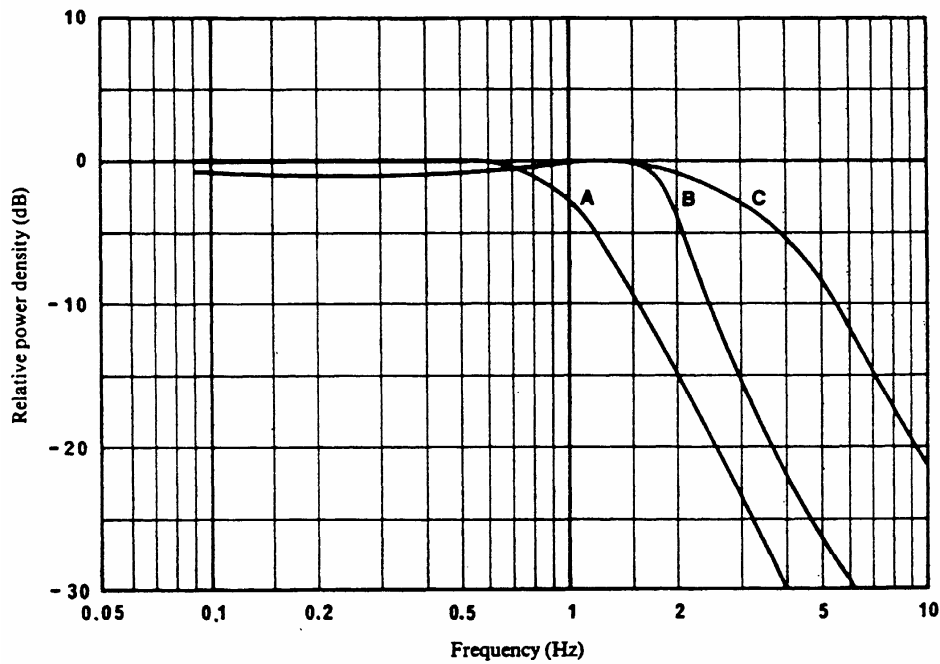


FIGURE 8.9

**Power spectra of 1.5 GHz multipath fading caused by sea surface reflection for three cases having wide spectral bandwidth**

(wave height: 5 m, elevation angle:  $10^\circ$ , antenna gain: 13 dBi)

Case A: receiving on a fixed platform

Case B: receiving onboard a ship without ship motion

Case C: receiving onboard a ship with significant motion (rolling/pitching)

**8.2.2.3.4 Fade duration statistics**

Fade duration statistics in MMSS environments were analysed by Karasawa and Shiokawa [1987] based on measured data. Fade duration  $T_D$  and fade occurrence interval  $T_I$  are defined as indicated in Figure 8.10. Mean values of  $T_D$  and  $T_I$  (namely  $\langle T_D \rangle$  and  $\langle T_I \rangle$ ) depend not only on fluctuation speed but also on the threshold level as a function of time percentage.

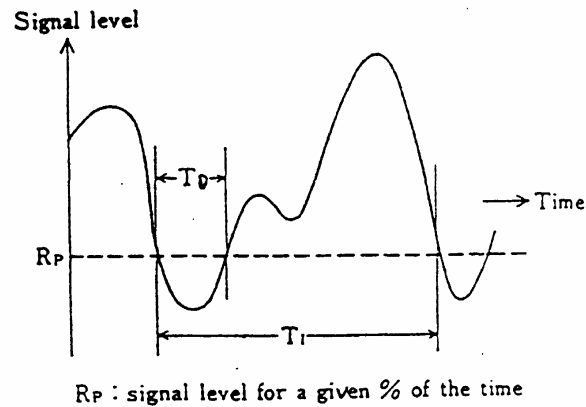


FIGURE 8.10

### Definition of fade duration and fade occurrence interval

Theoretically,  $\langle T_D \rangle$  and  $\langle T_I \rangle$  can be estimated from the frequency power spectrum when the process obeys Gaussian statistics [Papoulis, 1965]. This theoretical approach is still valid in the case of multipath fading due to sea surface reflection [Karasawa and Shiokawa, 1987]. Figure 8.11 shows a comparison of the measured value for  $\langle T_D \rangle$  and  $\langle T_I \rangle$  and those estimated from their power spectra. PDFs of  $T_D$  and  $T_I$  are close to exponential distributions.

Taking the relation between fade duration and power spectrum into account, the simplified prediction method for  $\langle T_D \rangle$  and  $\langle T_I \rangle$  in terms of -10 dB spectral bandwidth in Recommendation ITU-R P.680 was developed. Prediction errors of the method are within 10% in most cases in MMSS environments [Karasawa and Shiokawa, 1987].

#### 8.2.2.3.5 Correlation bandwidth and irreducible error rate

In the case of AMSS environments, the path difference between the direct and sea-reflected waves is quite large, and multipath fading may have frequency-selective characteristics. Correlation bandwidth as a function of antenna height was calculated [Karasawa *et al.*, 1990b] and is given in Recommendation ITU-R P.682.

Frequency-selective multipath fading in mobile channels gives rise to an irreducible error rate at which increases in the direct signal power do not reduce the corresponding error rate. Simulations of an AMSS link have been performed with a differentially-encoded MSK signal [Davarian, 1988]. The composite (direct plus diffusely-reflected) signal was modelled with Rician statistics, and the reflected signal was suitably delayed with respect to the direct signal. The composite signal was differentially detected and a BER test conducted.

The results indicate that the irreducible error rate is higher for an AMSS channel than for an LMSS channel. Increased delay of the multipath component cause the irreducible error rate to increase. Other studies [Hagenauer *et al.*, 1987; Korn, 1989] support these results and show that an increase in multipath power or delay will increase the irreducible error rate.

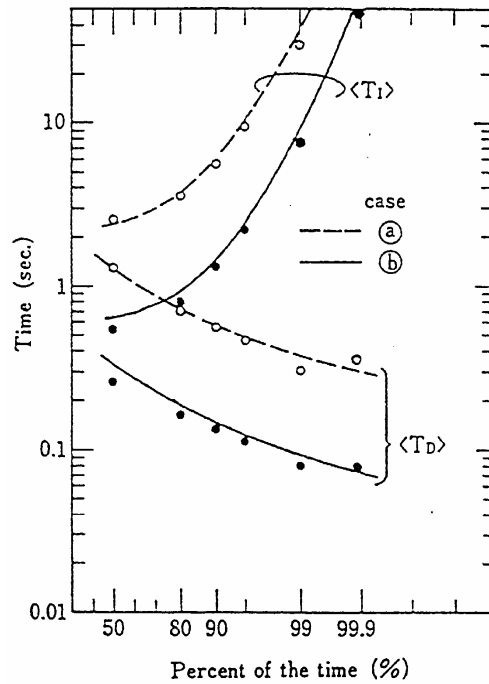


FIGURE 8.11

**Mean fade duration and fade occurrence interval as a function of threshold level corresponding to time percentage from 50% to 99.9%**

(Dots and circles are measured data; the two curves are estimated from each power spectrum)

Case	Elevation angle	Wave height	Ship velocity	Ship rolling
a	5°	0.5 m	11 knots	1°
b	10°	3 m	11 knots	5°

**8.2.3 Shadowing and blockage**

Shadowing and signal blockage due to trees, buildings, and other natural and man-made structures can be considered the dominant signal impairment in mobile-satellite communication systems. Signals received behind trees will have a direct line-of-sight component, which is reduced by the amount of absorption experienced while traversing through the tree canopy, as well as a random component arising from energy scattered from the tree. When the signal path is blocked by a solid structure such as a building, very little or no direct component exists and the communication link can be established only through diffracted and reflected signal paths. A proper understanding of different shadowing effects is required when defining coverage limits, service quality and link margins.

**8.2.3.1 Tree shadowing**

Attenuation due to trees arises from absorption by leaves and blockage by trunks and branches. Absorption from leaves is a function of the type and size of leaves and the water content in them. Blockage due to trunks is primarily a function of their size. In addition to attenuation of the direct signal, trees also cause an incoherent component due to signals reflected and diffracted off the tree surfaces. Table 8.2, extracted from Goldhirsh and Vogel [1992], shows measured attenuation levels through several types of trees at a frequency of 870 MHz. Peak attenuation levels in excess of 15 dB have been observed.

TABLE 8.2

Summary of single tree attenuation at 870 MHz [Goldhirsh and Vogel, 1992]

Tree type	Attenuation (dB)		Attenuation coefficient (dB/m)	
	Largest	Average	Largest	Average
Burr Oak	13.9	11.1	1.0	0.8
Callery Pear	18.4	10.6	1.7	1.0
Holly	19.9	12.1	2.3	1.2
Norway Maple	10.8	10.0	3.5	3.2
Pin Oak	8.4	6.3	0.85	0.6
Pin Oak	18.4	13.1	1.85	1.3
Pine Grove	17.2	15.4	1.3	1.1
Sassafras	16.1	9.8	3.2	1.9
Scotch Pine	7.7	6.6	0.9	0.7
White Pine	12.1	10.6	1.5	1.2
Overall Average	14.3	10.6	1.8	1.3

Table 8.2 shows that the average attenuation coefficient can vary over a large range; the overall average value is 1.3 dB/m. Based on these average values, a frequency scaling law for the attenuation coefficient has been derived [Goldhirsh and Vogel, 1992]:

$$\alpha_1 = \alpha_0 \sqrt{\frac{f_1}{f_0}} \text{ dB/m} \quad (8.20)$$

where  $\alpha_0$  and  $\alpha_1$  are the attenuation coefficients at the frequencies  $f_0$  and  $f_1$  respectively.

Several other empirical relationships giving the attenuation coefficient as a function of frequency are reported in the literature. Three of them are given below:

Benzair *et al.*, [1991]:  $\alpha = 0.79 f^{0.61}$  (8.21a)

Weissberger and Hauber, [1982]:  $\alpha = 0.45 f^{0.284}$  (8.21b)

Simmons, [1981]:  $\alpha = 1.102 + 1.48 \log f$  (8.21c)

where  $f$  is the frequency, in GHz.

Equation (8.21a) is based on multi-frequency measurements (1 to 4 GHz at 500 MHz intervals) behind a single foliated tree. Equation (8.21b) resulted from measurements in forested areas across a frequency range of 100 MHz to 3.2 GHz, and Equation (8.21c) is based on measurements from 9.5 to 90 GHz.

All of the above empirical relationships are plotted in Figure 8.12 together with the relationship shown in Equation (8.20) in which  $\alpha_0$  is assumed to be 1.3 dB/m at 870 MHz. It is seen that the four curves are quite distinct from each other. The disparities may have resulted from the method of measurement employed, the types of trees involved in the measurements, and the limited sample size used in each investigation. The range of variation of  $\alpha$  at 1.5 GHz is from 0.5 to 1.7 dB/m and closely follow the trends identified in Table 8.2. Measurements made with mobile receivers in rural environments appear to fall within the above range of variability. Considering the available results, an average attenuation coefficient of approximately 1.0 dB/m for L-band frequencies seems to be appropriate.

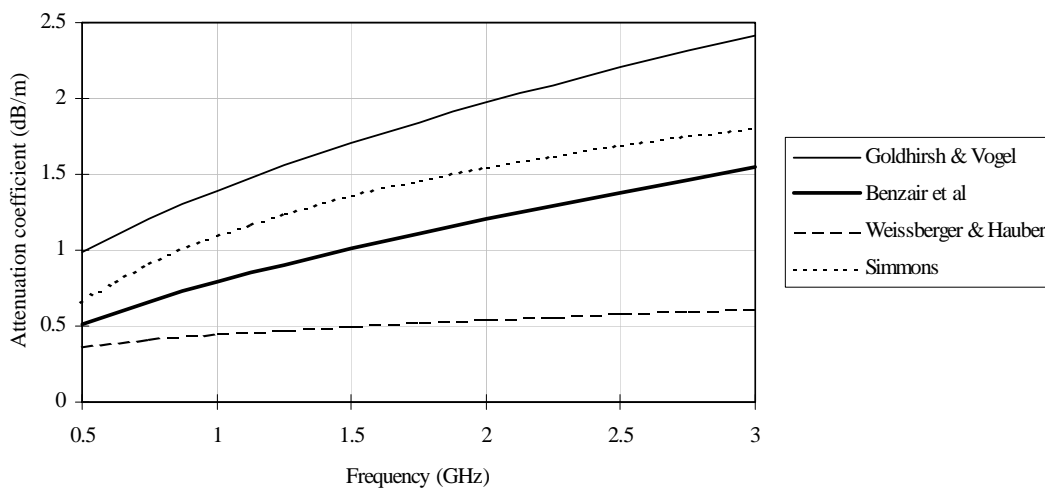


FIGURE 8.12

**A comparison of several empirical relations giving a tree attenuation coefficient as a function of frequency**

These results apply to fully foliated trees. Trees without foliage attenuate less, and the reduction in attenuation appears to be proportional to the total attenuation experienced when the tree is fully foliated. Empirically determined average reduction factors range from 0.36 [Goldhirsh and Vogel, 1992] to 0.44 [Weissberger and Hauber, 1982].

The received strength of the direct signal behind a tree will depend on the orientation of the signal path with respect to the tree. The amount of absorbing matter lying along the path will determine the degree of attenuation and hence, on average, the length of the signal path through the tree can be considered a major factor in determining the signal level. The path length is a function of the elevation angle and the distance between the receiver and the tree. The average attenuation behind an isolated tree can be estimated as the product of the attenuation coefficient and the path length through the tree. The path length through the canopy will depend on the shape of the canopy and the orientation of the signal path within the canopy. Depending on the type of tree being considered, the tree canopy may be modelled as any one of the shapes: cone, sphere, prolate spheroid, or a tetrahedron. For intermediate elevation angles (20 ° to 50°), attenuation is almost independent of elevation, and elevation dependence becomes important only at the higher and lower ends of the

elevation angle range. Alternatively, by considering the path length variability as a statistical parameter, a tree can be modelled as giving an average attenuation and a distribution around it. Both the coherent and incoherent components will vary with the receiver position, and complete decorrelation of the signal is expected over distances of the order of a few wavelengths.

In general, well-developed statistical models which fully characterize tree attenuation are not available. *In situ* measurements of attenuation from isolated trees at frequencies around 1 GHz have been performed by several investigators, and selected sources are Goldhirsh and Vogel [1987], Benzair *et al.*[1991], and Ulaby *et al.*[1990]. Some of the measurements have been made with low-gain antennas, and therefore these results may be contaminated with other artefacts such as ground reflections. Several investigations on attenuation within dense forests are also available. (See summaries in Weissberger and Hauber [1982] and Simmons [1981].) Additionally, there are measurements made with moving vehicles in rural environments where the main signal impairment is tree shadowing [Goldhirsh and Vogel, 1992; Jongejans *et al.*, 1986].

Measured signal strength distributions behind isolated trees have been reported as either normally or log-normally distributed. A log-normal distribution may be more appropriate considering the independent incremental process associated with the individual attenuation-producing components (leaves, twigs, branches, etc). The log-normal distribution is defined by two parameters, mean and standard deviation, and has the following form:

$$P(A > A_0) = \frac{1}{2} \operatorname{erfc} \left[ \frac{\ln A - \ln A_m}{\sqrt{2}\sigma} \right] \quad (8.22)$$

where  $A$  is the attenuation,  $P(A > A_0)$  is the probability of attenuation exceeding the specified value  $A_0$ ,  $A_m$  is the mean value of  $A$ , and  $\sigma$  is the standard deviation of  $\ln(A)$ .

The mean value of the attenuation can be determined from the attenuation coefficient after establishing the average path length through the canopy. The standard deviation is expected to depend on the average attenuation. However, for single tree attenuation, this dependency is expected to be rather weak. As evident from measured data from different sources [Benzair *et al.*, 1991; Jongejans *et al.*, 1986], the standard deviation ranges from about 0.3 to 0.5. Assuming the standard deviation to be 0.4, Figure 8.13 shows the resultant distribution for three values of mean attenuation: 8, 10, and 12 dB.

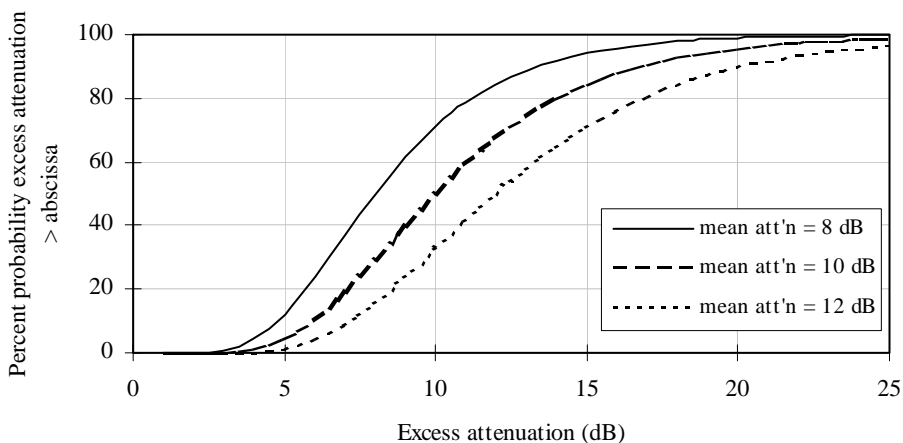


FIGURE 8.13

**Probability of tree attenuation; with three levels of mean attenuation**

The incoherent signal arising from the summation of many randomly scattered components is generally characterized in terms of the power contained in them compared with the direct signal power (carrier-to-multipath ratio,  $C/M$ ). As explained earlier, the random component is quite weak even when the direct signal is heavily attenuated. Mobile measurements in rural areas, where trees are the major source of the incoherent component, appear to suggest  $C/M$  values in excess of 12 dB.

### 8.2.3.2 Building shadowing

Signal reception behind buildings takes place mainly through diffraction and reflection. A direct line-of-sight component does not usually exist, and therefore shadowing cannot be defined unambiguously as in the case of trees. However, shadowing may be loosely defined as the power ratio between the average received signal level to the unshadowed direct signal level.

Diffractions from buildings can be studied using knife-edge diffraction theory. This is not rigorously exact, but the following gives a reasonable estimate. A conceptual view of knife-edge diffraction phenomena is shown in Figure 8.14, in which the relative signal strength is shown in both the shadowed and illuminated regions. Figure 8.14 (a) shows the loss caused by the presence of the obstacle, as a function of a dimensionless parameter  $v$ , and Figure 8.14 (b) illustrates the geometry of the path for both the illuminated and shadowed cases, in order to calculate the parameter  $v$ . From Recommendation ITU-R P.526,

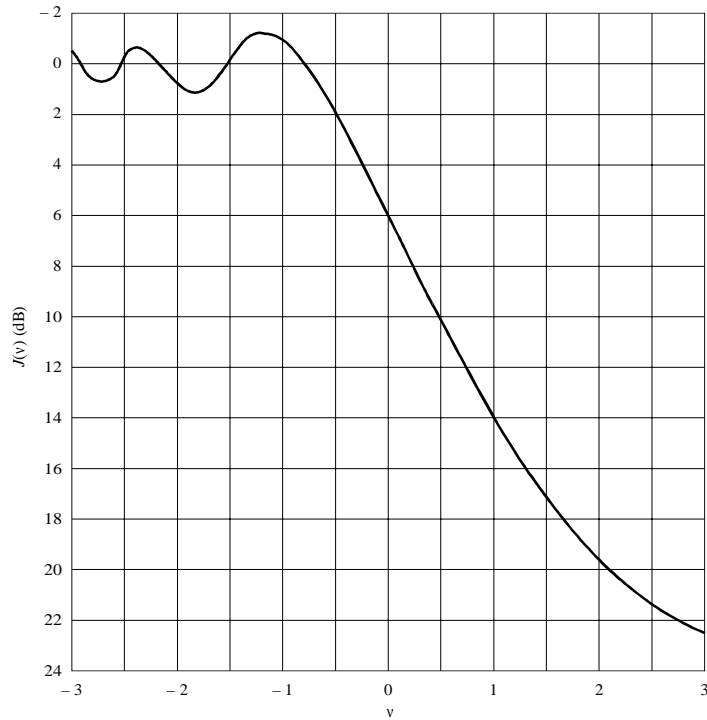
$$v = \theta \sqrt{\frac{2}{\lambda \left( \frac{1}{d_1} + \frac{1}{d_2} \right)}} \quad (8.23)$$

but  $d_1 \gg d_2$ , so

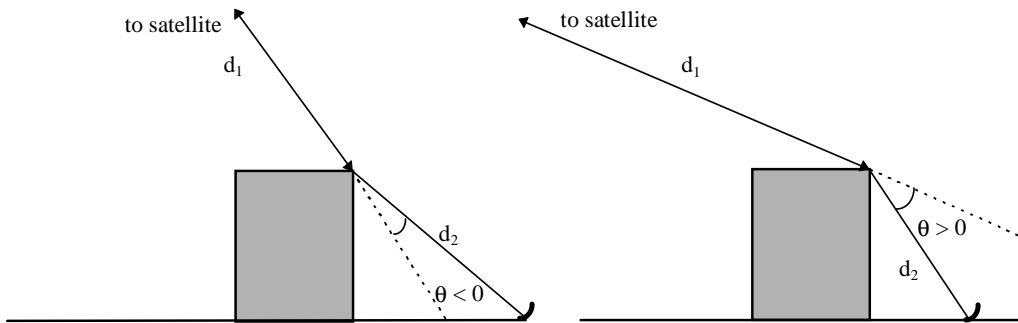
$$v \approx \theta \sqrt{\frac{2}{\lambda \left( \frac{1}{d_2} \right)}} = \theta \sqrt{\frac{2d_2}{\lambda}} \quad (8.24)$$

The signal strength at the shadow boundary is 6 dB below the line-of-sight level. In the illuminated region, the signal fluctuations are experienced due to interference between the direct component and the diffracted component. Once inside the shadowed region, the shadow loss increases rapidly. An experimental investigation into building shadowing [Yoshikawa and Kagohara, 1989] confirms the applicability of the knife-edge diffraction theory. Measured signal strength behind a building at various distances was found to follow the prediction made, assuming a single diffracting edge. However, where the building is narrow compared with its height, there may be significantly less shadowing than predicted by the above procedure. A method for finite-width screens is found in Recommendation ITU-R P.526.

When the direct signal path is blocked by a building, diffractions off the building are not expected to play a dominant role in establishing the communication link, unless the communication terminal is close to the shadow boundary. However, reflections may play a useful role in such situations, as happens in the terrestrial cellular systems.



(a) Loss due to knife-edge diffraction at edge of building



(b) Geometry of knife-edge diffraction - for calculation of  $v$

FIGURE 8.14

Building penetration depends on the type of exterior material of the building and the location inside the building. The loss through the outer structure, known as the penetration loss, is defined as the difference in median signal levels between that measured immediately outside of the building at 1.5 m above the ground, and that immediately inside the building at some reference level on the floor of interest. Measurements made at 940 MHz in a medium-size city in the United States indicate that on the ground floor of typical steel and concrete and stone office buildings, the average penetration loss is about 10 dB with a standard deviation of about 7 dB. Another set of measurements in a large city

resulted in an average ground floor penetration loss of 18 dB with a standard deviation of 7.7 dB [Walker, 1983]. The overall decrease of penetration loss with height was about 1.9 dB per floor. Table 8.3 [IEEE, 1988] provides average penetration loss for several common construction materials. Attenuation through glass ranges from about 2 to 6 dB depending on the type of glass; plain glass produces less attenuation compared to tinted or coated glass containing metallic compounds.

TABLE 8.3  
Attenuation of construction materials

Construction Material	Average Attenuation (dB)	Standard Deviation (dB)
8 inch concrete block wall	7	1
Wood and brick siding	3	0.5
Aluminium siding	2	0.5
Metal walls	12	4
Attenuation past office furnishings (dB/m)	1	0.3

Losses within a building are both a function of the distance from the exterior wall blocking the signal path, as well as the interior layout. Measurements have resulted in inverse distance power law coefficients ranging from 2 to 4.

Measurements of building attenuation using satellite-borne signals have been reported [Wells, 1977]. Measurements were made inside single-family dwellings in the USA at 860, 1 550 and 2 596 MHz using the ATS-6 satellite. The houses used for measurements were mostly wood frame with wood or similar material exterior and wood frame with brick veneer. At 1 550 MHz, an average building attenuation of 6.7 dB has been reported. Much higher levels of attenuation were found in houses containing aluminium-backed insulation material. Attenuation increases with frequency with a sensitivity of approximately 1 dB/GHz. The position of a room within a house had a very minor effect on the received signal level, with an average variation of 0.6 dB. Brick exteriors caused about 1.2 dB more attenuation than wood exteriors. No significant elevation angle dependence was observed. Horizontal polarization suffered about 1.8 dB more attenuation than vertical polarization.

Within a building, the mean signal level may be established by taking account of the penetration loss and an inverse distance dependence inside the building; inverse third power may be a reasonable approximation. Alternatively, the entry corresponding to “attenuation past office furnishings” in Table 8.3 may be used to obtain the attenuation from the exterior wall to a given location inside a room. Superimposed on the mean signal level is a varying component with a Rayleigh distribution.

#### 8.2.4 Fading in AMSS due to land reflection

An experiment aboard a helicopter over land was carried out by receiving right-hand circularly-polarized 1.5 GHz beacon signals from the Indian Ocean Region MARISAT satellite at an elevation angle of 10° [Karasawa *et al.*, 1990b]. Fading depths measured over plains such as paddy fields were fairly large (about 5 dB), nearly equal to that for sea reflection; fade depths measured over mountainous and urban areas were less than 2 dB. In the case of mountains, reflected waves are

more likely to be shadowed or diffused by the mountains. As for urban areas, the shadowing and diffusing effects of reflected waves by buildings are also large. For this reason, the ground-reflected multipath fading in these cases is not generally significant.

Results of measurements using the ATS-6 satellite [Schroeder *et al.*, 1976] are summarized in Recommendation ITU-R P.682.

## **8.2.5 Interference from adjacent satellite systems**

### **8.2.5.1 General**

In mobile-satellite communication systems for ships, aircraft and automobiles, small mobile antennas are essential for operational and economical reasons. As a result, a number of low  $G/T$  mobile earth station systems with smaller antennas have been developed. However, such antennas are subject to the restriction of frequency utilization efficiency, or coexistence between two (or more) satellite systems in the same frequency band and/or an overlap area where both satellites are visible. For coordination between two different systems in the same frequency band, a highly reliable interference evaluation model covering both interfering and interfered-with conditions is required.

Investigation into this area has been undertaken in particular by ITU-R Study Group 8. Development of such a model is an urgent matter for the ITU-R considering the number of mobile-satellite systems that are being developed.

In mobile-satellite systems, the desired signal from the satellite and the interfering signal from an adjacent satellite independently experience amplitude fluctuations due to multipath fading, necessitating a different treatment from that for fixed-satellite systems. The main technical requirement is a formulation for the statistics of differential fading, which is the difference between the amplitudes of the two signals.

The method given in § 5 of Recommendation ITU-R P.680 presents a practical prediction method for signal-to-interference ratio where the effect of thermal noise and noise-like interference is taken into account, assuming that the amplitudes of both the desired signal and interference signal affected with sea-reflected multipath fading follow Nakagami-Rice distributions. This situation is quite probable in maritime satellite communication systems.

### **8.2.5.2 Basic assumptions of the model**

Figure 8.15 is an example of interference between adjacent satellite systems, where (a) is “downlink interference” on the mobile earth-station side and (b) is “uplink interference” on the satellite side.

This applies to multiple systems sharing the same frequency band. It is anticipated that the interference causes an especially severe problem when the interfering satellite is at a low elevation angle viewed from the ship shown in Figure 8.15, because the maximum level of interference signal suffered from multipath fading increases with decreasing elevation angle. Another situation is interference between beams in multi-spot-beam operation, where the same frequency is allocated repeatedly.

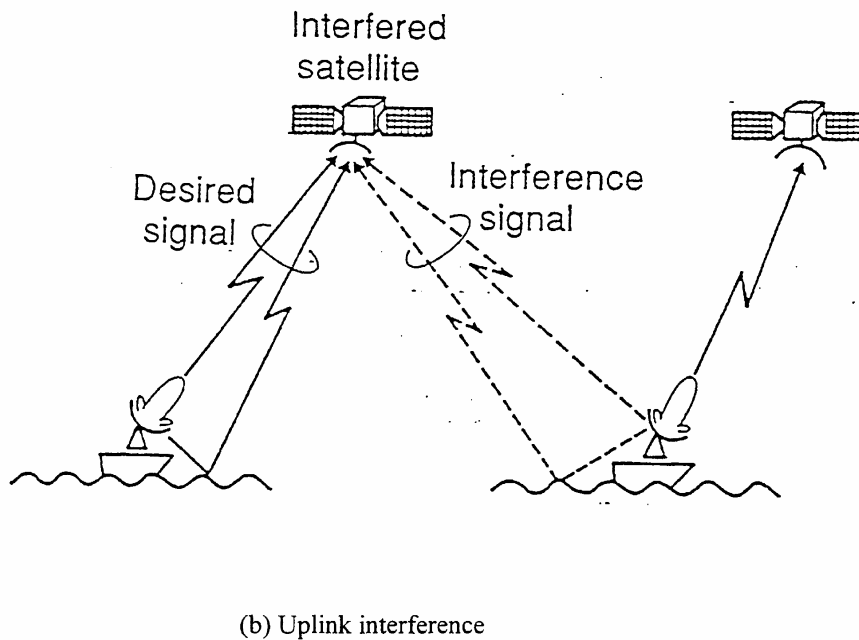
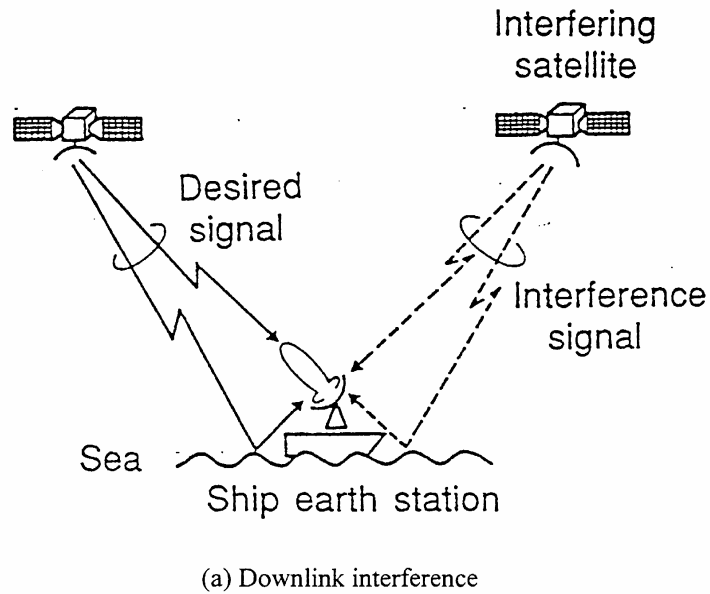


FIGURE 8.15

**Interference to/from an adjacent satellite system**

Baseline assumptions for the model are as follows [Karasawa and Yasunaga, 1991]:

- a) The amplitude of both the desired signal and interference signal follow Nakagami-Rice distributions, including a Rayleigh distribution for the interference signal. Amplitude variations of the desired and interference signals are uncorrelated.
- b) For thermal noise ( $n$ ), there are no temporal variations over time.
- c) Interference acts like thermal noise; i.e., when an interference signal and thermal noise are simultaneously present, an equivalent noise power ( $n_e$ ) can be obtained by summing the interference power ( $i$ ) and thermal noise power (namely,  $n_e = n + i$ ).

### 8.2.5.3 Prediction accuracy

The accuracy of the model presented here was evaluated by comparing a rigorous theoretical model satisfying the assumptions set out above [Karasawa and Yasunaga, 1991]. For all cases within the following parameter range ( $D$ : direct wave power of desired signal;  $N$ : averaged system noise power;  $M$ : averaged multipath power of desired signal;  $I$ : averaged power of interference):

$$N/D \leq -5 \text{ dB}; M/D \leq -5 \text{ dB}; I/D \leq -10 \text{ dB}$$

the maximum deviation of the predicted value ( $\epsilon_{max}$ ) for each time percentage, with  $\epsilon_{max}$  (dB) given by

$$\epsilon_{max} = \max ( | \text{[value estimated by simple method]} - \text{[rigorous value]} | )$$

is as follows:

$p$ (%):	80	90	99	99.9	99.99
$\epsilon_{max}$ (dB):	0.24	0.34	0.55	0.66	0.71

The maximum error increases with increasing time percentage,  $p$ . In the usual case however where the degradation of  $[c/(n+i)$ ;  $c$  is desired signal power] itself is very large (i.e., of the order of 10 to 20 dB lower than  $D/N$ ), the error is relatively small. Moreover, the error tends to be biased toward a conservative estimate, which seems desirable for interference prediction.

### 8.2.6 Example problem

To illustrate some of the concepts introduced in previous sections of this chapter, a fading calculation for a LMSS system is performed here. The geometry and link parameters correspond to mid-latitude reception of geostationary satellite signals by a LMSS system operating under line-of-sight (LOS) conditions. Note that the reflection coefficients used in the example must be obtained from reference sources (as Figure 8.1 of this handbook; see also Recommendation ITU-R P.527).

*System parameters:*

Transmission signal:	1 GHz, circularly polarized
Elevation angle, $\theta$ :	30° (boresight)
Mobile antenna:	circularly polarized
Antenna gain (co-polar), $g_{cr}$ :	4 dBi at $\theta = 30^\circ$ 0 dBi at $\theta < 0^\circ$
Antenna gain (cross-polar), $g_{xr}$ :	-6 dBi for $\theta < 0^\circ$

*Ionospheric effects:*

From Chapter 7, ionospheric effects are determined to be negligible at mid-latitudes except for Faraday rotation. As the transmissions are circularly polarized, Faraday rotation will not be a factor (see § 5.3.1).

*Tropospheric effects:*

From Chapter 3, attenuation effects are found to be negligible. From Chapter 6, refractive effects will be negligible for elevation angles above 5°.

*Ground effects:*

In this example:

- $R_{CS}$  and  $R_{XS}$ : co- and cross-polarized reflection coefficients from a curved Earth for a circularly-polarized incident wave;
- $\rho_S$ : terrain roughness factor (related to  $S_h$ , the r.m.s. value of the terrain height irregularities);
- $D$ : curved-Earth divergence factor (=1 for all normal conditions);
- $R_V$  and  $R_H$ : plane-Earth reflection coefficients for vertical and horizontal polarizations respectively; and
- $R_d$ : diffuse reflection component, relative to the direct component.

(See § 8.2.1 for a discussion of reflection from the Earth's surface and definitions of terms.) Here, assume  $S_h = 0.1$  m, and use reflection coefficients for average ground.

Since for a land mobile terminal (e.g. a vehicle-mounted antenna),  $h = 0$ , from Equation (8.4):

$$\varphi = \theta = 30^\circ$$

From Equation (8.8), the roughness parameter is:

$$g = 4\pi (S_h/\lambda) \sin \varphi = 2.09$$

*Specular component:*

$$R_{CS} = \rho_S D R_C; R_{XS} = \rho_S D R_X \quad (\text{From Equation 8.5 and the definition in § 8.2.1.4.1})$$

$$\rho_S = \exp [-g^2/2] I_0 [g^2/2] = 0.29 \quad (\text{From Equation 8.10})$$

$$D = 1$$

$$R_V = 0.33; R_H = -0.77 \quad (\text{From Figure 8.1, for dry land, at } \varphi = 30^\circ)$$

$$R_C = (R_H + R_V)/2 = (-0.77 + 0.33)/2 = -0.22$$

$$R_X = (R_H - R_V)/2 = (-0.77 - 0.33)/2 = -0.55$$

$$R_{CS} = (0.29)(1)(-0.22) = -0.064 \text{ or } -23.9 \text{ dB relative to the direct wave}$$

$$R_{XS} = (0.29)(1)(-0.55) = -0.160 \text{ or } -15.9 \text{ dB relative to the direct wave}$$

*Magnitude:*

Direct and specular components.

$|E|$  = sum of direct and specular components

$|E|$  = direct component  $\pm$  (co-polar +cross-polar specular reflections)

$|E|$  = field strength of direct component [  $1 \pm$  (co-polar antenna gain towards specular reflection point)(co-polar reflection coefficient) + (cross-polar antenna gain towards specular reflection point)(cross-polar reflection coefficient)]

$|E| = E_0 |1 \pm [g_{cr}(-60^\circ)R_{cs} + g_{xr}(-60^\circ)R_{xs}]|$

$|E| = E_0 |1 \pm [(0.63)(-0.064) + (0.316)(-0.16)]|$

$|E| = E_0 |1 \pm 0.0908|$

or

+0.75 dB to -0.83 dB relative to  $E_0$ , the field strength of the direct signal.

The specular component, 20.8 dB below the direct component (0.0908 as a ratio), when added to the direct wave produces a resultant that will fluctuate 0.8 dB around the direct wave ( $E_0$ ) for a 30° elevation angle. The elevation angle of the ground-reflected signal is above the Brewster angle, and the signal has the opposite sense of polarization than that of the direct signal.

*Diffuse component:*

Assume the mean value of the magnitude of the diffuse component  $\langle |R_d| \rangle \approx 0.08$ , (based on a typical value of  $\rho_d = 0.35$  for very rough surfaces and  $|R| = |-0.22| = 0.22$ , as computed in the analysis for the specular component above.)

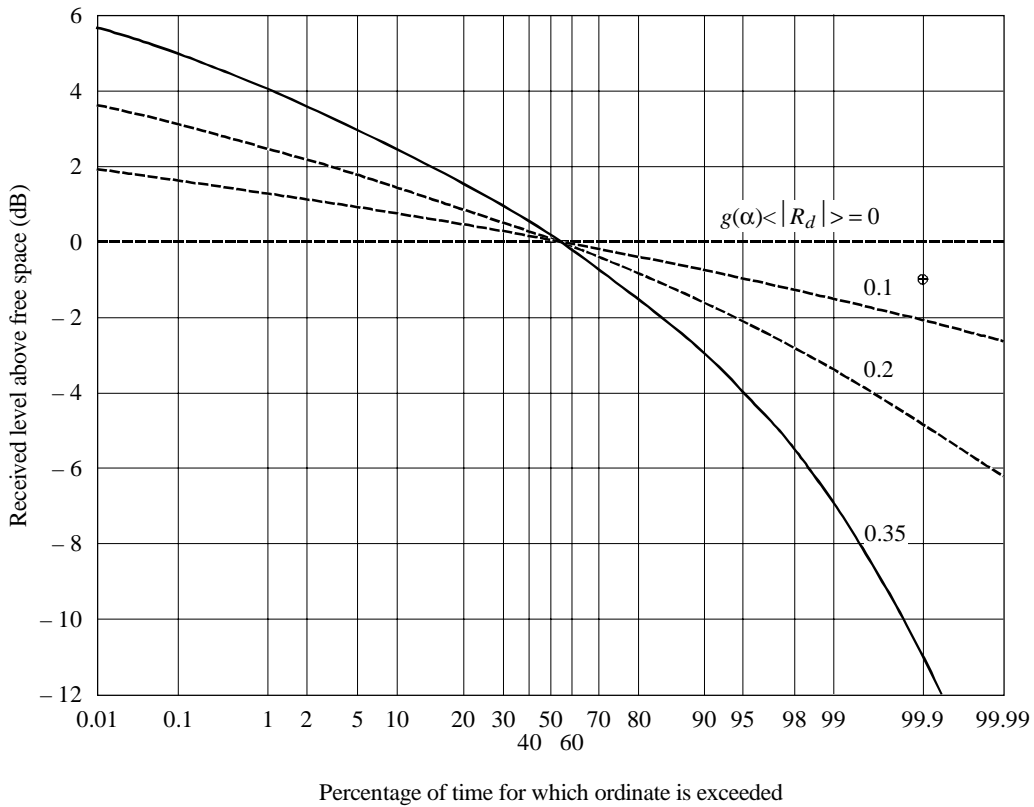
Assume the direct + specular is  $E_0$  (i.e., ignore the specular component).

Resultant received signal magnitude =  $E_0 [1 + |R_d| g(\alpha)]$

where  $|R_d|$  is Rayleigh distributed and  $g(\alpha)$  is taken as 0.63 (or -4 dB), the co-polar receiving antenna gain for off-boresight angles greater than 30°.

The resultant received signal is Nakagami-Rice distributed (see Recommendation ITU-R P.1057) and can be read from Figure 8.16. Due to antenna discrimination, the value of  $\langle |R_d| \rangle g(\alpha)$  used in Figure 8.16 should be  $(0.08)(0.63) = 0.05$ . As shown by the symbol  $\oplus$  in the figure, the signal fading caused by diffuse scatter is expected to exceed about 1 dB for 99.9% of the time under line-of-sight conditions. This level of fading is quite small and of minor consequence for system design.

The same conclusion is not generally true for sea-surface scattering, however (see § 8.2.2.3.1). Furthermore, as indicated by Equation (8.8), the effective roughness of a surface increases as frequency increases (or conversely, as  $\lambda$  decreases), so that the relative strength of the diffuse component will increase with frequency. (However, at higher frequencies, the antennas employed are often more directive, and may accordingly provide even better discrimination against the diffuse component than in the example above.)



The symbol  $\oplus$  corresponds to parameter values used in the example

FIGURE 8.16

**Amplitude distribution (dB) of a coherent signal combined with a Rayleigh-distributed reflected signal (reduced by the off-boresight antenna gain  $g(\alpha)$ ) (based on Beckmann and Spizzichino [1963])**

**8.2.7 Results of experimental measurements**

The complexity of shadowing, blockage and multipath phenomena on MSS propagation paths, particularly for LMSS links, leads to a large degree of reliance on empirical results in the development of prediction models. Selected experimental results are presented in this section to illustrate the characteristics of the impairments and typical magnitudes of the corresponding signal degradations. In addition, some measured data on surface-reflection characteristics are presented. A summary of LMSS data from experiments conducted in various countries is available, along with discussion of the results to LMSS propagation models [Goldhirsh and Vogel, 1992].

**8.2.7.1 LMSS measurements**

For convenience, emphasis is placed on LMSS results from a series of measurements made in Canada [Butterworth and Matt, 1983; Butterworth, 1984], some with simulated satellite sources, to illustrate the dependence of fading on parameters of the propagation path.

Figure 8.17 shows the distribution functions obtained for measurements made in summer conditions (trees foliated). One-third of these routes ran through wooded areas. The measurements were

repeated with a helicopter at various heights, to provide source elevation angles of 5°, 15° and 20° at the receiving antenna. During the measurements at 5° elevation, in addition to the rapid fading due to diffuse multipath propagation, slow fading with a depth of about 8 dB was observed in areas of open terrain. It was inferred that the slow fading was due to specular reflections. This effect was not observed at higher elevation angles.

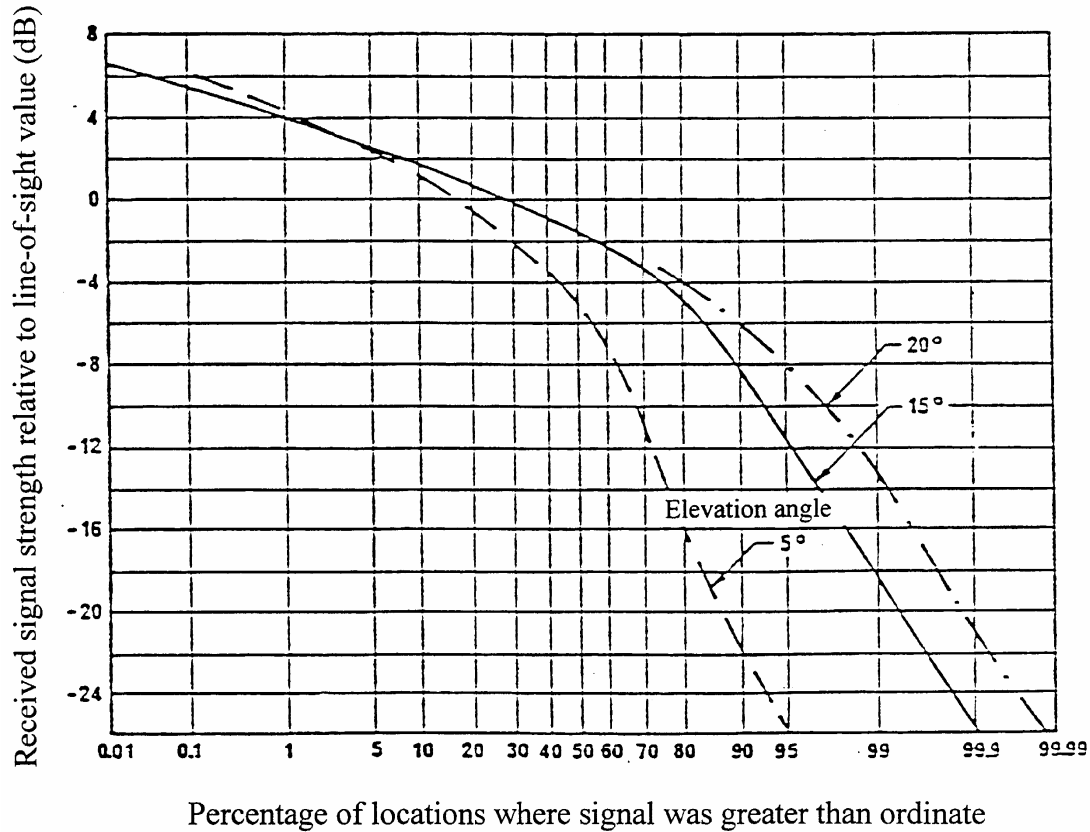


FIGURE 8.17  
**Distribution functions of data recorded at 870 MHz for various elevation angles**

Measurements at 1542 MHz using the MARECS-A satellite at 20° elevation angle have shown similar results. Fading characteristics were found to depend on the local environment, as illustrated in Figure 8.18 [Butterworth, 1984]. Typical test data could be simulated closely by assuming the multipath signals to be Rayleigh distributed, having a mean power 10 dB below the unattenuated direct signal. Shadowing effects were simulated by assuming a log-normal attenuating effect for the direct signal, with a typical mean direct signal attenuation of 7.5 dB, and a typical standard deviation of 3 dB.

A direct comparison is possible between the data taken at the two frequencies. Measurements were made over routes in the test area, 35% woodland and cleared land, at 870 MHz and 1 542 MHz. The antenna types used for both frequencies were circularly-polarized crossed drooping-dipole/ turnstiles with similar radiation patterns and with the signal source at the same elevation angle of 20°. Figure 8.19 shows this comparison. As expected, due to the increasing foliage attenuation with frequency, the excess path loss at 1 542 MHz is significantly greater than the loss at 870 MHz, for area coverage in the region of interest, i.e., above 90%.

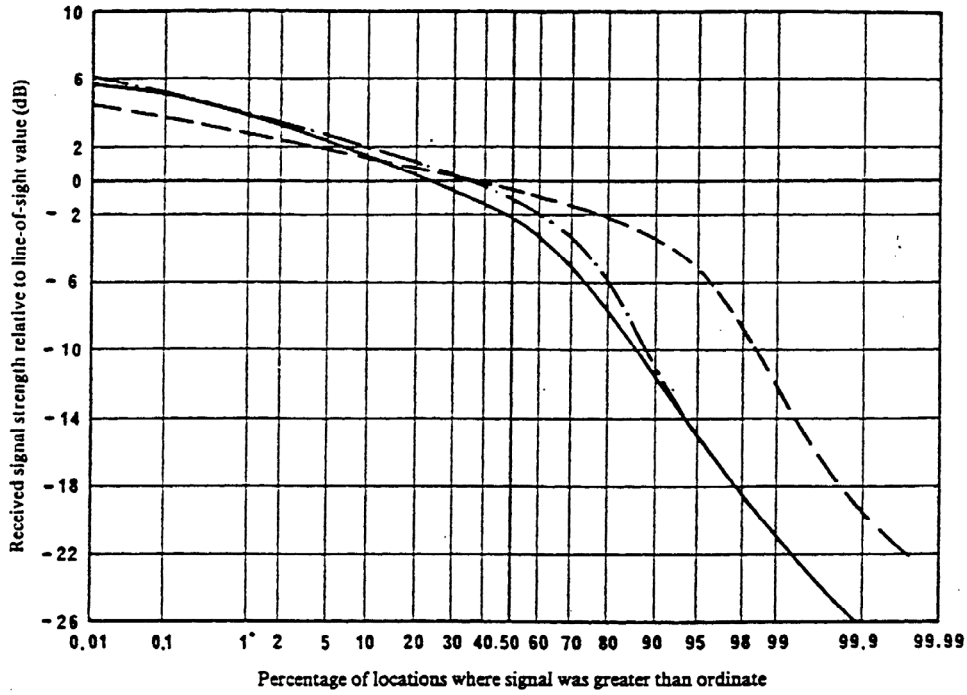


FIGURE 8.18

Envelope distribution functions recorded at 1542 MHz for circular polarization and an elevation angle of 20° for various types of terrain

— Suburban  
- - - Rural/forested  
- · - Rural/farmland

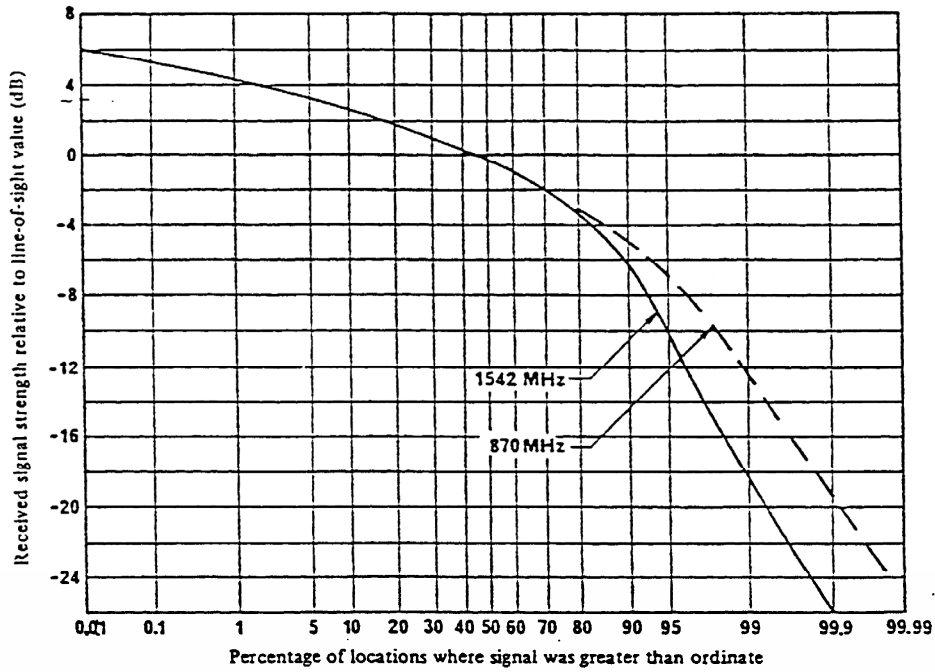


FIGURE 8.19

Comparison of 870 MHz and 1542 MHz data recorded in the same test area with the same antenna type and a signal source elevation angle of 20°

In several measurements, degradations in isolation between the co-polarized and cross-polarized components were related to corresponding multipath fading of the co-polarized channel. Equiprobability distributions of co-polar and cross-polar signals based on multiple runs for LMSS measurements in Australia [Goldhirsh and Vogel, 1992] indicated that the isolation degraded to about 11 dB for a co-polar fade of 5 dB. Consequently, successful implementation of frequency reuse by using dual-polarized signal channels on mobile-satellite paths appears unlikely because of the multipath scattering into the cross-polarized channel.

### 8.2.7.2 Measurements of sea-reflection multipath effects

A study of multipath propagation at 1.6 GHz was performed with a KC-135 aircraft and the NASA ATS-6 satellite [Schroeder *et al.*, 1976]. The signal characteristics were measured with a two-element waveguide array in the aircraft nose radome, with 1 dB beamwidths of 20° in azimuth and 50° in elevation. Data were collected over the ocean and over land at a nominal aircraft altitude of 9.1 km and with a nominal ground speed of 740 km/h.

The mean-square scatter coefficient,  $\Gamma$ , is defined as

$$\Gamma = G \frac{\langle |I|^2 \rangle}{\langle |D|^2 \rangle} \quad (8.25)$$

where:

$G$ : adjustment to account for gain differences between the direct and indirect channels;

$\langle |I|^2 \rangle$ : mean-square power in the multipath component as measured at the receiver;

$\langle |D|^2 \rangle$ : mean-square power in the direct component as measured at the receiver.

Coefficients for horizontal and vertical antenna polarizations were measured in the ATS-6 experiments. Values for r.m.s. sea surface slopes of 3° and 12° are plotted versus elevation angle in Figure 8.20, along with predictions derived from a physical optics model [Staras, 1968]. Sea slope was found to have a minor effect for elevation angles above about 10°. The agreement between measured coefficients and those predicted for a smooth flat Earth as modified by the spherical-Earth divergence factor increased as sea slope decreased. The relationship between r.m.s. sea surface slope and wave height is complex, but conversion can be performed [Karasawa and Shiokawa, 1984a].

For most aeronautical systems, circular polarization will be of greater interest than linear. For the simplified case of reflection from a smooth Earth (which should be a good assumption for elevation angles above 10°), circular co-polar and cross-polar scatter coefficients ( $\Gamma_c$  and  $\Gamma_x$ , respectively) can be expressed in terms of the horizontal and vertical coefficients ( $\Gamma_h$  and  $\Gamma_v$ , respectively) by

$$\Gamma_c = (\Gamma_h + \Gamma_v)/2 \quad ; \quad \Gamma_x = (\Gamma_h - \Gamma_v)/2 \quad (8.26)$$

for either incident right-hand circular (RHC) or left-hand circular (LHC) polarization. In general, the horizontal and vertical coefficients are complex values, and phase information is required to apply Equation (8.26) to the curves in Figure 8.20.

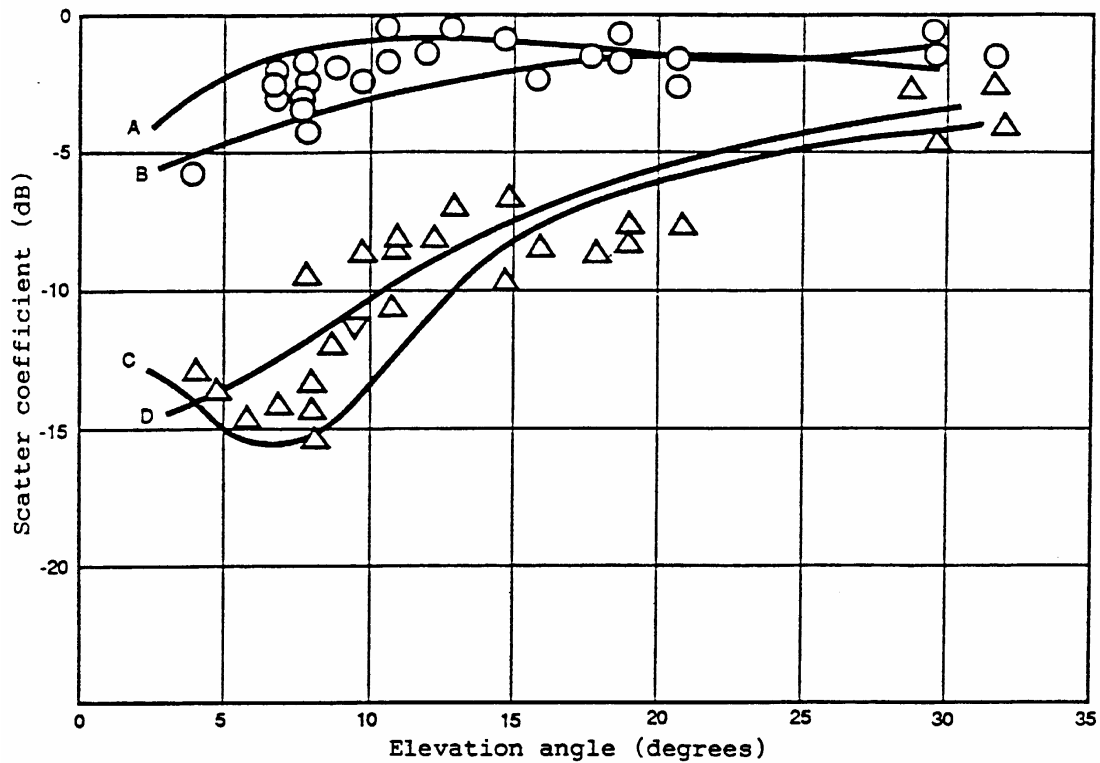


FIGURE 8.20

**Oceanic mean-square scatter coefficients vs. elevation angle at 1.6 GHz**

- O: Horizontal polarization measurements
- Δ: Vertical polarization measurements
- A: Horizontal polarization prediction, 3° slope
- B: Horizontal polarization prediction, 12° slope
- C: Vertical polarization prediction, 3° slope
- D: Vertical polarization prediction, 12° slope

**8.3 Local environmental effects**

Local environmental effects considered here are noise contributions from various sources in the vicinity of the earth terminal and the influence of the ship superstructure in the operation of maritime-mobile terminals. Models to predict propagation effects caused by local shadowing and blockage are found in § 4 of Recommendation ITU-R P.681.

**8.3.1 Noise contribution of local environment**

Some of the noise contributions from the local environment in which the earth terminal is operated are listed below:

- *Atmospheric noise from absorption*

Absorbing media, such as oxygen, water vapour, and precipitation particles, emit thermal noise that can be described in terms of antenna noise temperature. These effects are discussed in Chapter 4.

- *Man-made noise*

Heavy electrical equipment tends to generate broadband noise that can interfere with sensitive receivers. A high percentage of this noise originates as broadband impulsive noise from ignition circuits. The ambient noise generated by automobiles and trucks varies depending on the traffic density and consequently on the time of the day. The noise varies in magnitude by as much as 20 dB, depending on whether it is measured on a normal working day or on weekends and holidays when it is lower in magnitude.

- *Out-of-band emissions from radar*

Shipborne radar and surveillance radar operating in pulse mode can generate out-of-band emissions that can interfere with mobile receivers. In general, such emissions can be suppressed by inserting waveguide or coaxial filters at the radar transmitter output.

- *Interference from high-power communication transmitters*

High-power terrestrial transmitters (e.g., HF radios, TV broadcasting) can interfere with mobile earth terminals.

- *Interference from automobiles*

Under certain operation conditions, RF emissions from automobile traffic may impair receiver sensitivity. In one measurement the noise emanating from heavy traffic was recorded to be about -150 dB(mW/Hz) within the frequency band 1 535 to 1 660 MHz [Clarke *et al.*, 1974].

- *Shipyards noise*

Extremely high peak amplitudes of noise of -141 dB(mW/Hz) were recorded from Boston Navy Yard, which was in full operation at that time [Clarke *et al.*, 1974]. This noise is a combination of city ambient noise and broadband electromagnetic noise from industrial equipment.

### 8.3.2 Ship superstructure/blockage

Ship superstructure can produce both reflection multipath and blockage in the direction of the satellite. For the most part reflections from the ship's superstructure can be considered coherent with the direct signal. The fading depth due to these reflections depends on a number of parameters including:

- shape of the ship
- location of the ship antenna
- antenna directivity and sidelobe level
- axial ratio and orientation of the polarization ellipse
- azimuth and elevation angles towards the satellite

Antenna gain has a significant influence on the fading depth. Low gain antennas with broader beamwidths will collect more of the reflected signals thus producing deeper fades.

Blockage is caused by ship superstructures such as the mast and various types of antennas deployed on the ship. The geometry of blockage by a mast is shown in Figure 8.21. Signal attenuation depends on several parameters including diameter of column, distance between antenna and column, and size of antenna. Estimated attenuation due to blocking by a column type structure is shown in Figure 8.22 for antennas of 20 dB and 14 dB gain.

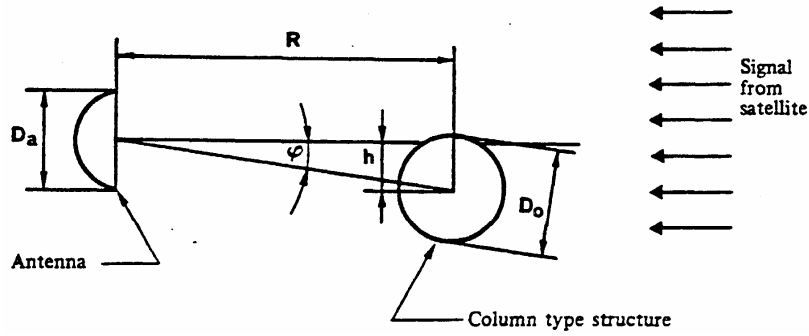


FIGURE 8.21

Geometry of blocking

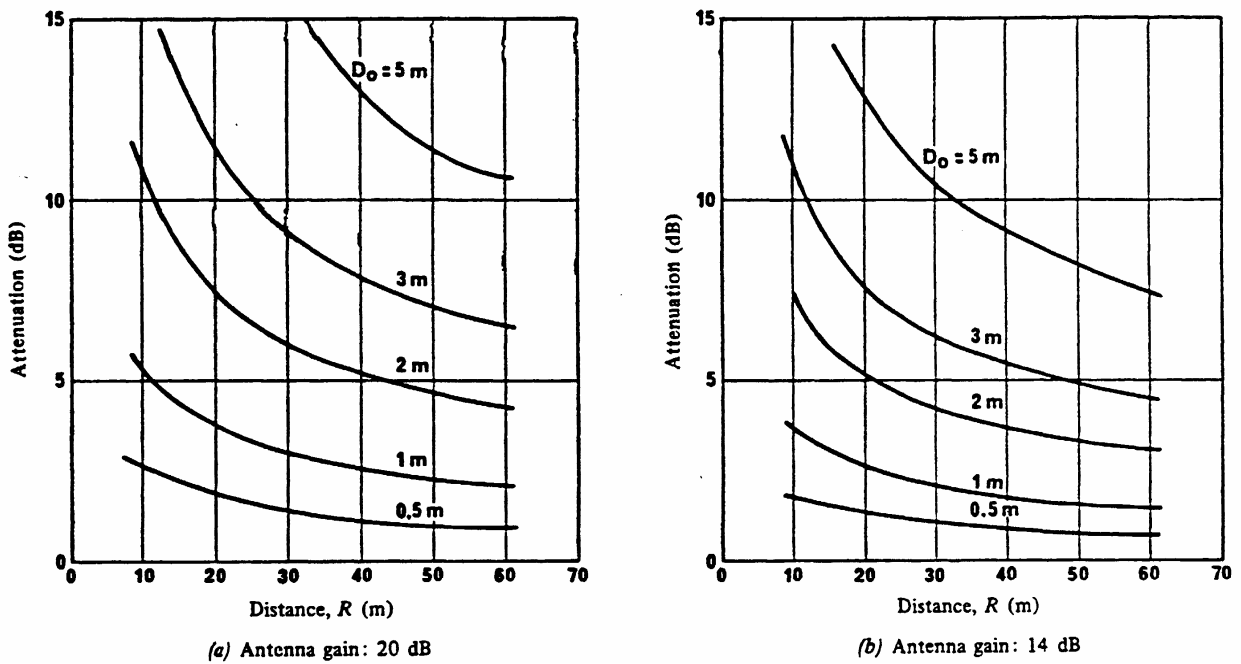


FIGURE 8.22

Estimated attenuation due to blocking

### 8.3.3 Motion of mobile antenna

The motion of mobile antennas is an important consideration in the design of maritime mobile-satellite communication systems. The received signal level is affected by the antenna off-beam gain because the antenna motion is influenced by the ship motion. The random ship motion must be compensated by a suitable stabilizing mechanism to keep the antenna properly pointed towards the satellite. This is normally achieved either through a passive gravity-stabilized platform or an active antenna tracking system. In either case the residual antenna pointing error can be significant enough to warrant its inclusion in the overall link calculation.

Experimental evidence [Satoh *et al.*, 1984] suggests that the roll motion of a ship follows a zero-mean Gaussian distribution over the short-term. The standard deviation of the distribution,  $\sigma_s$ , is a function of the vessel characteristics and the sea state or wave height. Figure 8.23 shows the distribution of the instantaneous roll angle of a ship under moderate to rough sea conditions. The distribution of the ship motion approximates to a Gaussian distribution with  $\sigma_s$  of 5.42. Also shown in the figure is the distribution of roll angle of a passively stabilized antenna under the same conditions, which also follows a zero-mean Gaussian distribution with a standard deviation of 0.99. The relation between the standard deviations of the two distributions depends on the design of the passive stabilizer. Although the antenna motion is much reduced, depending on the antenna beamwidth, the residual pointing error may be large enough to produce appreciable signal fluctuations.

Over long periods of time  $\sigma_s$  varies as a function of the sea surface conditions and its distribution can be approximated either by a log-normal distribution or a Weibull distribution [Nishinokubi and Kawashima, 1976].

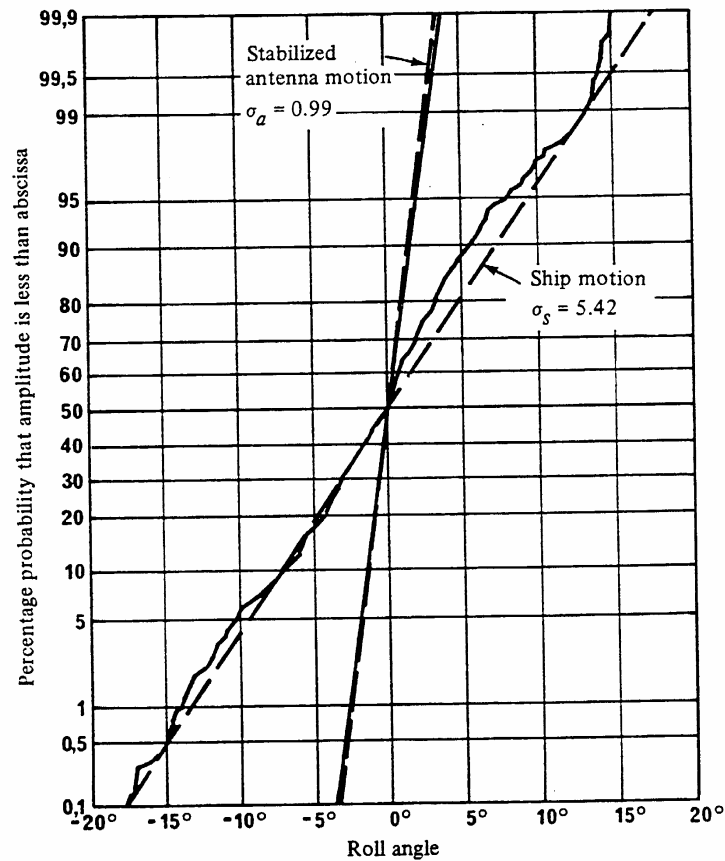


FIGURE 8.23

**Measured stabilized antenna motion**

————— Measured values  
----- Calculated values  
Wave height: approximately 5 m

REFERENCES FOR CHAPTER 8

- BEARD, C.I. [1961] Coherent and incoherent scattering of microwaves from the ocean. IRE Trans. Ant. Prop., Vol. AP-9, 5, 470-483.
- BECKMANN, P. and SPIZZICHINO, A. [1963] The scattering of electromagnetic waves from rough surfaces. Pergamon Press, New York/ Oxford.
- BENZAIR, B., SMITH, H. and NORBURY, J.R. [1991] Tree attenuation measurements at 1 - 4 GHz for mobile radio systems, International Conference on Mobile Radio and Personal Communications, Coventry, 16-20.
- BOITHIAS, L. [1987] Radiowave Propagation. McGraw-Hill Book Co., New York, 1987.
- BUTTERWORTH, J.S. and MATT, E.E. [1983] The characterization of propagation effects for land-mobile satellite services. IEE Conf. Publ. No. 222 (Satellite systems for mobile communications and navigation), 51-54.
- BUTTERWORTH, J.S. [1984] Propagation measurements for land mobile satellite systems at 1 542 MHz. CRC Technical Note No. 723, Communications Research Centre, Ottawa, Canada.
- CLARKE, J.M., CANTOR, S.R., WINCHUS, J.J. and CAPORALE, A.L. [1974] Measurement and analysis of L-band (1535-1660 MHz) electromagnetic (EM) noise on ships. Final Report No. CG-D-50-75, U.S. Dept. of Transportation, Washington, D.C.
- DAVARIAN, F. [1988] Irreducible error rate in aeronautical satellite channels. *Electron. Lett.*, Vol. 24, 21, 1332-1333.
- DeSANTO, J.A. [1981] Scattering from a rough interface. *Radio Sci.*, Vol. 16, 6, 1021-1024.
- DISSANAYAKE, A.W., JONGEJANS, A.W. and DAVIES, P.E. [1985] Preliminary results of PROSAT maritime-mobile propagation measurements. IEE Conf. Publ. No. 248, 338-342, *IEE Fourth Int. Conf. Antennas Propagat.*, Univ. Warwick, Coventry, UK.
- GOLDHIRSH, J. and VOGEL, W.J. [1987] Roadside tree attenuation measurements at UHF for land mobile satellite systems. *IEEE Trans. Antennas Propagat.*, Vol. AP-35, 589-596.
- GOLDHIRSH, J. and VOGEL, W.J. [1992] *Propagation effects for Land Mobile Satellite Systems*. NASA Reference Publication 1274.
- HAGENAUER, J., NEUL, A., PAPKE, W., DOLAINSKY, F. and EDBAUER, F. [1987] The aeronautical satellite channel. DFVLR Tech. Rep. No. NE-NT-T-87-17, May, DFVLR.
- HALL, M.P.M. [1979] *Effects of the Troposphere on Radio Communication*. IEE Electromagnetic Wave Series, 8, Peter Peregrinus Ltd., London, U.K.
- IEEE Vehicular Technology Society Committee on Radio Propagation [1988] Coverage prediction for mobile radio systems operating in the 800/900 MHz frequency range. *IEEE Trans. Vehicular Tech.*, Vol. VT-37, 3-72.
- JONGEJANS, A. DISSANAYAKE, A., HART, N., HAUGLI, H., LOISY, C. and ROGARD, R. [1986] PROSAT Phase I Report, European Space Agency, STR-216.

- KARASAWA, Y., MATSUDO, T. and SHIOKAWA, T. [1990a] Wave height and frequency dependence of multipath fading due to sea reflection in maritime satellite communications. *Electron. Commun. Japan, Part 1*, Vol. 73,1, 95-106. (Translated from IEICE Vol. 72-BII, 4, 1989)
- KARASAWA, Y. and SHIOKAWA, T. [1984a] Characteristics of L-band multipath fading due to sea surface reflection. *IEEE Trans. Antennas Propagat.*, Vol. AP-32, 6, 618-623.
- KARASAWA, Y. and SHIOKAWA, T. [1984b] Spectrum of L-band multipath fading due to sea surface reflection. *Trans. IECE of Japan*, Vol. J67-B, 2, 171-178.
- KARASAWA, Y. and SHIOKAWA, T. [1987] Fade duration statistics of L-band multipath fading due to sea surface reflection. *IEEE Trans. Antennas Propagat.*, Vol. AP-35, 8, 956-966.
- KARASAWA, Y. and SHIOKAWA, T. [1988] A simple prediction method for L-band multipath fading in rough sea conditions. *IEEE Trans. Commun.*, Vol. 36, 10, 1098-1104.
- KARASAWA, Y. and YASUNAGA, M. [1991] Interference evaluation method for mobile-satellite systems under Nakagami-Rice fading conditions. *Inst. Electro. Inform. Commun. Eng. Trans. Communications*, Vol. E75-B, 1, 42-49.
- KARASAWA, Y., YASUNAGA, M., SHIOKAWA, T. and YAMADA, M. [1990b] Propagation characteristics for aeronautical mobile-satellite systems. *13th AIAA Int. Commun. Sat. Sys. Conf.*, Los Angeles, 575-582, March.
- KINSMAN, B. [1965] *Wind waves, their generation and propagation on the ocean surface*. Prentice-Hall Inc., Englewood Cliffs, New Jersey.
- KORN, I. [1989] Coherent detection of M-ary phase-shift keying in the satellite mobile channel. *IEEE Trans. Comm.*, Vol. 37, 10, 997-1003.
- LONG, M.W. [1975] *Radar reflectivity of land and sea*. Lexington Books, Lexington, MA, USA.
- MILLER, A.R., BROWN, R.M. and VEGH, E. [1984] New derivation for the rough-surface reflection coefficient and for the distribution of sea-wave elevations. *IEE Proc.*, Vol. 131, Part H, 2, 114-116.
- NISHINOKUBI, H. and KAWASHIMA, R. [1976] On the sea keeping qualities of fishing by field measurement - III. *J. Japan Inst. Nav.*, 55, 1-6.
- OHMORI, S., IRIMATA, A., MORIKAWA, H., KONDO, K., HASE, Y. and MIURA, S. [1985] Characteristics of sea reflection fading in maritime satellite communications. *IEEE Trans. Antennas Propagat.*, Vol. AP-33, 8, 838-845.
- PAPOULIS, A. [1965] *Probability, random variables and stochastic processes*, Sec. 14-4, McGraw-Hill, New York.
- SANDOWELL, D.T. and AGREEN, R.W. [1984] Seasonal variation in wind speed and sea state from global satellite measurements. *J. Geophys. Res.*, Vol. 89, no. C2, 2041-2052.
- SANDRIN, W. and FANG, D.J. [1986] Multipath fading characterization of L-band maritime mobile satellite links. *COMSAT Tech. Rev.*, Vol. 16, 2, 319-338.
- SATOH, K., NADAMAE, M. and MISHIMA, H. [1984] A simple ship-borne antenna stabilizer for limited area maritime satellite communication systems. 35th Cong. of the International Astronautical Federation (IAF), IAF 84-86.

- SCHROEDER, E.H. *et al.* [1976] Air traffic control experimentation and evaluation with the NASA ATS-6 satellite. The Boeing Company, Rep. No. FAA-RD-75-173.
- SIMMONS, A.J. [1981] EHF propagation through foliage, MIT Lincoln Laboratory TR-594.
- STARAS, H. [1968] Rough surface scattering on a communication link. *Radio Sci.*, Vol. 3, 6, 623-631.
- ULABY, F.T., WHITT, M.W. and DOBSON, M.C. [1990] Measuring the propagation properties of a forest canopy using a polarimetric scatterometer, *IEEE Trans. Antennas Propagat*, Vol. AP-38, 251-258.
- US DEPT of TRANSPORTATION [1973] ATS-5 multipath/ranging/digital data L-band experimental program - Phase V. Rep. No. FAA-RD-73-57-V.
- WALKER, E.H. [1983] Penetration of radio signals into buildings in the cellular radio environment, *BSTJ*, Vol. 62, 2719-2734.
- WEISSBERGER, M. and HAUBER, J. [1982] An initial critical summary of models for predicting the attenuation of radiowaves by trees. ESD-TR-81-101, Electromagnetic Compatibility Analysis Center, Annapolis, MD, July 1982.
- WELLS, P.I. [1977] The attenuation of UHF radio signals by houses, *IEEE Trans. Vehicular Tech*, Vol. VT-26, 358-362.
- YASUNAGA, M. KARASAWA, Y., SHIOKAWA, T. and YAMADA, M. [1986] Characteristics of L-band multipath fading due to sea surface reflection in aeronautical satellite communications. *Trans. IECE of Japan*, Vol. E69, 10, 1060-1063.
- YOSHIKAWA, M. and KAGOHARA, M. [1989] Propagation characteristics in land mobile satellite systems, 39th IEEE Vehicular Technology Conf, 550-556.

## CHAPTER 9

### COMBINED EFFECTS MODELLING

An Earth-to-space link may be affected, as discussed in the previous sections, by several impairments (see § 1.2). These impairments may have between them different degrees of correlation or statistical dependence.

Examples of the correlation between propagation effects are, for example, rain and cloud attenuation. Since precipitation cannot occur without a cloud being present, one may say that the probability of cloud attenuation conditioned to the presence of precipitation, is one. However, the probability of precipitation conditioned to the presence of clouds is surely not one (a cloud may or may not be precipitating).

Combined effects modelling is the process of representing the composite attenuation due to all atmospheric components. The result is a distribution of joint probabilities associated with total attenuation along a propagation path. The process considers the attenuation due to each effect as a random variable. The distributions of those random variables are then combined to form a total joint probability based on assumptions of dependence and independence.

The first step is to collect distributions of attenuation based on rain, water vapour, oxygen, and hydrosols (clouds). When appropriate, a distribution of attenuation due to tropospheric scintillation is also required (see § 6.2). These distributions may be obtained using models or measurements.

The distributions are typically represented as cumulative distribution functions (CDFs). A CDF represents the probability that a random variable does not exceed a particular value. The value of the CDF for a random variable with a value of  $X$  may be derived by integrating the probability density function (PDF) of the random variable from  $-\infty$  to  $X$ . All operations discussed with respect to the distributions of attenuation are performed on CDFs. After all distributions of attenuation are collected, worst and best case estimates can be derived by assuming that the different effects are either statistically dependent or independent.

#### 9.1 Equiprobable summation

The first method, equiprobable summation, assumes a total dependence between each of the effects. The equiprobable summation function for  $N$  unique effects is given by:

$$A_{TOTAL}(P) = A_1(P) + A_2(P) + \dots + A_N(P) \quad (9.1)$$

where  $A_x(P)$  is the attenuation value of the CDF for effect  $X$  for a fixed probability level of  $P$ . By performing the equiprobable summation function at all probability levels a resultant distribution of total attenuation is produced.

The fundamental assumption of statistical dependence in equiprobable summation means that all effects are perfectly correlated. That is to say, as attenuation due to one effect increases, they all increase. While it intuitively seems reasonable that the highest rain rates will be generated by the wettest clouds, the reverse logic may not apply. Similarly, during non-rainy conditions, the assumption is made that if temperature and humidity remain constant, the presence of cloud liquid water along the path also remains constant.

Equiprobable summation provides a statistical “worst case” prediction of attenuation. This prediction best represents measured attenuation statistics when considering the highest probabilities [Feldhake, 1996]. However, the particular probability level at which equiprobable summation begins to demonstrate its greatest accuracy is dependent on specific radio system and geophysical parameters.

## 9.2 Convolution

The second method for combining effects is convolution. The convolutional method assumes statistical independence between sources of attenuation. This allows for the randomness of signal levels due to tropospheric scintillation during periods of fixed temperature and humidity. It also considers the effects of passing clouds while other path attenuators remain constant. However, when utilizing the convolutional approach, a finite probability is considered that extreme rain rates may occur in the absence of clouds. The total attenuation distribution is calculated by:

$$P(A_{TOTAL}) = \int_{-\infty}^{A_{TOTAL}} P_1(A) \cdot P_2(A_{TOTAL} - A) dA \quad (9.2)$$

where  $P_1(A)$  is the probability density of attenuation of effect 1 and  $P_2(A)$  is the cumulative attenuation distribution of effect 2. When convolving the distributions of attenuation due to two independent sources, care should be taken to ensure that the resolution of the distributions is sufficient to produce an accurate resultant.

By assuming statistical independence between effects, a second assumption is included that the random variables are perfectly uncorrelated. The result of the convolutional method represents the most realistic “best case” condition. A more optimistic “best case” prediction would occur if a perfect negative correlation were assumed between effects. This type of dependence can be observed in the frequencies either close to or inside the oxygen absorption bands between the dry air and water vapour attenuations [Salonen *et al.*, 1992]. This is due to the increasing dry air attenuation with decreasing air temperature that leads also to decreasing water vapour density and consequently smaller water vapour attenuation. Unless this specific condition is met, convolution should be used to predict the best case distribution.

## 9.3 Temporal segmentation

The use of equiprobable summation and convolution to combine effects produces statistical upper and lower bounds. Under ideal circumstances, the bounds would be defined by the same line creating a single prediction. While, in practice, this condition will never occur, temporal segmentation of the data will bring the bounds closer together [Feldhake, 1996].

Temporal segmentation is the process of separating attenuation statistics into distributions representing smaller units of time. For example, these distributions may represent monthly, seasonal, or rain/nonrain conditions. The greater the separation of the data, the more the final upper and lower bounds will be brought together.

After the data have been temporally segmented, upper and lower bounds of attenuation are derived for each time segment using the equiprobable summation and convolutional techniques. The lower bounds are then combined to create an independent case distribution for the total time. The same process is performed on the dependent case curves. The process for generating the upper and lower bound distributions for the total period of time is Bayes theorem. Bayes theorem states that for a fixed attenuation value, the resulting joint probability may be represented through a weighted average.

$$P_{RESULTANT}(A) = \frac{P_1(A)W_1 + P_2(A)W_2 + \dots + P_N(A)W_N}{\sum_{n=1}^N W_n} \quad (9.3)$$

where  $P_x(A)$  is the probability associated with the CDF of attenuation for time period  $X$  at a fixed attenuation value of  $A$ . The value of the weighting factor,  $W_x$ , is determined by the amount of time considered by CDF of period. For example, if December, January, and February CDFs were being combined to create a resultant for winter, then  $W_{DEC} = 31$ ,  $W_{JAN} = 31$ , and  $W_{FEB} = 28.25$ .

#### 9.4 Root-Square summing

Different combinations of statistical dependence and independence between effects can be assumed to achieve a best estimate of the overall combined fading [Poiars Baptista and Davies, 1994; Watson and Hu, 1994; Salonen *et al.*, 1995; 1996]. The root-sum-square (RSS) on an equiprobable basis provides a result which falls between the upper and lower statistical bounds. It is discussed in Recommendation ITU-R P.618 to combine scintillation effects with rain attenuation [Karasawa and Matsudo, 1991]. It can be expressed as:

$$A_{TOTAL} = \sqrt{A_1^2(P) + A_2^2(P)} \quad (9.4)$$

#### 9.5 Example

In this example, two combinational methods for scintillation and attenuation distributions are compared using filtered and unfiltered 11.2 GHz beacon measurements from Austin, Texas, on a 5.8° elevation path. Figure 9.1 shows the cumulative distributions for the total fade (solid curve), for the absorptive attenuation only (dotted curve - rain, atmospheric gases, and clouds), and for the scintillation fade (dot-dash curve). Total attenuation distributions derived from the scintillation and absorptive attenuation distributions using the convolution and RSS methods are also shown. The cumulative distribution from the convolution method differs little from the measured total fade distribution, while the method using RSS underestimates the effect of scintillation in the low fade margin range.

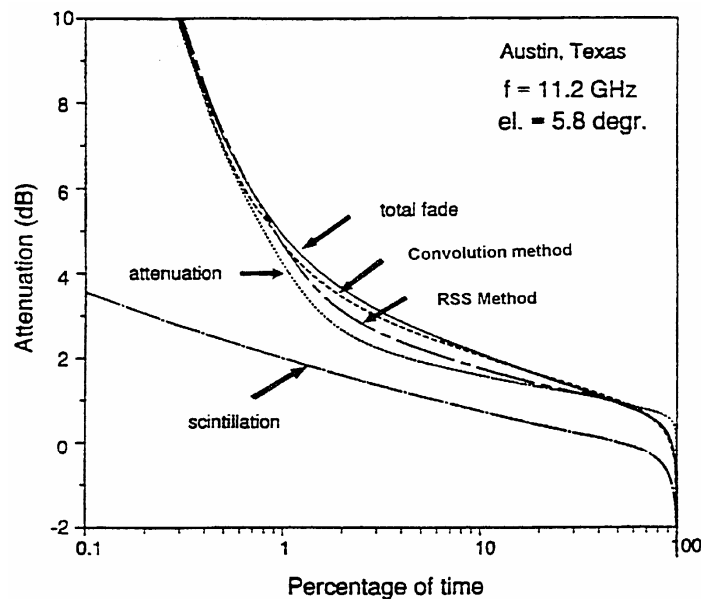


FIGURE 9.1

**Cumulative distributions at 11.2 GHz for an elevation angle of 5.8° in Austin (Texas) from June 1988-May 1992.**

REFERENCES FOR CHAPTER 9

- FELDHAKÉ, G.S., [1996] A sensitivity analysis of combined effects modelling, NAPEX XX, Fairbanks, Alaska.
- KARASAWA, Y. and MATSUDO, T. [1991] Characteristics of fading on low-elevation angle Earth-space paths with concurrent rain attenuation and scintillation, *IEEE Trans. on Antennas and Propagation*, Vol. AP-39, 5, 657-661.
- POIARES BAPTISTA, J.P.V. and DAVIES, P.G. (Editors), [1994] *OPEX, Volume 1: Reference Book on Attenuation Measurement and Prediction*, European Space Agency, WPP-083, Noordwijk, The Netherlands.
- SALONEN, E., KARHU, S., JOKELA, P., ZHANG, W., UPPALA, S., AULAMO, H., SARKKULA, S., POIARES BAPTISTA, J.P.V., [1992] Modelling and calculation of atmospheric attenuation for low-fade-margin satellite communications, *ESA Journal*, Vol. 16, 3, 615-622.
- SALONEN, E., KARHU, S., TERVONEN, J., [1995] Prediction of total atmospheric attenuation for low-fade margin satellite communications, 7th URSI Commission F Open Symposium, Ahmedabad, India.
- SALONEN, E., TERVONEN, J., VOGEL, W., [1996] Scintillation effects on total fade distributions for Earth-satellite links, *IEEE Trans. on Antennas and Propagation*, Vol. AP-44, 1, 23.
- WATSON, P.A. and HU, Y.F., [1994] Prediction of attenuation on satellite-Earth links for systems operating with low fade margins, CLIMPARA '94, URSI Commission F, Moscow, Russia.
-





**\*7320\***

Printed in Switzerland  
Geneva. 1996  
ISBN 92-61-06361-6